Master Thesis

Development of Selection Algorithms for Electron Neutrino Interaction Events with New T2K Near Detectors
(T2K 新型前置検出器を用いた電子ニュートリノ反応事象選別アルゴリズムの開発)

January 20, 2021

Department of Physics, Graduate School of Science
The University of Tokyo
東京大学大学院理学系研究科物理学専攻

Aoi Eguchi
江口碧

Abstract

The T2K (Tokai-to-Kamioka) experiment is a long baseline neutrino oscillation experiment in Japan. We are measuring neutrino oscillations through the detection of electron neutrinos which is originally produced as muon neutrinos at the Japan Proton Accelerator Research Complex (J-PARC) by the Super-Kamiokande detector. We aim to observe the CP violation in lepton sector for the first time in the world. Until now, T2K has rejected the CP conservation in neutrino oscillations with more than 95% confidence level. The uncertainty on the ν_e cross section is one of the largest systematic errors in the current oscillation analysis.

In order to observe the CP violation with higher precision, T2K is proposing to upgrade the near detectors in 2022 and introduce a new tracking detector SuperFGD (Super Fine Grained Detector). In this thesis, we developed selection algorithms with SuperFGD for the interactions of the intrinsic ν_e components in the neutrino beam and evaluated them with the Monte Carlo samples. We achieved the ν_e selection efficiency of 20% with the signal purity over 70% for the ν_e events whose out-coming electron is contained in SuperFGD. The results show the capability of ν_e cross section measurement with SuperFGD, especially in low momentum ($p < 300$ MeV/c) and large scattering angle ($\theta > 45°$) region where no prior direct measurement has been performed so far.

Contents

Chapter 1

Introduction

1.1 Neutrino oscillation

1.1.1 A framework of neutrino physics

The Standard Model (SM) describes the strong, electromagnetic, and weak interactions of elementary particles in the framework of quantum field theory. It requires the presence of three flavors of neutrinos: electron neutrino (ν_e), muon neutrino (ν_μ), and tau neutrino (ν_τ). These three neutrinos and their counterpart charged leptons form the doublets of weak interactions. Neutrinos do not interact electromagnetically since they are electrically neutral. Similarly, they do not interact strongly as they are color-neutral. Thus, neutrinos can only interact via weak interactions: charged current (CC) and neutral current (NC) interaction.

Neutrino has flavor and mass eigenstates. By using lepton mixing matrix U, known as Pontecorvo-Maki-Nakagawa-Sakata (PMNS) matix, one of eigenstates can be transformed into the other as

$$\begin{pmatrix} \nu_e \\ \nu_\mu \\ \nu_\tau \end{pmatrix} = U \begin{pmatrix} \nu_1 \\ \nu_2 \\ \nu_3 \end{pmatrix} = \begin{pmatrix} U_{e1} & U_{e2} & U_{e3} \\ U_{\mu 1} & U_{\mu 2} & U_{\mu 3} \\ U_{\tau 1} & U_{\tau 2} & U_{\tau 3} \end{pmatrix} \begin{pmatrix} \nu_1 \\ \nu_2 \\ \nu_3 \end{pmatrix}. \tag{1.1}$$

This PMNS matrix U is unitary and satisfies

$$\sum_i U_{\alpha i} U^*_{\beta i} = \delta_{\alpha\beta} \ (\alpha, \beta = e, \mu, \tau), \quad \text{and} \quad \sum_\alpha U_{\alpha i} U^*_{\alpha j} = \delta_{ij} \ (i, j = 1, 2, 3). \tag{1.2}$$

The mixing matrix depends on four physical patameters: three mixing angles ($\theta_{12}, \theta_{13}, \theta_{23}$) and one CP-violating phase (δ_{CP}). A convenient parameterization of the Dirac neutrino mixing matrix is

$$U = \begin{pmatrix} 1 & 0 & 0 \\ 0 & c_{23} & s_{23} \\ 0 & -s_{23} & c_{23} \end{pmatrix} \begin{pmatrix} c_{13} & 0 & s_{13}e^{-i\delta_{CP}} \\ 0 & 1 & 0 \\ -s_{13}e^{i\delta_{CP}} & 0 & c_{13} \end{pmatrix} \begin{pmatrix} c_{12} & s_{12} & 0 \\ -s_{12} & c_{12} & 0 \\ 0 & 0 & 1 \end{pmatrix} \tag{1.3}$$

$$= \begin{pmatrix} c_{12}c_{13} & s_{12}c_{13} & s_{13}e^{-i\delta_{CP}} \\ -s_{12}c_{23} - c_{12}s_{13}s_{23}e^{i\delta_{CP}} & c_{12}c_{23} - s_{12}s_{13}s_{23}e^{i\delta_{CP}} & c_{13}s_{23} \\ s_{12}s_{23} - c_{12}s_{13}c_{23}e^{i\delta_{CP}} & -c_{12}s_{23} - s_{12}s_{13}c_{23}e^{i\delta_{CP}} & c_{13}c_{23} \end{pmatrix}, \tag{1.4}$$

where $c_{ab} \equiv \cos\theta_{ab}$ and $s_{ab} \equiv \sin\theta_{ab}$. The three mixing angles take values in the range $0 \leq \theta_{ab} \leq \pi/2$ and the CP-violating phase takes a value in the range $-\pi \leq \delta_{CP} < \pi$.

1.1.2 Neutrino oscillation

Neutrino oscillation is a quantum mechanical phenomenon that converts the flavor of neutrino. It was first discovered by the Super-Kamiokande (SK) collaboration in 1998 [1]. This phenomenon is of fundamental importance in neutrino physics because it is so far the only evidence that neutrinos have a mass different from 0 and that lepton family numbers are not conserved. Neutrino oscillations are described as a consequence of a mixing of neutrino flavor states.

A neutrino with flavor α and momentum $\vec{p}$, created in charged-current weak interaction process, is described by the flavor state

$$|\nu_\alpha\rangle = \sum_k U^*_{\alpha k} |\nu_k\rangle \quad (\alpha = e.\mu, \tau). \tag{1.5}$$

The massive neutrino states $|\nu_k\rangle$ are eigenstates of the Hamiltonian,

$$\mathcal{H} |\nu_k\rangle = E_k |\nu_k\rangle, \tag{1.6}$$

with energy eigenvalues

$$E_k = \sqrt{\vec{p}^2 + m_k^2}. \tag{1.7}$$

The Schrödinger equation

$$i\frac{d}{dt} |\nu_k(t)\rangle = \mathcal{H} |\nu_k(t)\rangle \tag{1.8}$$

implies that the massive neutrino states evolve in time as plane waves:

$$|\nu_k(t)\rangle = e^{-iE_k t} |\nu_k\rangle. \tag{1.9}$$

Now let us consider a flavor state $|\nu_\alpha(t)\rangle$ which decribes a neutrino created with a certain flavor α at time $t = 0$. Substituting Eq. (1.9) into Eq. (1.5), one obtain

$$|\nu_\alpha(t)\rangle = \sum_k U^*_{\alpha k} e^{-iE_k t} |\nu_k\rangle \,. \tag{1.10}$$

The transition probability of $\nu_\alpha \to \nu_\beta$ is, then, given by

$$P_{\nu_\alpha \to \nu_\beta}(t) = |\langle \nu_\beta | \nu_\alpha(t)\rangle|^2 = \sum_{k,j} U^*_{\alpha k} U_{\beta k} U_{\alpha j} U^*_{\beta j} e^{-i(E_k - E_j)t}. \tag{1.11}$$

For ultrarelativistic neutrino, the dispersion relation in Eq. (1.7) can be approximated by $E_k \simeq E + m_k^2/2E$, where $E = |\vec{p}|$ is the neutrino energy. In this case,

$$E_k - E_j \simeq \frac{m_k^2 - m_j^2}{2E} \equiv \frac{\Delta m^2_{kj}}{2E}. \tag{1.12}$$

Also we can approximate $t = L$, because ultrarelativistic neutrinos propagate almost at the speed of light. As a consequence, neutrino oscillation probability in vacuum is calculated as:

$$\begin{aligned} P(\nu_\alpha \to \nu_\beta) = \delta_{\alpha\beta} \; & - 4 \sum_{i<j} \mathrm{Re}[U_{\alpha i} U^*_{\beta i} U^*_{\alpha j} U_{\beta j}] \sin^2\left(\frac{\Delta m^2_{ji} L}{4E}\right) \\ & \pm 2 \sum_{i<j} \mathrm{Im}[U_{\alpha i} U^*_{\beta i} U^*_{\alpha j} U_{\beta j}] \sin\left(\frac{\Delta m^2_{ji} L}{2E}\right), \end{aligned} \tag{1.13}$$

where $\pm$ is for neutrino and antineutrino cases, respectively. When $\alpha = \beta$, it describes the non-oscillation (survival) probability as:

$$P(\nu_\alpha \to \nu_\alpha) = P(\bar{\nu}_\alpha \to \bar{\nu}_\alpha) = 1 - 4 \sum_{i<j} \left| U_{\alpha i} U^*_{\alpha j} \right|^2 \sin^2\left(\frac{\Delta m^2_{ji} L}{4E}\right), \tag{1.14}$$

which is the same for both neutrinos and antineutrinos. This is because $U_{\alpha i} U^*_{\beta i} U^*_{\alpha j} U_{\beta j}$ is real for $\alpha = \beta$.

1.1.3 CP violation in neutrino oscillation

Since the survival probability is the same for neutrinos and antineutrinos, CP violation is not possible for the survival channel. It is only measurable via the comparison of appearance probabilities $P(\nu_\alpha \to \nu_\beta)$ and $P(\bar{\nu}_\alpha \to \bar{\nu}_\beta)$.

As artificial neutrino sources, we currently have two ways of producing neutrinos: reactors and accelerators. Reactors provide us $\bar{\nu}_e$ with an energy of a few MeV. Since this energy range is too smaller than the muon mass of $m_\mu \sim 105.7$ MeV$/c^2$ [2], they cannot be used for measuring the ν_μ appearance probability. All present accelerator-based neutrino beamlines in the world are dedicated to produce a muon neutrino beam. There are some proposals for conducting electron neutrino beamlines like neutrino factories [3] and beta-beams [4]. However, there are many technical problems to realize these electron neutrino beamlines. As a consequence, we search for the CP violation in neutrino oscillations via the appearance channel of $\nu_\mu \to \nu_e(\bar{\nu}_\mu \to \bar{\nu}_e)$ using the accelerator neutrinos.

In order to study the CP violation in neutrino oscillations, it is convenient to introduce the quantity ΔP as

$$\Delta P \equiv P(\nu_\mu \to \nu_e) - P(\bar{\nu}_\mu \to \bar{\nu}_e) \tag{1.15}$$

$$= -16J \sin\left(\frac{\Delta m^2_{32} L}{4E_\nu}\right) \sin\left(\frac{\Delta m^2_{31} L}{4E_\nu}\right) \sin\left(\frac{\Delta m^2_{21} L}{4E_\nu}\right), \tag{1.16}$$

where $J \equiv \text{Im}\left[U_{e1}U^*_{\mu1}U^*_{e1}U_{\mu2}\right]$. The quantity J is known as the Jarlskog invariant and one can write

$$J = \frac{1}{8}\cos\theta_{13}\sin(2\theta_{13})\sin(2\theta_{12})\sin(2\theta_{23})\sin\delta_{CP}. \tag{1.17}$$

According to the current measurements, this is approximately $J = 0.034\sin\delta_{CP}$ [2]. Conditions for CP violation in neutrino oscillations can be summarized as

$$\theta_{ij} \neq 0\ , \quad m_i \neq m_j\ , \quad \delta_{CP} \neq 0, \pi. \tag{1.18}$$

1.1.4 Mass ordering of neutrinos

The ordering of the three neutrino mass eigenstates has not been determined yet. This is one of the important remaining questions in neutrino physics. Since we have experimentally determined that $\Delta m^2_{21} > 0$, there are two possible cases for the mass ordering based on the sign of Δm^2_{31}. The order of $m_1 < m_2 < m_3$ is called as the normal ordering and $m_3 < m_1 < m_2$ is called as the inverted ordering. Figure 1.1 shows the illustration of two possible mass orderings.

The NOvA experiment reported a result to disfavor the inverted mass ordering at the 95% confidence level for all choices of oscillation parameters in 2018 [6].

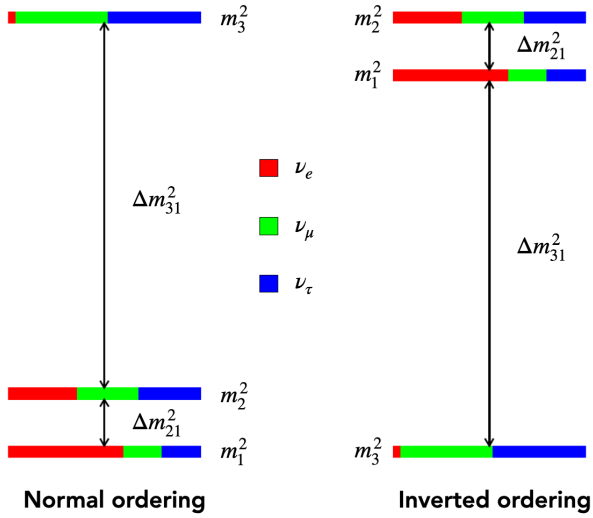

Figure 1.1: Scheme of the two distinct neutrino mass orderings. The color indicates the fraction of each flavor $(\nu_e, \nu_\mu, \nu_\tau)$ present in each of the mass eigenstates (ν_1, ν_2, ν_3) [5].

1.2 Neutrino interaction

1.2.1 Motivation of the cross section measurement

It is important to understand the neutrino interaction with a nucleus in order to measure neutrino oscillations since the oscillation probability is calculated from the number of observed events along with the reconstructed neutrino energy. The number of observed events at the far detector is written as

$$N_{\text{far}}^{\text{obs}} = \Phi_{\text{far}} \times \sigma \times \epsilon_{\text{far}} \times T_{\text{far}} \times P_{\text{osc}}(\theta, \delta_{CP}, \Delta m^2, E_\nu), \tag{1.19}$$

where Φ_{far} is the neutrino flux at the far detector assuming no oscillation, σ is the neutrino-nucleus interaction cross section, ϵ_{far} is the detection efficiency, and T_{far} is the number of the target nuclei at the far detector. $P_{\text{osc}}(\theta, \delta_{CP}, \Delta m^2, E_\nu)$ is the oscillation probability as a function of the oscillation parameters and the neutrino energy. We can calculate the oscillation probability via the measurement of $N_{\text{far}}^{\text{obs}}$ and the neutrino energy. It is fundamental to understand the neutrino interaction with nucleus and measure the cross section precisely.

Neutrinos interact with a nucleus only via a weak interaction. The interaction that exchanges W boson is called charged-current interaction (CC), and one that exchanges Z boson is called neutral-current interaction (NC). Charged lepton is produced in CC interaction but not in NC interaction.

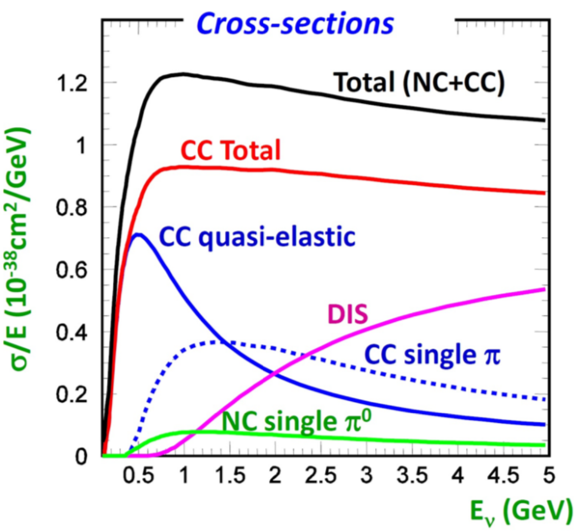

Figure 1.2: Cross sections of neutrino-nucleus interactions calculated with MC simulation.

As shown in Figure 1.2, there are contributions of several interaction processes depending on the neutrino energy. In the T2K experiment, the neutrino energy spectrum has a peak around 0.6 GeV and is distributed up to a few GeV. At this energy region, the most dominant interaction process is charged current quasi-elastic scattering (CCQE), while resonance scattering (RES) and deep inelastic scattering (DIS) processes get more dominant at higher energy region. The more detailed explanations on these interaction models are given in Appendix A.

1.2.2 Electron neutrino interaction

Since the CP violation is only observable via $\nu_e(\bar{\nu}_e)$ appearance channel, we are measuring $\nu_e(\bar{\nu}_e)$ at the far detector. On the other hand, the main component of the neutrino beam is $\nu_\mu(\bar{\nu}_\mu)$ at the near detector which is measuring neutrino cross sections and constraining the systematic uncertainties. In order to measure the CP violation, it is also important to measure the $\nu_e(\bar{\nu}_e)$ cross sections at the near detector.

There is a difference between ν_e and ν_μ quasi-elastic cross sections especially at low neutrino energies [7]. This is because of the different kinematic limits due to the final-state lepton mass and the presence of the pseudoscaler form factor F_P, which are generally accounted for in modern neutrino generators. There are also differences coming from radiative corrections and the

Table 1.1: Status of ν_e and $\bar{\nu}_e$ cross section measurements in the world.

Year	Experimet	Average neutrino energy (range)	Target	Reference
1978	Gargamelle	0.6-10 GeV	CF_3Br	[8]
2014	T2K	1.28 GeV	CH	[9]
2016	MINERvA	3.6 GeV	CH	[10]
2020	T2K	1.28 GeV (ν_e)/1.98 GeV ($\bar{\nu}_e$)	CH	[11]

effect of the form factors F_V^3 and F_A^3 corresponding to second class currents, which are not included in neutrino interaction generators. These differences introduce a systematic uncertainty on the neutrino oscillation analysis.

Measurements of ν_e interaction cross section at a few GeV region have been performed by several experiments as listed in Table 1.1. The first CC-ν_e and CC-$\bar{\nu}_e$ inclusive cross section measurement was made by the Gargamelle experiment using a heavy liquid bubble chamber in 1978 [8]. Thirty-six years later, T2K measured the CC-ν_e inclusive cross section at an average ν_e energy of 1.3 GeV in 2014 [9]. The MINERvA collaboration also measured the ν_e CCQE-like scattering cross section on hydrocarbon target at an average ν_e energy of 3.6 GeV in 2016 [10]. In 2020, T2K updated the result of CC-ν_e cross section measurement and newly measured CC-$\bar{\nu}_e$ cross section at an average $\bar{\nu}_e$ energy of 2.0 GeV [11], whose results will be reviewed in Chapter 2.

However, in this energy range (0.3 to a few GeV), the relatively small components of ν_e and $\bar{\nu}_e$ flux in neutrino beams limit the statistics of data. In addition, the contamination of the background such as photons from π^0 decays give a large systematic uncertainties on the cross section measurements. These limitations prevent us from using these results for tuning simulations directly. Therefore, most simulations used in current neutrino oscillation experiments tune the $\nu_e(\bar{\nu}_e)$ cross section with high-precision $\nu_\mu(\bar{\nu}_\mu)$ cross section data and apply corrections such as those discussed above. The measurements of the $\nu_e(\bar{\nu}_e)$ cross sections will be crucial for the precision measurements of neutrino oscillations.

Chapter 2

T2K experiment

2.1 Overview

The T2K (Tokai to Kamioka) experiment is a long baseline neutrino oscillation experiment which has been conducted in Japan [12]. It started its first physics run in January 2010. It uses a ν_μ and $\bar{\nu_\mu}$ beam produced in the Japan Proton Accelerator Research Complex (J-PARC) in Ibaraki prefecture. Neutrinos are detected at the near detector at 280 m from the beam production point and at the far detector, Super-Kamiokande in Gifu prefecture as shown in Figure 2.1.

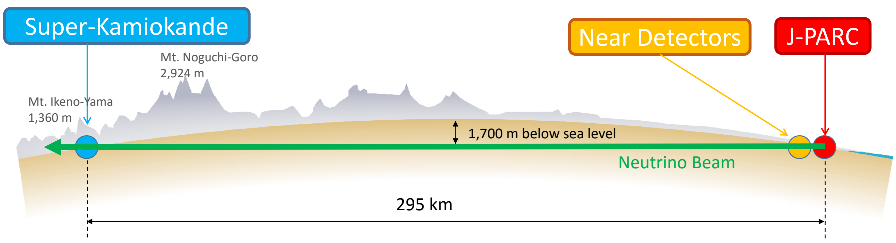

Figure 2.1: Overview of the T2K experiment.

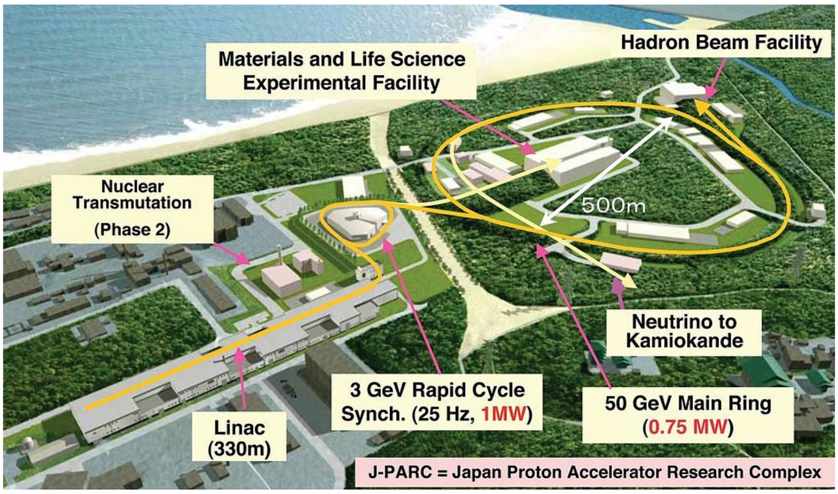

Figure 2.2: Overview of the J-PARC.

2.2 J-PARC accelerators and neutrino beamline

2.2.1 Overview of the beamline

The J-PARC proton accelerator consists of three accelerators: a 400 MeV linear accelerator (LINAC), 3 GeV rapid cycling synchrotron (RCS), and a 30 GeV main ring synchrotron (MR) as shown in Figure 2.2. Protons are accelerated to 30 GeV and directed to the neutrino beamline.

A proton spill consists of 8 bunches with 580 ns spacing. It is produced every 2.48 s as shown in Figure 2.3. Each bunch typically has a timing spread of $\simeq$ 15 ns. At a beam power of 430 kW, this corresponds to 2.25×10^{14} protons on target (POT) per spill [13].

Figure 2.4 shows the schematic view of the neutrino beamline at J-PARC. Protons strike a graphite target and create secondary pions and other hadrons. Created pions are focused by three magnetic horns and decay into muons and muon neutrinos. The polarity of the magnetic field made by the horns for the neutrino beam mode is defined as a forward horn current (FHC), while that for the antineutrino beam mode is defined as a reversed horn current (RHC). The dominant decay channels for FHC and RHC mode are

$$\begin{aligned} \pi^+ &\to \mu^+ + \nu_\mu, \\ \pi^- &\to \mu^- + \bar{\nu}_\mu, \end{aligned} \tag{2.1}$$

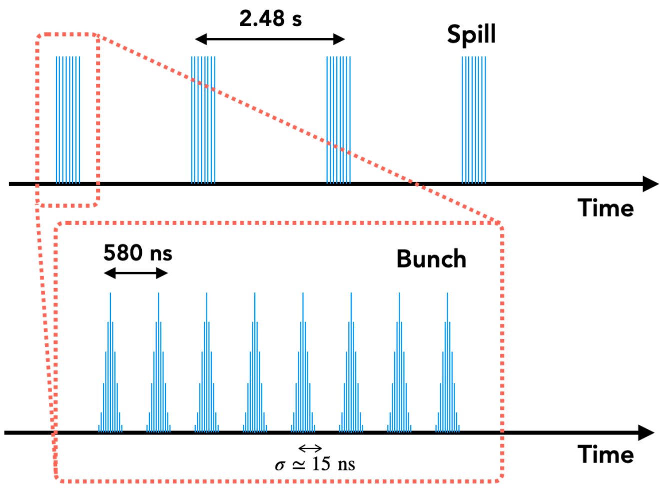

Figure 2.3: Time structure of the proton beam spill.

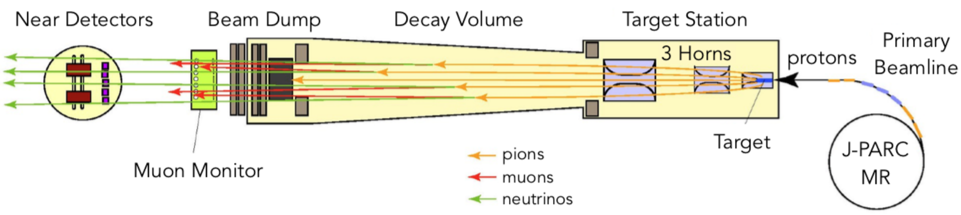

Figure 2.4: Schematic view of the neutrino beamline.

respectively. For 3 GeV or higher energy neutrinos, dominant contributions are from kaon decays such as:

$$
\begin{aligned}
K^{+} &\rightarrow \mu^{+} + \nu_{\mu}, \\
K^{+} &\rightarrow \pi^{0} + \mu^{+} + \nu_{\mu}, \\
K^{-} &\rightarrow \mu^{-} + \bar{\nu}_{\mu}, \\
K^{-} &\rightarrow \pi^{0} + \mu^{-} + \bar{\nu}_{\mu}.
\end{aligned}
\tag{2.2}
$$

Hadrons are stopped by the beam dump located 109 m downstream from the target. High energy muons can penetrate the beam dump and they are detected with the muon monitor (MUMON [14]) which is composed of two detectors: ionization chambers and silicon PIN photodiodes. MUMON can monitor the two dimentional profile of the beam direction and the beam intensity as well.

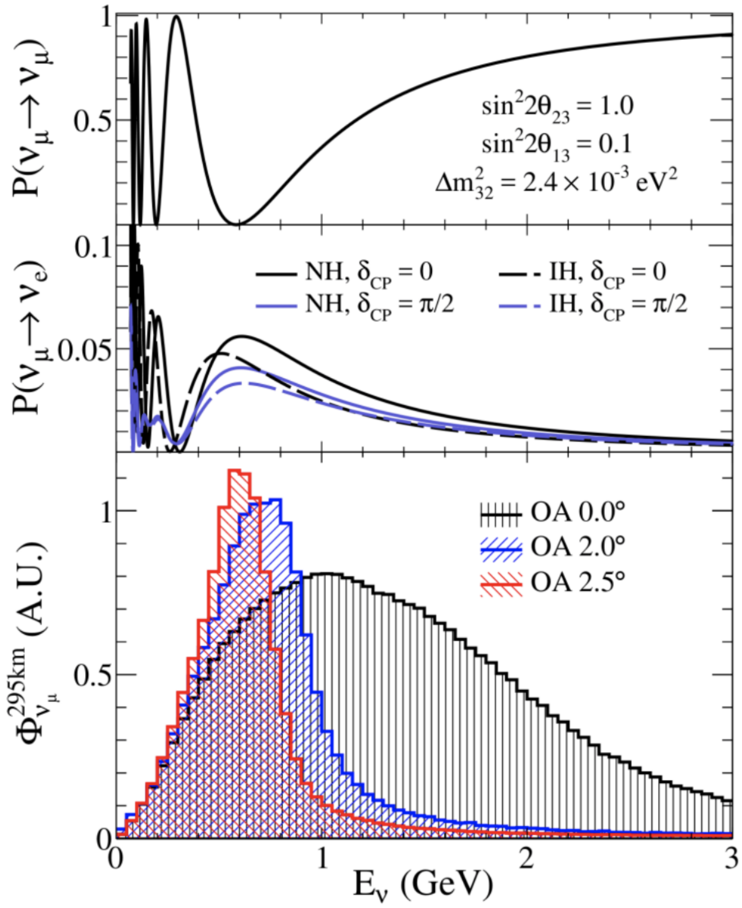

Figure 2.5: The probability of the neutrino oscillation and muon neutrino flux at different off-axis.

2.2.2 Off-axis method

One of the most important features of the T2K experiment is the off-axis method. The direction of Super-Kamiokande and ND280 is shifted by 2.5° from the proton beam direction. This finite off-axis angle provides us a narrower neutrino energy spectrum than that at on-axis. It has a peak at around 600 MeV. Figure 2.5 shows the probability of the neutrino oscillation and the simulated neutrino flux at different off-axis angles. The off-axis angle of 2.5° is chosen to maximize the neutrino oscillation probability at the location of Super-Kamiokande.

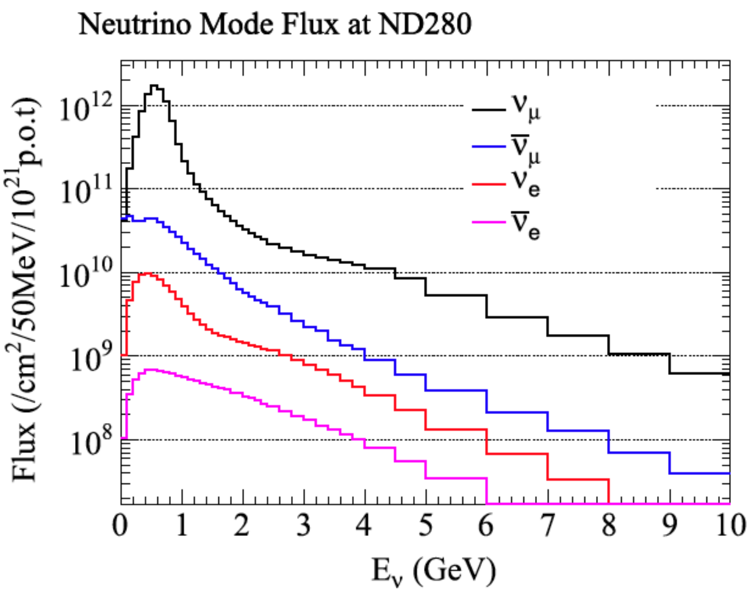

Figure 2.6: The predicted flux as a function of neutrino energy at ND280 in FHC [15].

2.2.3 Beam property

The compositions of the predicted neutrino flux at ND280 are shown in Figure 2.6. While the dominant sources of muon neutrinos are described with Eq. (2.1) and (2.3), there are wrong-sign neutrino contamination for each mode. This is caused by the incompleteness of the magnet horn focusing.

In addition to that, there are $\nu_e(\bar{\nu}_e)$ components which are mainly generated from kaon and muon decays:

$$\begin{aligned} K^+ &\to \pi^0 + e^+ + \nu_e, \\ \mu^+ &\to e^+ + \nu_e + \bar{\nu}_\mu, \\ K^- &\to \pi^0 + e^- + \bar{\nu}_e, \\ \mu^- &\to e^- + \bar{\nu}_e + \nu_\mu. \end{aligned} \tag{2.3}$$

The mean of the ν_e energy spectrum at ND280 is 1.28 GeV in FHC and 1.98 GeV in RHC mode. The total integrated ν_e flux at ND280 in FHC is

$$\Phi_{\nu_e}^{\mathrm{FHC}} = (2.67 \pm 0.24) \times 10^{11} \text{ neutrinos/cm}^2, \tag{2.4}$$

which is estimated to be approximately $\sim 1\%$ of the total ν_μ flux.

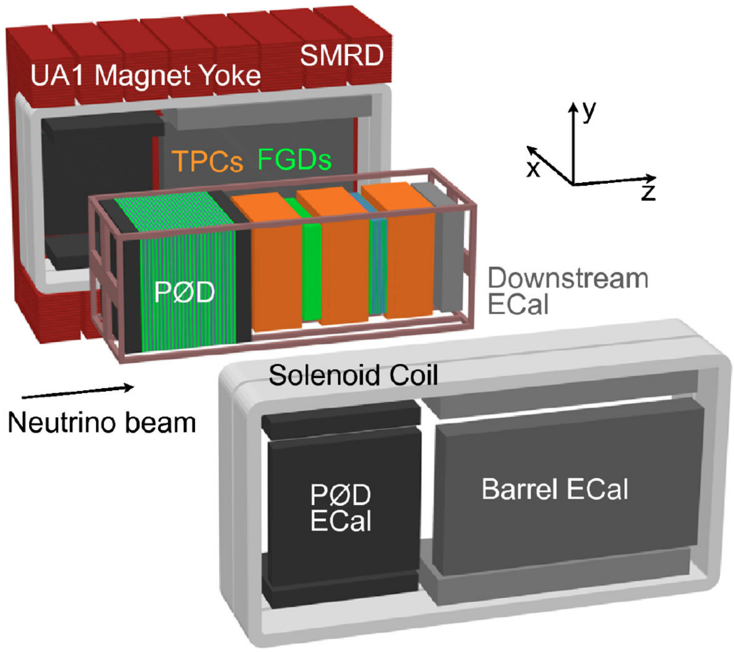

Figure 2.7: Overview of the ND280 detector complex.

2.3 Near detectors

The T2K experiment has a magnetized detector complex so-called ND280 that is located at the same off-axis angle as Super-Kamiokande at a distance of 280 m from the target. The schematic view of the ND280 is shown in Figure 2.7.

ND280 consists of several sub-detectors. Two Fine Grained Detectors (FGD) and three Time Projection Chambers (TPC) are the main tracking detectors in ND280. In analysis, we mainly use neutrino interactions which take place in one of the FGDs and whose out-going lepton tracks are entering one of the TPCs. There are several electromagnetic calolimeters (ECal) surrounding these tracking detectors to support the particle identification and energy reconstruction of charged particle tracks which are penetrating the TPCs. The π^0 detector (P0D) is placed at the upstream of the tracking detectors aiming at measuring the neutral current interactions. As drawn in Figure 2.7, FGDs, TPCs, downstream ECal, and P0D are contained in a supporting structure, which is called a basket. All these sub-detectors are placed in the UA1 magnet that provides a 0.2 T magnetic field.

We will give a brief introduction to each sub-detector.

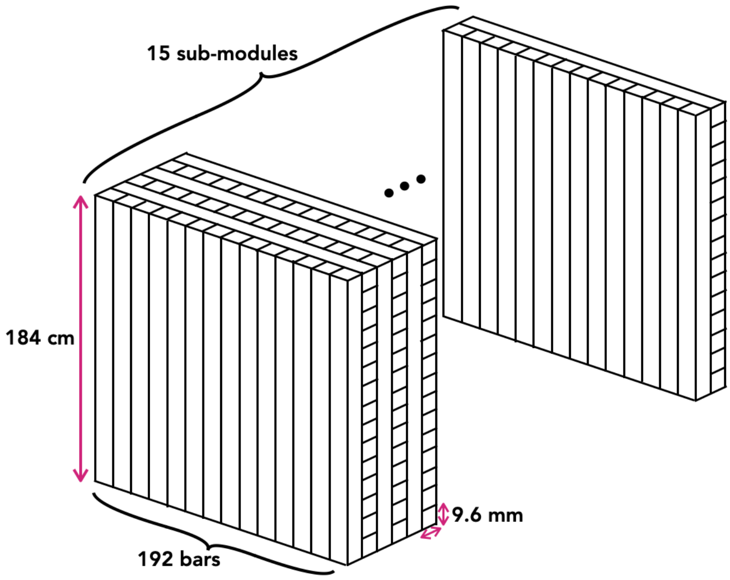

Figure 2.8: The schematic view of the FGD1.

FGD (Fine-Grained Detector)

Fine-Grained detector (FGD) is a plastic scintillator (and water) target detector [16]. There are two FGDs sandwiched by three TPCs inside the magnet. The upstream and the downstream FGDs are called FGD1 and FGD2, respectively. FGDs consist of several sub-modules which are made with fine-grained scintillator bars with the size of 184 cm $\times$ 0.96 cm $\times$ 0.96 cm that are oriented perpendicular to the beam direction as shown in Figure 2.8. One sub-module is composed of two orthogonal layers that consist of 192 scintillator bars in the horizontal and vertical direction. While FGD1 has fifteen sub-modules, FGD2 has seven modules along with six water sub-modules that have thin-walled hollow polycarbonate sheets filled with water.

TPC (Time Projection Chamber)

Three time projection chambers (TPC) are also used for tracking charged particles generated from the neutrino interactions in FGDs. It is filled with the gas that is a mixture of $\mathrm{Ar} : \mathrm{CF}_4 : i\mathrm{C}_4\mathrm{H}_{10}$ (95%:3%:2%) [17]. Uniform electric field is applied in a horizontal direction aligned with the magnetic field direction. When charged particles pass through the TPC, they ionize the gas molecules and generate electron-ion pairs along its trajectory. Ionized electrons drift toward the anode and they are detected by Micromegas modules [18].

By using TPCs, we can reconstruct tracks in 3D and perform the charge and momentum measurement for charged particles. It also allows us to conduct a particle identification by combining the energy loss with momentum measurement.

P0D (Pi-0 Detector)

The π^0 detector (P0D) is located at the upstream of the tracker detectors. It is aiming at observing neutral current interactions that contain π^0 in the final state:

$$\nu_\mu + N \to \mu + N + \pi^0 + X. \tag{2.5}$$

The central region, which is referred to as the water target region, is made from alternating scintillator planes, water bags, and brass sheets [19].

ECal (Electromagnetic CALolimeter)

The electromagnetic calolimeter (ECal) is a lead-scintillator sampling calorimeter which surrounding the tracking detectors and P0D [20]. As shown in Figure 2.7, it consists of three main parts: the P0D-Ecal which surrounds P0D, the barrel-Ecal (Brl-ECal) which surrounds the FGDs and TPCs, and the downstream-ECal (Ds-ECal) which is located downstream of the tracking detectors. Also, the Brl-ECal and Ds-ECal together are referred to as the tracker-ECal. ECal consists of 13 modules: 6 P0D-ECal (2 top, 2bottom, 2 side), 6 Brl-ECal (2 top, 2 bottom, 2 side) and 1 Ds-ECal. Each module consists of layers of scintillating polystyrene bars with the size of 40 mm$\times$10 mm bonded to lead sheets. The thickness of the lead sheets is 1.75 mm in the tracker-ECal and 4.00 mm in the P0D-ECal.

2.4 Far detector

The Super-Kamiokande (SK) is the far detector of the T2K experiment and it detects neutrinos after traveling 295 km. It is a cylindrical water Chrenkov detector fullfilled with 50 kton of water. The diameter of the tank is 39.3 m and the height is 41.4 m. Inner wall of the water tank is covered by 11,200 20-inch photomultiplier tubes (PMT) and outer wall is covered by 1,185 8-inch PMTs for the purpose of VETO.

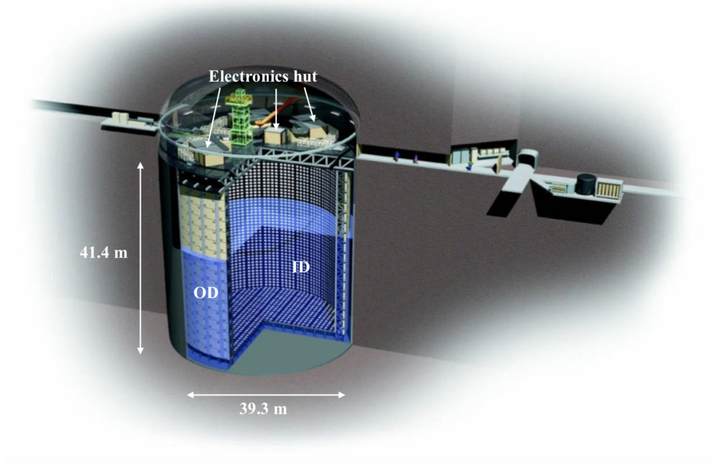

Figure 2.9: Schematic view of the Super-Kamiokande.

2.5 T2K recent results

2.5.1 Oscillation analysis results and systematic errors

The main goal of the T2K experiment is to search for the CP violation in lepton sector by measuring the $\nu_\mu \to \nu_e$ (and $\bar{\nu}_\mu \to \bar{\nu}_e$) oscillation signal. Until now, T2K has concluded that the 3σ confidence interval for δ_{CP} is $[-3.41, -0.03]$ for the normal mass ordering and $[-2.54, -0.32]$ for the inverted mass ordering based on neutrino (antineutrino) mode data corresponding with $1.49 \times 10^{21}(1.64 \times 10^{21})$ protons on target (POT) [21]. The sources of systematic uncertainties on the predicted relative number of ν_e and $\bar{\nu}_e$ candidates are summarized in Table 2.1.

The T2K collaboration is proposing the second stage of the experiment named as T2K-II phase to search for the CP violation with more than 3σ significance level [22]. In T2K-II phase, we are planning to collect data of 10×10^{21} POT by 2027 when Hyper-Kamiokande is going to start operation [23]. Toward this new phase, the J-PARC MR and the neutrino beamline will be upgraded in 2021-2022 to achieve the beam power of 1.3 MW with the repetition cycle of 1.16 s. This beamline upgrade will provide us 3.2×10^{14} POT per spill, which is increased by $\sim 30\%$ from the current one.

As the data statistics will increase, the effect of the systematic errors will be more crucial to the precision CP violation measurement. Therefore, it is required to reduce the systematic uncertainty from $\sim 6\%$ to $\sim 4\%$ level to match the needs of T2K-II phase [24]. The uncertainties on ν_e and $\bar{\nu}_e$ cross

Table 2.1: The systematic uncertainties on the predicted relative number of ν_e and $\bar{\nu}_e$ candidates in the SK samples with no decay electrons [21].

Type of uncertainty	$\nu_e/\bar{\nu}_e$ candidate relative uncertainty (%)
SK detector model	1.5
Pion FSI and rescattering model	1.6
Neutrino production and interaction model constrained by ND280 data	2.7
ν_e and $\bar{\nu}_e$ interaction model	3.0
Nucleon removal energy in interaction model	3.7
Modeling of NC interactions with single γ	1.5
Modeling of other NC interactions	0.2
Total systematic uncertainty	6.0

sections are one of the largest systematic error sources as listed in Table 2.1. In the current analysis, ν_e and $\bar{\nu}_e$ cross sections are decided from the well-known ν_μ and $\bar{\nu}_\mu$ cross sections with applying several corrections since they have not been measured with high enough precision. It is a high priority to reduce this systematic error toward the T2K-II phase.

2.5.2 Electron neutrino cross section measurements

In order to understand the ν_e and $\bar{\nu}_e$ interaction model and reduce the systematic uncertainty on oscillation analysis, T2K has tried to measure the ν_e and $\bar{\nu}_e$ cross sections with ND280 using the intrinsic $\nu_e(\bar{\nu}_e)$ component of the neutrino beam [9, 11]. In this analysis, 11.92×10^{20} POT are analyzed for FHC mode and 697 events are selected in total. The momentum and angular distribution of selected electron candidates that are used in this ν_e cross section measurement are shown in Figures 2.10. A significant amount of photon background populates the low momentum and high angle regions which gives a large systematic uncertainties. Using the NEUT (5.3.2) [25], the total ν_e selection efficiency and purity in FHC mode were calculated as 26% and 54%, respectively. The measured ν_e cross section in FHC mode is

$$\sigma_{\nu_e} = (6.62 \pm 1.32(\text{stat}) \pm 1.30(\text{syst})) \times 10^{-39}\ \text{cm}^2/\text{nucleon}, \qquad (2.6)$$

where both statistic and systematic errors have almost the same level of limitation. In order to reduce both of the errors, we need to achieve the high selection efficiency and high purity of the sample.

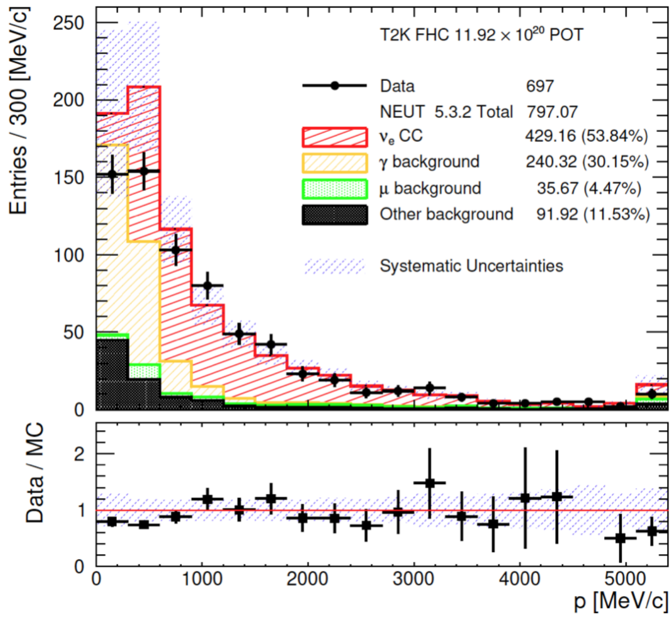

(a) Momentum distribution

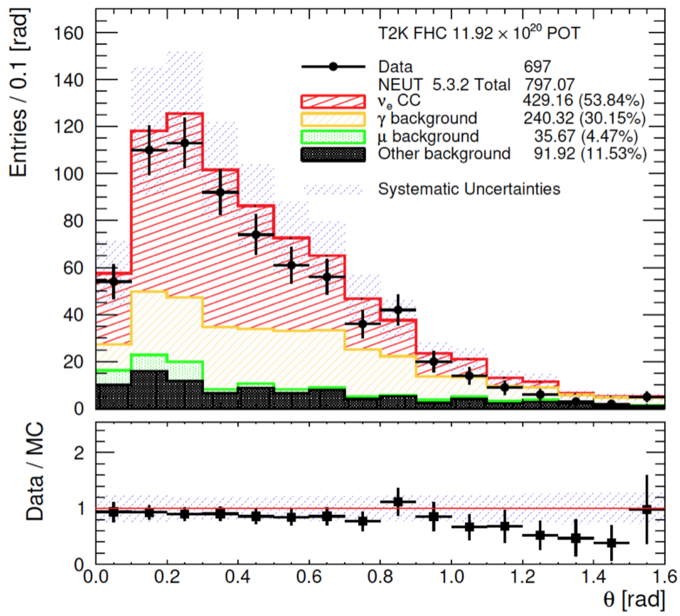

(b) Angular distribution

Figure 2.10: Reconstructed (a) momentum and (b) angular distributions of the selected electron candidates in FHC mode. The number of MC events is normalized to the data POT. The effect of the total systematic uncertainty on the MC events yields is also shown as a shaded region. [11]

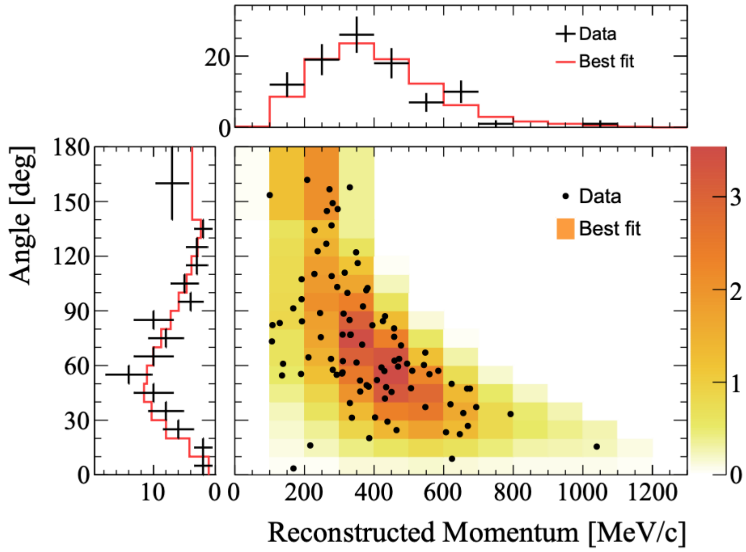

Figure 2.11: Reconstructed momentum and angular phase space distributions of the observed single e-like ring events at SK for FHC mode. The colored background shows the expected number of events with simulation.

Furthermore, this measurement was performed in a limited phase space ($p > 300$ MeV/c and $\theta < 45°$). This limit gives a discrepancy from the measurement of ν_e signals at SK. Figure 2.11 shows the reconstructed momentum-angular phase space distributions of the ν_e candidate events at SK. We have many events in $p < 300$ MeV/c and $\theta > 45°$ region, where no direct measurement of the ν_e cross section has been performed yet. Since SK has full polar angle acceptance and electron selection threshold of $p > 100$ MeV/c, it is important to measure the ν_e cross section in the same phase space with near detectors.

Chapter 3

ND280 upgrade

3.1 Strength and weakness of the current near detectors

In order to constrain the uncertainties on neutrino interaction models and cross sections, T2K is measuring neutrino-nucleus cross sections by using near detectors.

Thanks to the three TPCs surrounding two FGDs, ND280 has an excellent capability of the particle identification and the kinematics measurement of charged particles. This allows us to study neutrino interactions in detail with different final state topologies based on the number of pions in the final state [13, 26]. With the combinations of several sub-detectors including FGDs, TPCs, and ECals, we can measure various types of neutrino interaction cross sections.

Since ND280 is in a magnetic field, it can also distinguish the positively charged leptons from negatively charged leptons, which makes it possible to distinguish neutrino interactions and antineutrino interactions. This feature is important to correctly measure the cross section particularly in antineutrino mode, since about 30% of the interactions in ND280 are induced from neutrinos.

However, current detector configurations have a limited acceptance for particles with a large scattering angle. Since the TPCs are located only at the forward and backward regions of the FGDs, the ND280 has a lower efficiency for scattering angles larger than $\sim 40^\circ$ to the beam direction while SK has a full-angle acceptance. This difference of measurable phase spaces gives an uncertainty when the cross sections measured by ND280 are extrapolated to the full-angle region.

The second weakness of the ND280 is the low efficiencies for low momentum particles. In FGDs, each sub-module is composed of two orthogonal layers in which plastic scintillator bars are aligned in the vertical and horizontal directions as shown in Figure 2.8. Thus, when we require three hits in each direction to reconstruct a track, the shortest track length is about 6 cm. In case of protons, this length corresponds to about ~ 600 MeV/c and most of the lower momentum protons stop before traveling this distance. It is essential to detect protons with momentum below 600 MeV/c in order to precisely understand the detail of neutrino-nucleon interactions.

The third weakness of the ND280 is the low selection capability for low momentum electrons. The conversion of γ which is coming from π^0 decay is the largest contamination when selecting electrons generated from ν_e interactions in the current ND280. It limits the capability of the ν_e cross section measurement at ND280.

3.2 Physics motivation of the detector upgrade

The T2K experiment is planning to measure the CP violation with 3σ or higher significance level with the data of 10×10^{21} POT in upcoming T2K-II phase [22]. It is required to reduce the systematic uncertainty from $\sim 6\%$ to $\sim 4\%$ level to match the needs of T2K-II phase [24]. In order to achieve this, we are planning to upgrade the ND280 and improve the performance. The requirements for the ND280 upgrade can be listed as below:

1. Full polar angle acceptance with similar performance in terms of momentum resolution, energy loss, and charge measurement.

2. Fiducial mass of a few tons (each FGD has a fiducial mass of approximately one ton).

3. High tracking efficiency for low energy pions and protons contained inside the scintillator detector.

4. High separation capability of low momentum electrons from converted gammas.

In order to satisfy these requirements, we decided to replace P0D detector with new tracking detectors. The main target detector is Super Fine Grained Detector (SuperFGD) which are vertically sandwiched by two High Angle Time Projection Chambers (HA-TPC) as shown in Figure 3.1. These tracking detectors are surrounded by six Time of Flight (TOF) layers.

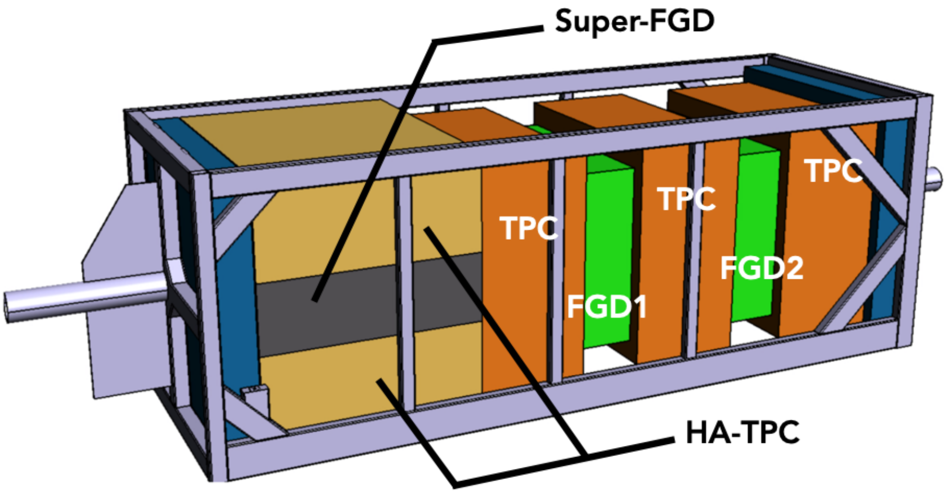

Figure 3.1: Schematic view of the upgraded ND280 [24].

SuperFGD is a highly granular detector consisting of 1 cm side plastic scintillator cubes. This detector allows us to track particles scattered in 4π solid angle. Also, the high granularity of the SuperFGD is expected to provide a high tracking efficiency for protons and pions stopping in this detector. Moreover, the separation capability of electrons from gammas is also expected to be improved.

3.3 New detectors

3.3.1 SuperFGD

SuperFGD is a highly granulated plastic-scintillator detector. It consists of $192 \times 56 \times 184$ scintillator cubes that have a size of $1 \times 1 \times 1$ cm^3. Each cube has three through holes in three directions to put WLS fibers through them. The scintillation light is collected and transported via WLS fibers and detected by MPPCs at one side of the WLS fibers. The schematic view of the SuperFGD is shown in Figure 3.2.

Scintillator cube

The scintillator cubes are produced by UNIPLAST Co. (Vladimir, Russia). They are mainly made of polystyrene doped with 1.5% of paraterphenyl (PTP) and 0.01% of POPOP. Cubes are covered by a reflecting layer which

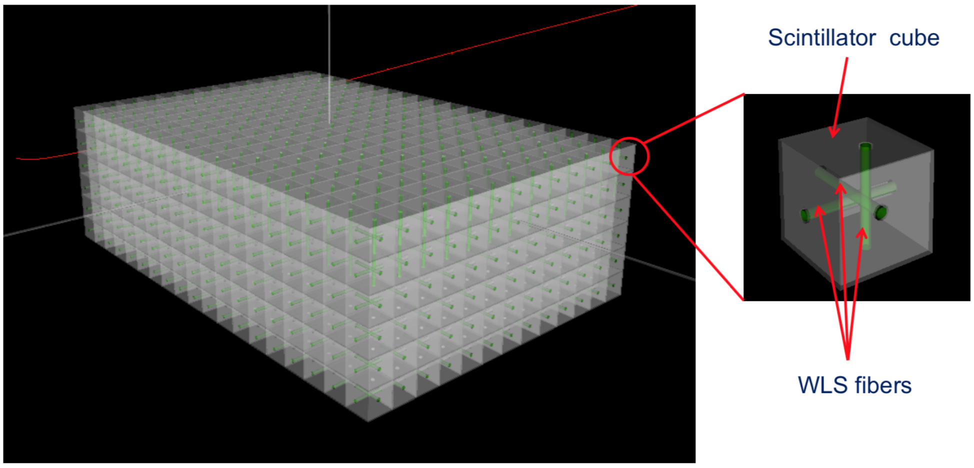

Figure 3.2: Schematic view of the SuperFGD.

is produced with a chemical etching of the scintillator surface. The thickness of the reflecting layer is within 50-80 μm. Each cube has three orthogonal through holes with a diameter of 1.5 mm.

WLS fiber

Wavelength shifting (WLS) fibers are used in order to efficiently collect scintillation light from the scintillator cubes. The WLS fibers Y-11 (200), which are also used in the current ND280, are produced by KURARAY Co., LTD [27]. They have multi-cladding structure with a 1.0 mm diameter. The peak absorption wavelength of the WLS fibers is 430 nm, which is matched with the wavelength of scintillation light from plastic scintillators.

MPPC

We adopted the Multi-Pixel Photon Counter (MPPC) S13360-1325PE produced by Hamamatsu Photonics K.K. as the photosensor [28]. It is a solid state photodetector that uses multiple avalanche photodiode (APD) pixels operated in Guiger mode. MPPC has several advantages over traditional photomultiplier tubes (PMT) such as the magnetic field resistance, smaller volume and lower operation voltage.

Readout electronics

We use Cherenkov Imaging Telescope Integrated Read Out Chip (CITIROC) as a readout electronics. CITIROC is a front-end ASIC developed by Omega laboraroty at Ecole Polytechnique [29]. It can readout 32 channel of SiPM outputs at the same time [30].

Beam test

In order to test the detector and electronics response, we conducted a beam test at CERN-PS T9 beamline in 2018 with a SuperFGD prototype detector [31]. The prototype is made of $24 \times 8 \times 48$ cubes and is instrumented with readout electronics similar to the future implementation for SuperFGD. We recorded detector responses to different particle types so that they can be reflected in the detector response simulation.

3.3.2 HA-TPC (High-Angle TPC)

Two High-Agnle TPCs vertically sandwich the SuperFGD. The schemtic view of the HA-TPC is shown in Figure 3.3. The basic structure of the HA-TPC is the similar to the TPCs which are described in Section 2.3. It consists of a gas tight rectangular box sub-divided by a common high-voltage electrode cathode located in its midpoint. Eight Micromegas readout modules held by model frames are located at each end of the box in parallel to the cathode.

3.3.3 TOF (Time of Flight detector)

Six Time of Flight (TOF) detectors surround SuperFGD and HA-TPCs. The main aim of this detector is to precisely measure the crossing time of charged particles in ND280. This allows us to determine their direction to separate neutrino interactions in the target from backgrounds originated outside of the detector. Six TOF planes consist of several plastic scintillator bars. The bars running along the beam direction have a size of $200 \times 1 \times 12$ cm^3, while the bars perpendicular to the beam have a size of $230 \times 1 \times 12$ cm^3. These sizes are decided to fully enclose the SuperFGD and HA-TPCs. Large-area MPPCs are applied directly to the plastic scintillator bars on both ends.

3.4 Subject of this thesis

As discussed earlier, one of the largest systematic uncertainty sources in the T2K oscillation analysis is the cross section of electron neutrinos. So far,

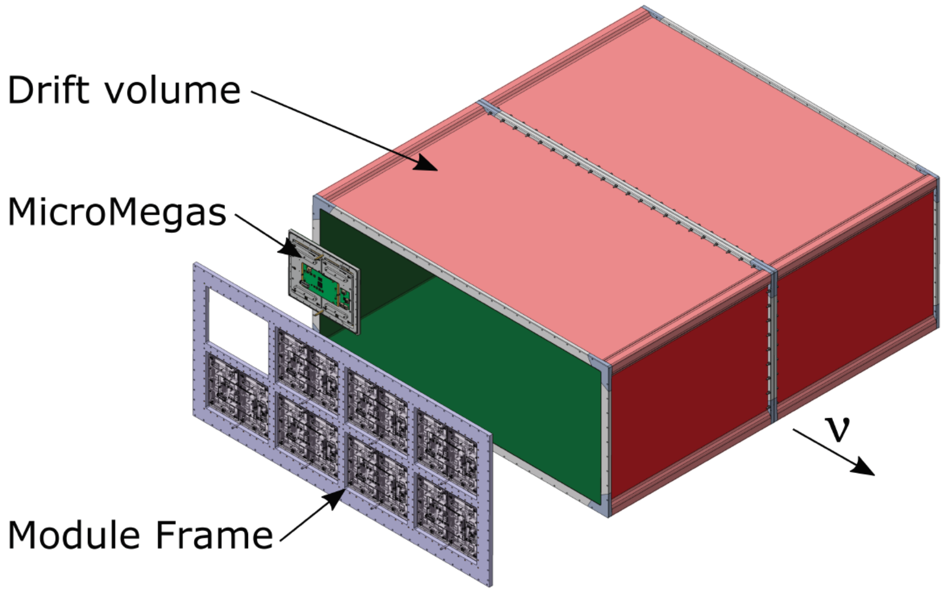

Figure 3.3: The schematic view of the HA-TPC [24].

measurements of ν_e cross section are mainly limited by the small statistics of the data and the large contamination of gamma backgrounds. However, thanks to its high granularity, SuperFGD is expected to improve the selection capability of ν_e interaction events.

Upgrade detectors are currently under construction and will be installed in 2022. In parallel, we are preparing the simulation, reconstruction, and analysis infrastructures. In this thesis, we will introduce new algorithms for selecting ν_e interaction events and evaluate them with Monte Carlo data.

Chapter 4

Monte Carlo data production and reconstruction

4.1 Monte Carlo samples

In this section, we describe the two types of Monte Carlo (MC) samples used in this thesis: neutrino interaction samples and particle gun samples. These MC samples are generated through a series of simulation processes such as neutrino interaction generation with NEUT, Geant4 simulation, and detector response simulation. The detail explanations of these simulation processes are given in Appendix B.

4.1.1 Neutrino interaction sample

Using NEUT 5.4.0, we generated two neutrino interaction MC samples with different flux inputs: a basket flux and a magnet flux that correspond to 1×10^{21} POT and 1×10^{20} POT, respectively. Both samples are generated in FHC mode. The magnet flux sample is simulated with all materials inside the magnet while the basket flux sample does not contain the P0D ECals, the Barrel ECals, and the magnet.

Events are first divided into 3 categories: CC-$\nu_\mu(\bar{\nu}_\mu)$, CC-$\nu_e(\bar{\nu}_e)$, and NC samples. First two samples correspond to the CC interactions which have a corresponding lepton in the final state. Events are classified as NC samples if they do not have any charged lepton in the final state. The momentum and angular distributions of the out-coming lepton for $\nu_\mu(\bar{\nu}_\mu)$ and $\nu_e(\bar{\nu}_e)$ samples are shown in Figure 4.1. The backward scattering is suppressed for antineutrino interactions because of the spin orientation [32]. Also, since the ν_e flux has a higher mean energy compared to that of the ν_μ flux, ν_e samples have relatively high momentum lepton.

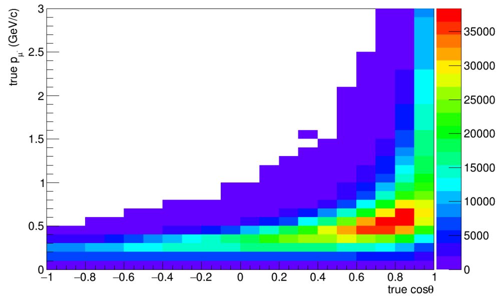

(a) ν_μ samples.

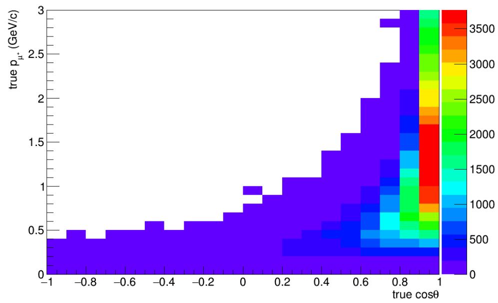

(b) $\bar{\nu}_\mu$ samples.

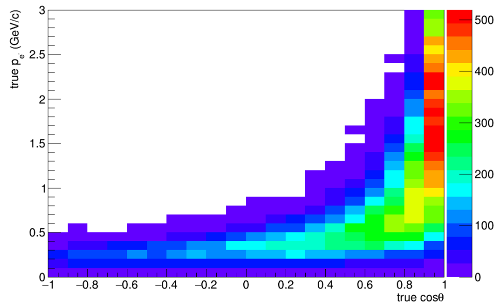

(c) ν_e samples.

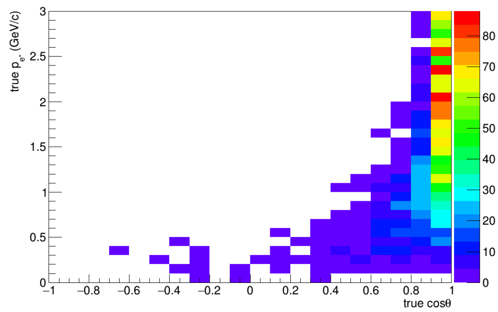

(d) $\bar{\nu}_e$ samples.

Figure 4.1: True momentum and angular distribution of the (a) ν_μ, (b) $\bar{\nu}_\mu$, (c) ν_e, and (d) $\bar{\nu}_e$ samples using the magnet flux sample (1×10^{20} POT). Angle is plotted as the cosine of the angle between the true lepton direction and the beam direction (z-axis), which means that 1 corresponds to the forward scattering and -1 corresponds to the backward scattering.

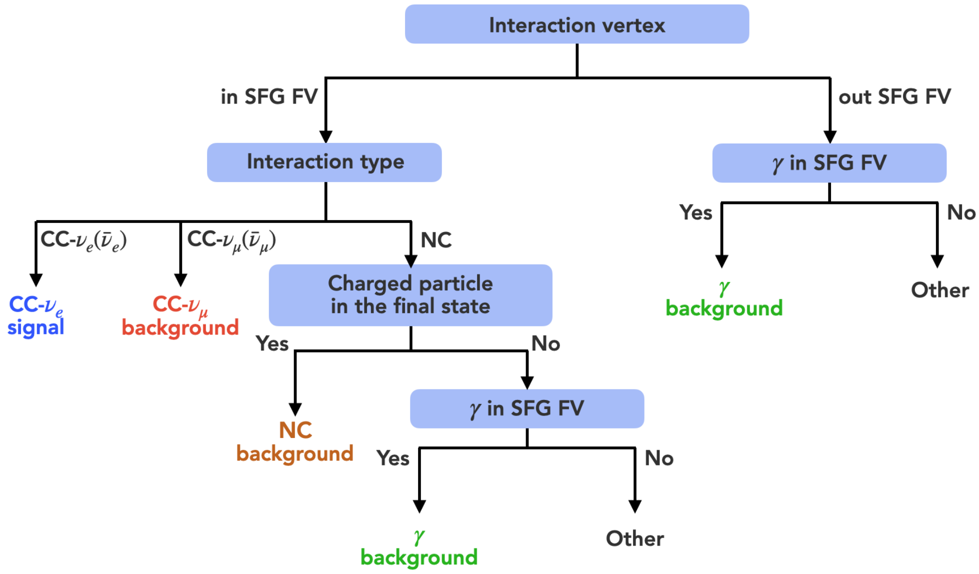

Figure 4.2: The classification of neutrino MC events based on the true information. They are classified based on the position of the neutrino interaction vertex, the number of charged particles in the final state of neutrino interaction, and if they have a γ conversion in the fiducial volume of SuperFGD. The fiducial volume of SuperFGD is shortly written as "SFG FV" in the figure.

The goal of this thesis is to select the CC-$\nu_e(\bar{\nu}_e)$ samples that has an interaction vertex inside the SuperFGD fiducial volume (FV). Thus, other samples are defined as backgrounds in this study. In this study, the fiducial volume of the SuperFGD is defined as the scintillator cube region excluding the outermost 2 layers. The classification of the neutrino MC events are shown in Figure 4.2. CC-$\nu_\mu(\bar{\nu}_\mu)$ events that have an interaction point in the SuperFGD FV are classified as ν_μ backgrounds. Besides, NC events in the SuperFGD FV with one or more primary charged particles are classified as NC backgrounds.

The most important background is the γ background. Here, we distinguish the γ samples from the CC and NC samples described above in order to study the effect of γ contamination separately. There are two types of γ backgrounds for this ν_e selection study. The first one is from NC interactions inside the SuperFGD FV and the secondary γ converts into electron-positron pair in the SuperFGD FV. The second one is from neutrino interactions out of the SuperFGD FV but have a γ conversion point in the SuperFGD FV. In this study, the former type is limited for the NC interactions without charged particles in the final state, otherwise the event is classified into the NC background sample. Events are also classified into the γ samples if the original neutrino interaction vertex is out of the SuperFGD FV and secondary photons convert into e^+e^- pair inside the SuperFGD FV.

Figure 4.3 shows the momentum distribution of γ backgrounds classified with the primary particle produced at neutrino interactions from which the γ is generated. Most γ backgrounds are coming from the π^0 generated from neutrino interactions. The type of the neutrino interaction of the γ backgrounds classified with the number of π^0 is shown in Figure 4.4. CC events have a larger fraction than that of NC events, while single π^0 events dominate in both of CC and NC cases.

The momentum distribution of γ backgrounds, classified with the position of the original neutrino interaction vertex, is also shown in Figure 4.5. The dominant γ backgrounds come from the Upstream-ECal (USECal) which is placed upstream the SuperFGD. Also, the second largest γ backgrounds are originated at not-detector components which are noted as the "other" in the plot.

Figure 4.6 shows the momentum and angular distribution of the γ backgrounds. The low momentum and forward-going γ samples dominate the γ background sample. This is because the γ backgrounds mainly come from the π^0 decay and tend to have a smaller momentum compared to the electrons (positrons) generated from neutrino interactions.

The number of events in each neutrino interaction MC samples are summarized in Table 4.1. The number of γ backgrounds in the magnet flux sample is roughly 2.2 times of that in the basket flux sample. This is because the magnet flux sample have additional γ background sources such as P0D ECal, Barrel ECal, and the magnet compared to the basket flux sample. Since the fraction of the target events is approximately $\sim 1\%$ to the total events, this selection is very challenging and requires an extremely good particle identification capability.

4.1.2 Particle gun sample

Particle gun samples are generated in order to study the behavior of each particle in the detector. They are also used for the training of the multivariate analysis in the following studies.

We generated five types of particle gun samples with different particle species: e^-, μ^-, π^+, p, and γ. e^- is the main target of this selection study since it is generated from ν_e interactions. When we select ν_e interaction, we have to identify the e^- track. Other particle species are considered as the background sources. μ^-, π^+, and p are mainly generated from neutrino inter-

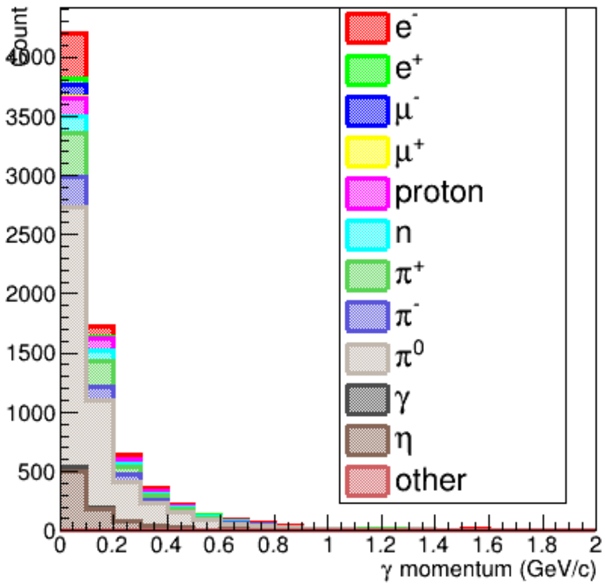

Figure 4.3: The momentum distribution of the γ backgrounds classified with the primary particle from which the γ background is generated. The magnet flux sample (1×10^{20} POT) is used.

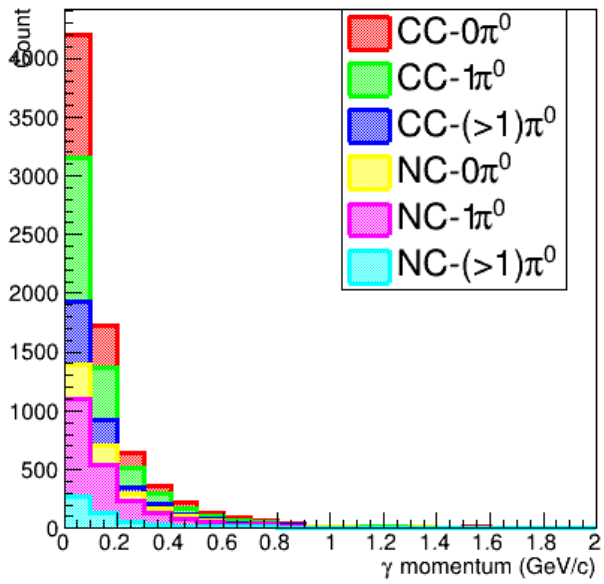

Figure 4.4: The momentum distribution of the γ backgrounds classified with the number of π^0 generated from the neutrino interaction where the γ background originated. The magnet flux sample (1×10^{20} POT) is used.

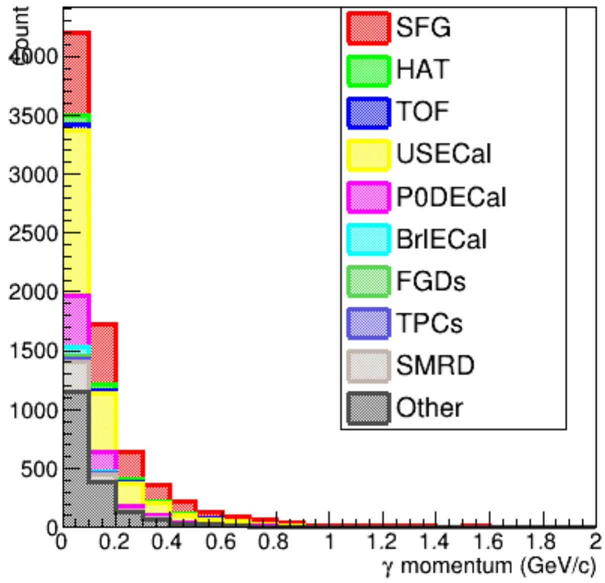

Figure 4.5: The momentum distribution of the γ backgrounds classified with the position of the neutrino interaction vertex from which the γ background originated. The magnet flux sample (1×10^{20} POT) is used.

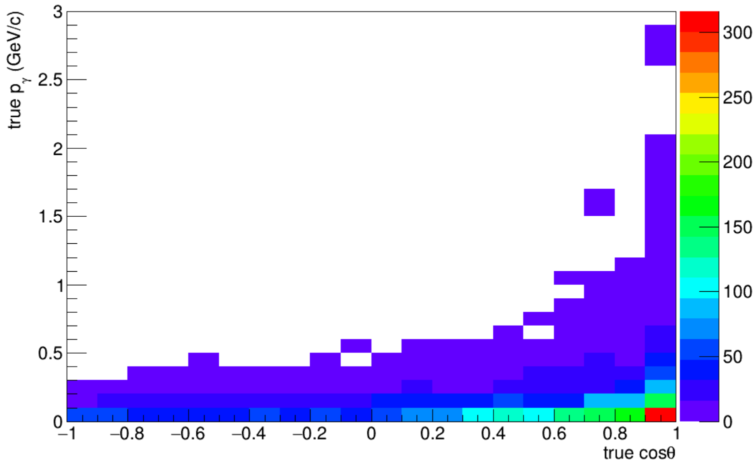

Figure 4.6: True momentum and angular distribution of the γ background samples using the magnet flux sample (1×10^{20} POT). Angle is plotted as the cosine of the angle between the true track direction and the beam direction (z-axis), which means that 1 corresponds to the forward scattering and -1 corresponds to the backward scattering.

Table 4.1: Event number in neutrino interaction samples.

	CC-ν_μ	CC-$\bar{\nu}_\mu$	CC-ν_e	CC-$\bar{\nu}_e$	NC	γ	Total
Basket flux (1×10^{21} POT)							
Total	1355733	38712	23537	1994	549337		1969313
Out FV	1207624	34149	20797	1743	514899		1779212
In FV	148109	4563	2740	251	34438	23346	213447
Magnet flux (1×10^{20} POT)							
Total	3011851	207283	48518	4437	4305609		7577698
Out FV	2996983	206792	48258	4407	4302225		7558665
In FV	14868	491	260	30	3384	5162	24195

Table 4.2: Characteristics of particle gun samples.

Particle	$e^-, \mu^-, \pi^+, p, \gamma$
Momentum	Weighted in [0, 3 GeV/c] using the neutrino interaction sample
Angle	Isotropic in 4π
Position	Uniform in the fiducial volume of SuperFGD

actions while μ^+, π^-, and n are generated in antineutrino interactions. This time we construct a selection algorithm for neutrino interaction (FHC mode) samples, thus we generated former three particles. Particle gun samples of γ are also generated to study the γ background rejection, which is the most crucial background for the ν_e selection.

Each event contains a single primary particle starting inside the SuperFGD FV. We generated particle gun samples with the weighted momentum distribution based on the magnet flux MC sample. The distribution of momentum weights for each particle gun samples are shown in Figure 4.7.

The characteristics of the particle gun samples are summarized in Table 4.2.

4.2 Reconstruction

4.2.1 Reconstruction overview

In the ND280 data processing flow, both data and MC samples are passed to the sub-detector reconstruction. Although the reconstruction tools for upgrade detectors including SuperFGD, HA-TPC, and TOF are currently work in progress, some of them for SuperFGD are already available. In

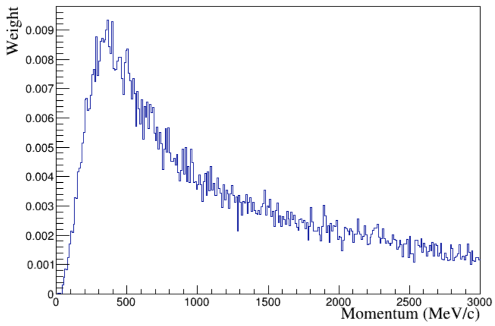

(a) e^-

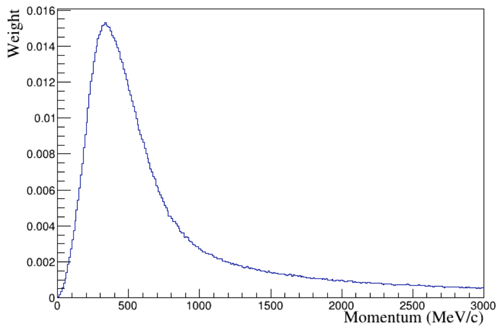

(b) μ^-

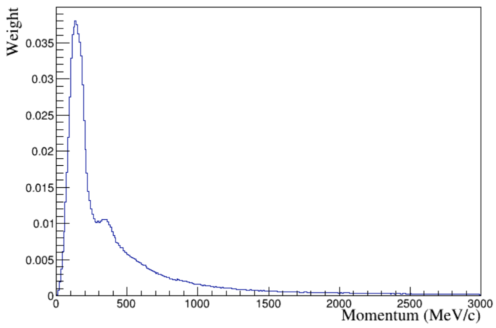

(c) π^+

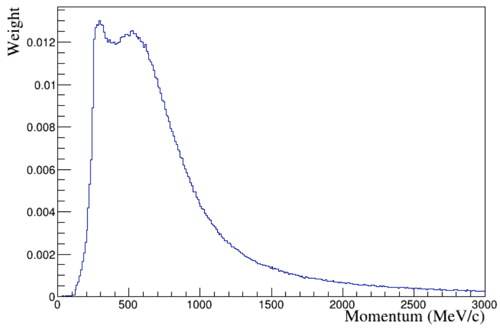

(d) p

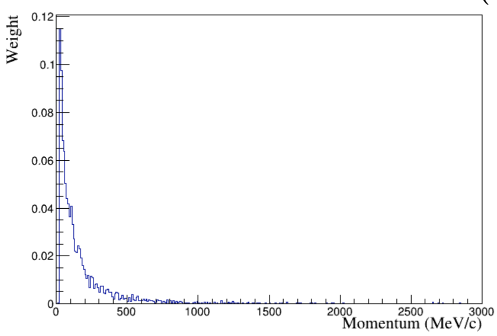

(e) γ

Figure 4.7: The distribution of the weight for each momentum bin that is used for generating the particle gun samples. The weight is calculated with NEUT.

Table 4.3: Number of events for particle gun samples.

Sample	e^-	μ^-	π^+	p	γ
Total (in FV)	89041	87940	79297	88626	122894
Reconstructed	88458	87333	78305	77317	122037
Efficiency (%)	99.3	99.3	98.7	87.2	99.3

SuperFGD reconstruction, we take 2-dimensional MPPC hit projections for three orthogonal directions as inputs. We first convert this group of 2D hits into 3D cube hits. Then neighboring cube hits are classified into a cluster or track object based on their positions and timings. In the SuperFGD reconstruction, tracks are defined as an object with four or more hits. Other objects with less hits than the criteria are defined as clusters. The details of the reconstruction process are explained in Appendix C.

4.2.2 Reconstruction result for particle gun sample

We test the reconstruction efficiencies for particle gun samples. Particles are regarded as reconstructed if there is a track object that is starting within 2 cm sphere around the true starting position. For γ samples, the starting position is defined as the conversion point of the γ, while it is the position of the particle gun for other samples. Figures 4.8 and 4.9 show the reconstruction efficiency as a function of the momentum and angle, respectively. The reconstruction efficiencies for protons with a momentum less than 300 MeV/c are low. This is because low momentum protons usually come to rest before traveling enough distance (four or more cubes) in order to be reconstructed as a track.

The number of reconstructed events are summarized in Table 4.3. These reconstructed samples will be used in the following study.

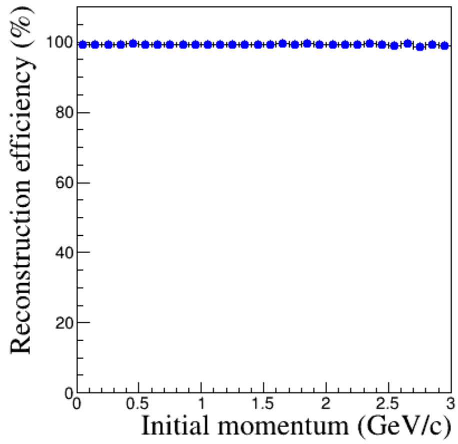

(a) e^-

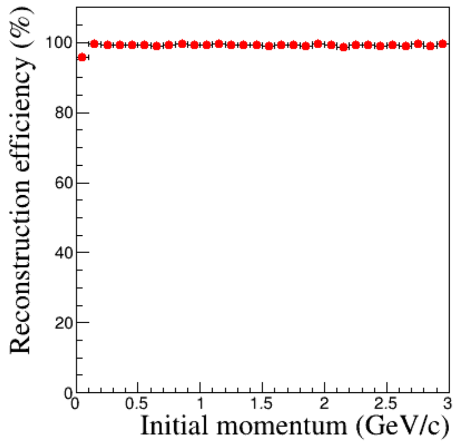

(b) μ^-

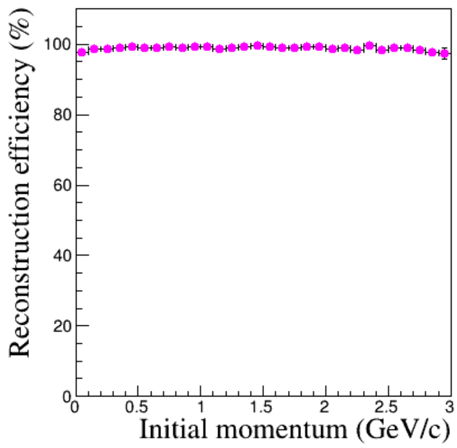

(c) π^+

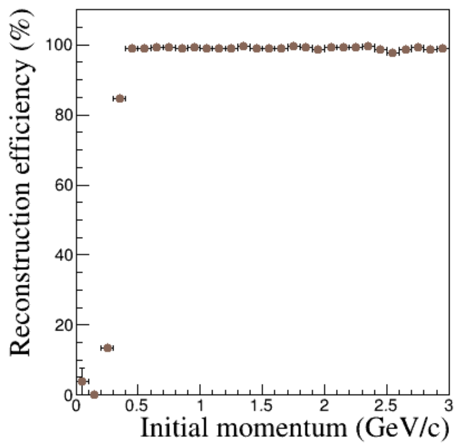

(d) p

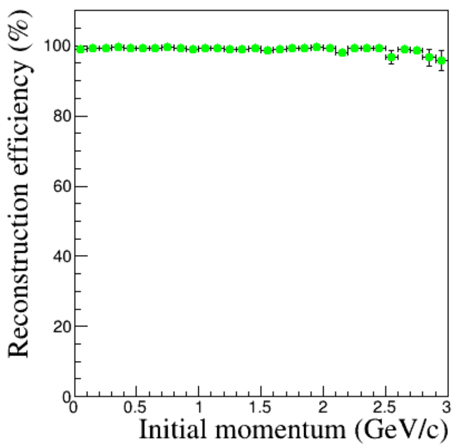

(e) γ

Figure 4.8: Reconstruction efficiencies for particle gun samples as a function of the momentum.

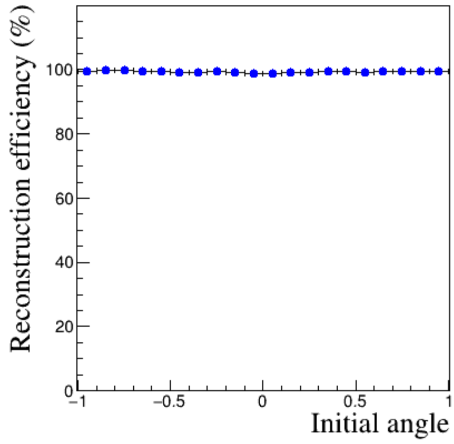

(a) e^-

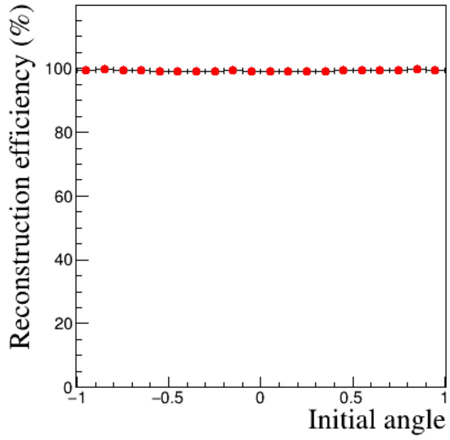

(b) μ^-

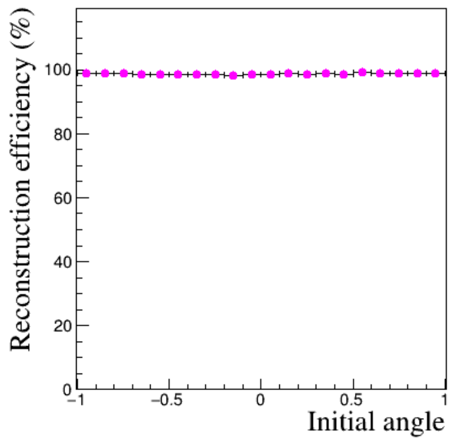

(c) π^+

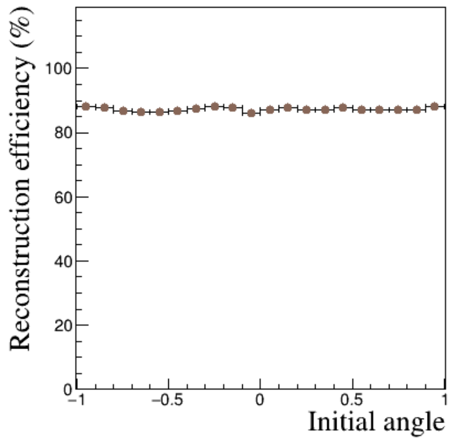

(d) p

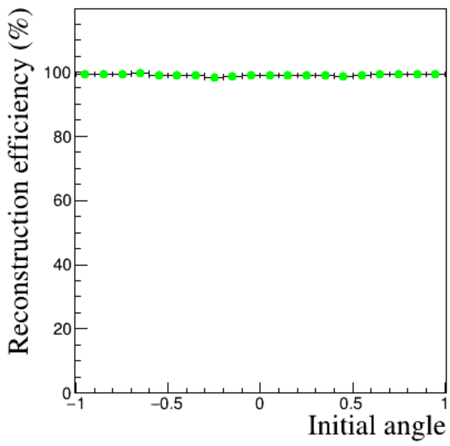

(e) γ

Figure 4.9: Reconstruction efficiencies for particle gun samples as a function of the angle.

Chapter 5

Electron selection algorithms

In this chapter, we explain a particle identification algorithm for electrons (positrons) produced from $\nu_e(\bar{\nu}_e)$ interactions. The overall selection flow for electrons in SuperFGD is shown in Figure 5.1. We first construct a cone object which contains all the reconstructed tracks and clusters in the forward region of the primary track. For electron and positron case, this corresponds to the electromagnetic (EM) shower. Then we apply a quality cut based on the number of hits in cone to make sure that the following selections work well. As a second cut, we apply a timing cut to reject events with a secondary Michel electron signal. Thirdly, in order to reject apparent hadron candidates with a visible scattering point, we apply a kink cut. Then, we apply an EM shower selection based on a multivariate analysis. Finally, γ cut is applied in order to reject electron (positron) tracks originated from a gamma conversion.

5.1 Electromagnetic shower reconstruction

In the reconstruction step, all reconstructed objects are classified into track or cluster objects. The classifications of the reconstructed tracks used in this study are shown in Figure 5.2. In this study, the true interaction vertex position is given and tracks starting from the true vertex are called primary tracks. Tracks that are in contact with the primary tracks are called connected tracks. These primary and connected tracks are used as the base tracks in the following cone construction step. Tracks that are not in contact with the base tracks are called distant tracks.

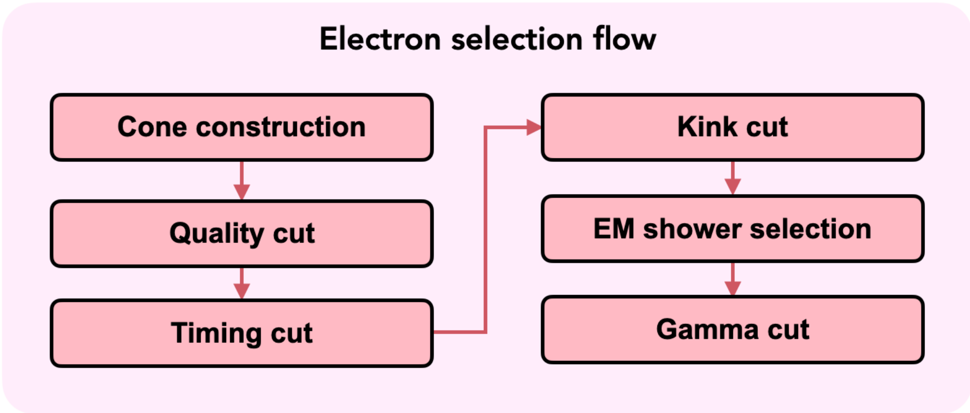

Figure 5.1: Electron selection flow for SuperFGD.

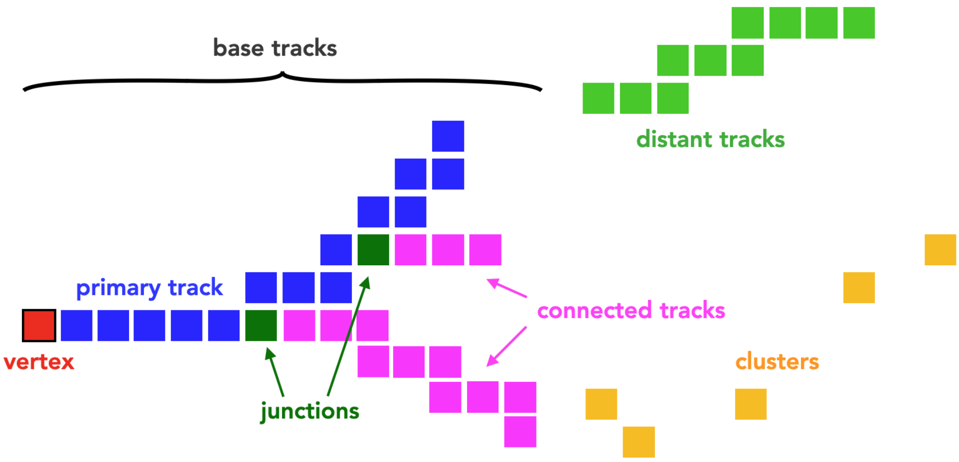

Figure 5.2: Classification of reconstructed track objects.

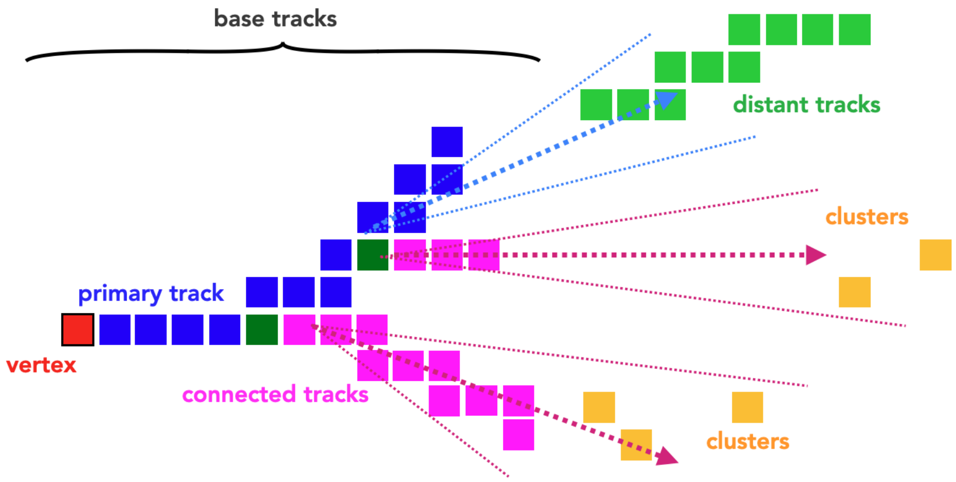

Figure 5.3: Schematic image of the cone construction.

5.1.1 Cone construction

In order to construct a cone object from each primary track, we check the spatial relationships between all distant objects and the primary track.

Figure 5.3 shows the illustration of the cone construction method. We iterate through all the base tracks including the primary track and connected tracks, and construct a cone for each of them. The starting position of the base track is used as the cone vertex and the track direction at the starting position is used as the cone axis. Then we check whether the distant track and cluster objects are within the cone or not. If the object is within the cone, it is matched to the base track. When a distant object is inside the several cones from different primary tracks, it is matched to the closest base track.

The cone angle is decided based on the study with neutrino interaction MC samples. The desirable cone angle is the one which maximize the fraction of the energy deposit within cone to the total energy deposit produced from the primary particle. It is also required to minimize the contamination of energy deposit originated from other primary tracks. These conditions are defined as a cone efficiency and a cone purity, respectively. The efficiency and the purity of the energy deposit with several cone angles are shown in Figure 5.4. For the cone angle larger than 30°, the efficiency does not change so much. Thus, we set the cone angle at 30° in this study. At the energy region of a few hundreds MeV/c, electrons does not cause much EM shower because they lose their energy down to the critical energy immediately. The

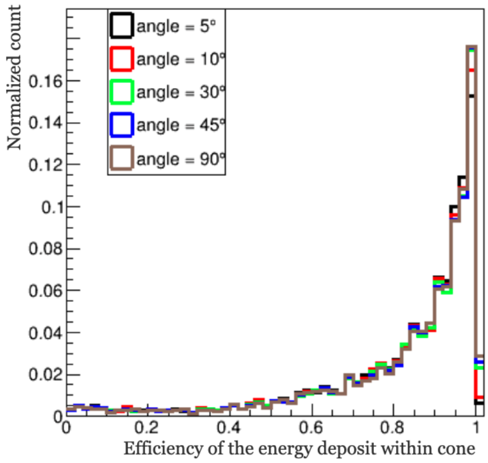

(a) Efficiency

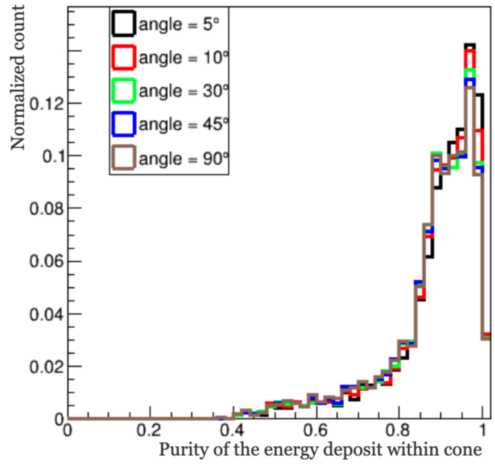

(b) Purity

Figure 5.4: The efficiency and the purity of the energy deposit within a cone with several cone angles. Both distributions are calculated with neutrino interaction MC samples generated by using NEUT.

dominant energy deposition comes from the base tracks which do not depend on the cone angle. As a consequence, the dependency of the energy deposit to the cone angle looks relatively small in Figure 5.4.

After constructing a cone, we require that there are 5 or more hits in the cone in order to make sure that the following selection works correctly. This is referred to as a quality cut.

5.1.2 Timing cut

Michel electron events are rejected by a timing cut. We calculate the hit timing difference between the primary track and other connected tracks. If the timing difference is large, the connected track is likely to be a Michel electron track. Figure 5.5 shows the maximum hit timing difference between the primary track and connected tracks for each particle gun sample. In the following study, we reject events whose timing differences is larger than 40 ns.

Some event displays of the events rejected with the timing cut is shown in Appendix E.

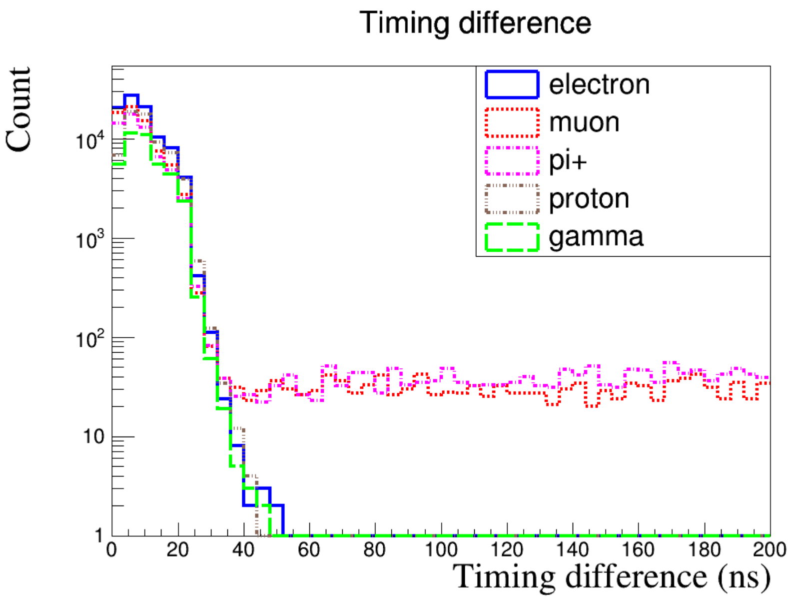

Figure 5.5: Maximum hit timing difference between the primary track and connected tracks.

5.1.3 Kink cut

Hadron scattering interactions can be characterized with kink-like structures. Thus, we reject tracks that have kinks. For the kink selection, we first require that there are only two out-coming tracks from the kink candidate. If the angle between the two tracks is larger than 45° and both of them have a length larger than 55 mm, we reject that event.

Figure 5.6 shows the number of kinks in each particle gun samples.

Some event displays of the events rejected with the kink cut is shown in Appendix E.

5.2 Electron identification using multivariate analysis

5.2.1 Discrimination variables

The particle identification (PID) for electrons consists of two successive steps. First we calculate several low-level discrimination variables and secondly combine them into the final PID output. Also, we handle tracks contained in

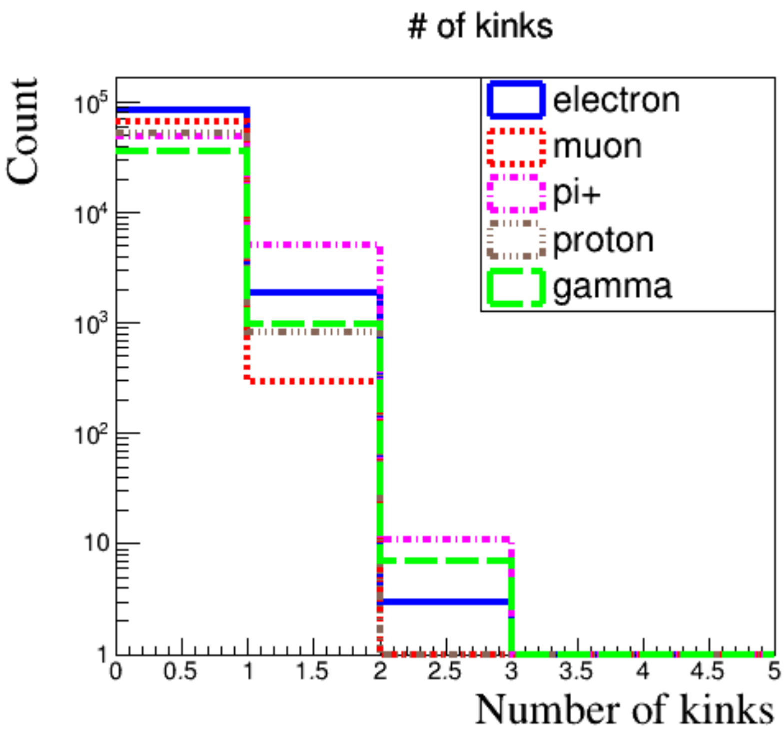

Figure 5.6: Number of kinks for each particle gun sample

SuperFGD and tracks escaping from SuperFGD separately since they behave differently due to the effects of Bragg peaks and electromagnetic showers. A track is defined as "escaping" if it has a hit in the outermost layer of the SuperFGD, otherwise it is defined as "contained". Generally, we expect that escaping tracks have much less information than that of contained tracks, which will give a weaker separations.

As for the first step, we introduce several variables that describe the shape, charge, and topological characteristics of the cone. As described previously, each cone is constructed with a primary track, connected tracks, matched distant tracks, and matched clusters. The numbers of these objects have topological information of the cone and vary according to the particle types. Thus, the number of connected tracks, matched tracks, and matched clusters are used in the multivariate analysis. Along with these variables, the length of the primary track, the energy loss of the primary track, and the total energy deposit in the cone are also passed to the multivariate analysis. Figures 5.7 and 5.8 show the distributions of these variables for contained and escaping particle gun samples.

In addition to the variables shown in Figures 5.7 and 5.8, we define five additional discriminating variables in order to describe the spatial and charge characteristics of the cone. The shape of a cone object is described by its depth and radius as shown in Figure 5.9. The cone vertex is fixed at the starting point of the primary track. The axis of the cone is defined as the direction from the cone vertex to the farthest hit in the cone. The cone depth is then defined as the distance between the vertex and the farthest hit. The cone radius is the maximum distance between hits and the cone axis.

Axis Max Ratio (AMR)

The axis max ratio (AMR) gives an indicator of how wide a shower is relative to its longitudinal length. Figure 5.10 shows the distribution of the cone depth and cone radius for each particle. Electrons and gammas have widely spread distributions compared to other particles as a result of the electromagnetic shower.

In order to take into account these differences, AMR is calculated by

$$\mathrm{AMR} = \frac{\text{cone radius}}{\text{cone depth}}. \tag{5.1}$$

For protons and MIPs, this value should be close to 0, while it is expected to be larger for EM shower cases. The distributions of AMR for each particle gun sample is shown in Figure 5.11. The distributions are shown both for contained particles and escaping particles.

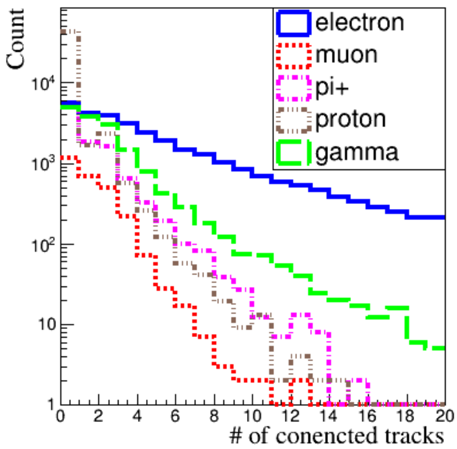

(a) Number of connected tracks.

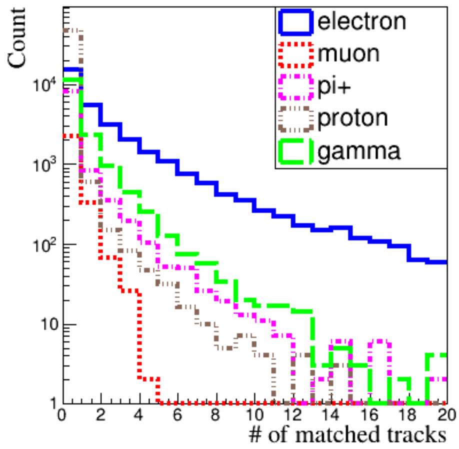

(b) Number of matched tracks.

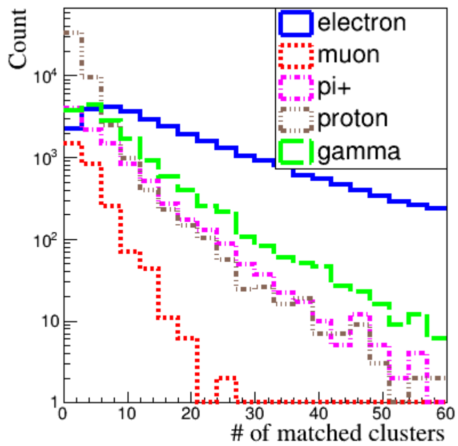

(c) Number of matched clusters.

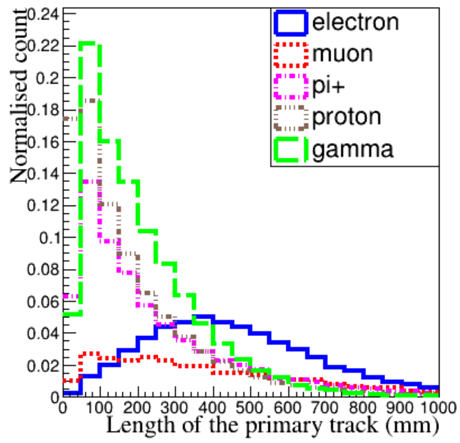

(d) Length of the primary track.

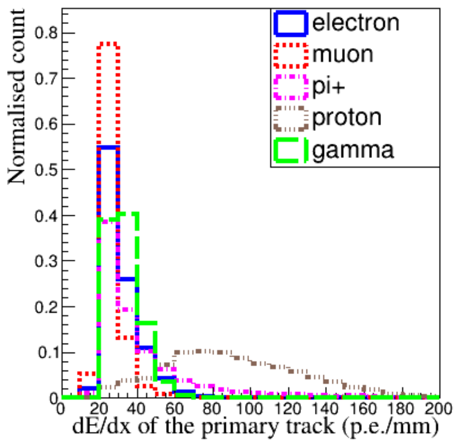

(e) dE/dx of the primary track.

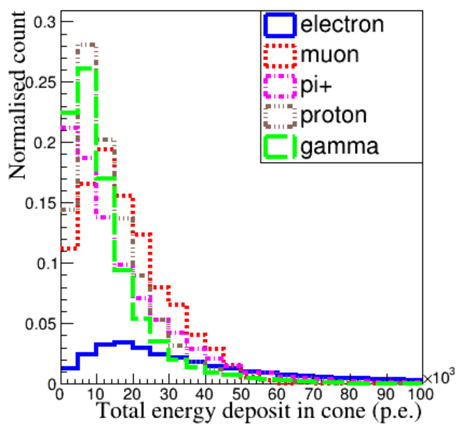

(f) Total energy deposit in cone.

Figure 5.7: Multivariate analysis input variables for contained tracks.

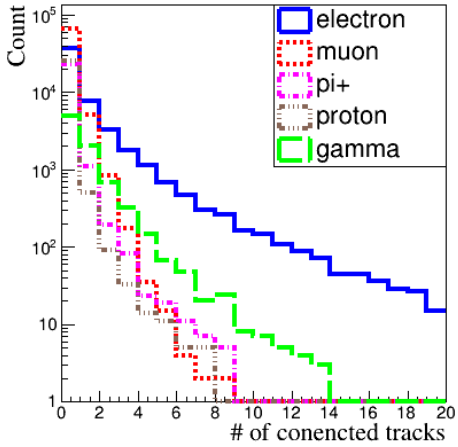

(a) Number of connected tracks.

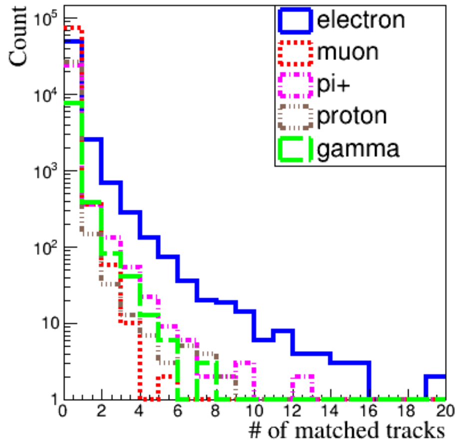

(b) Number of matched tracks.

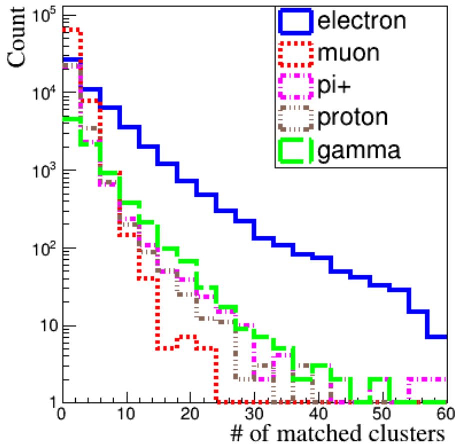

(c) Number of matched clusters.

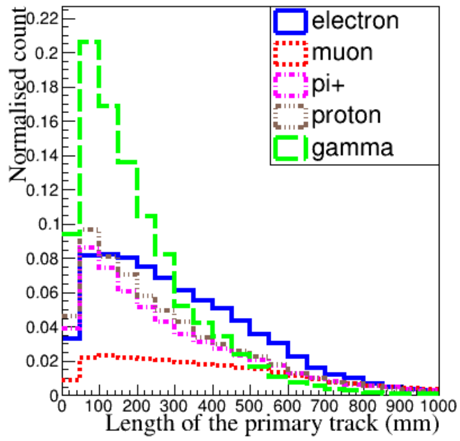

(d) Length of the primary track.

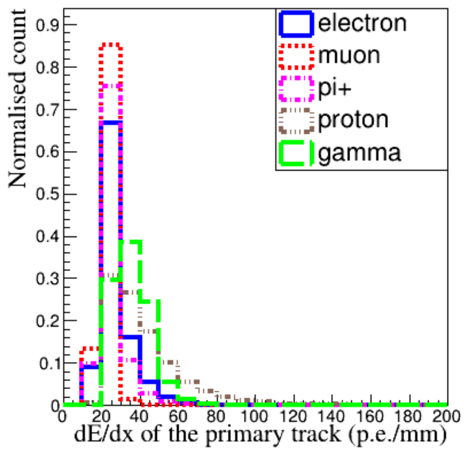

(e) dE/dx of the primary track.

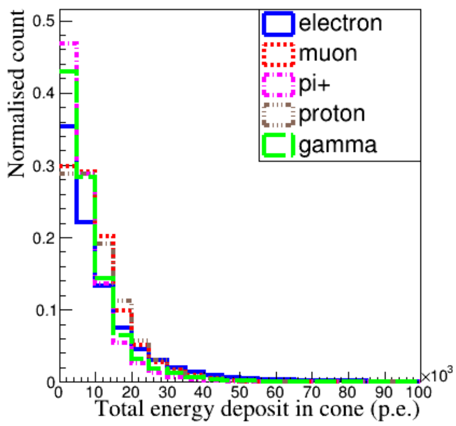

(f) Total energy deposit in cone.

Figure 5.8: Multivariate analysis input variables for escaping tracks.

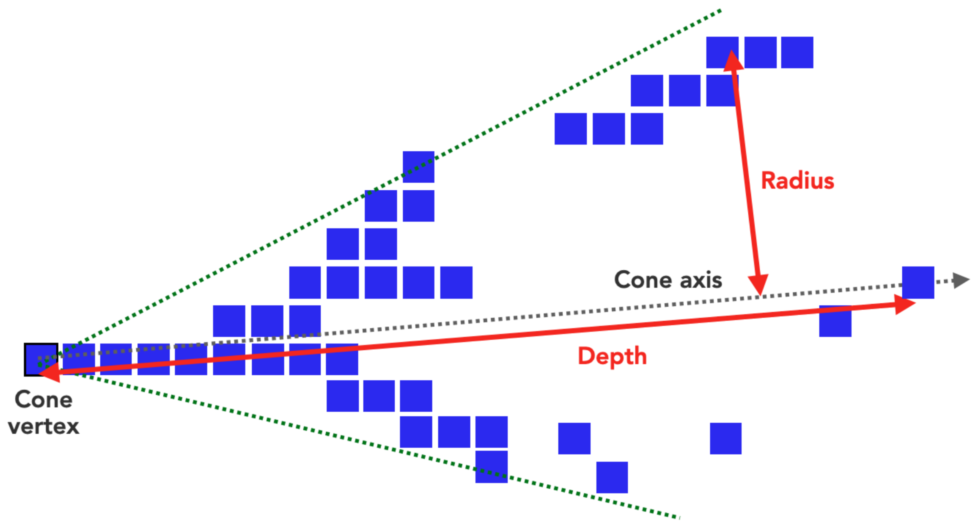

Figure 5.9: Definition of shower radius and depth based on the constructed cone object.

Truncated Max Ratio (TMR)

The truncated max ratio (TMR) gives a longitudinal charge distribution profile of the cone. We slice the cone along the shower axis for every 50 mm and take the ratio of the charge in the lowest charge slice to that in the highest charge slice. The most and least 20% energetic hits are removed so that it would be more robust to noises and very high hit charges. Protons lose their energy while traveling through the detector and give larger energy deposition toward the end point, which makes TMR smaller than other particles. MIPs should have a larger value since their mean energy loss do not change so much while they are traveling the detector medium. However, when a pion stops inside the detector, it gives a smaller value due to the Bragg peak. In addition, showers have smaller values compared to MIPs because of the large energy deposition around the shower peak. The distribution of TMR for each particle gun sample is shown in Figure 5.12.

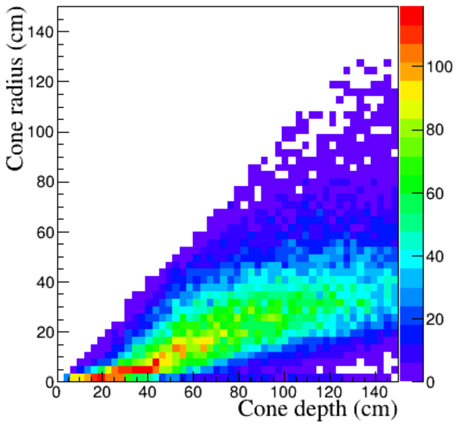

(a) e^-

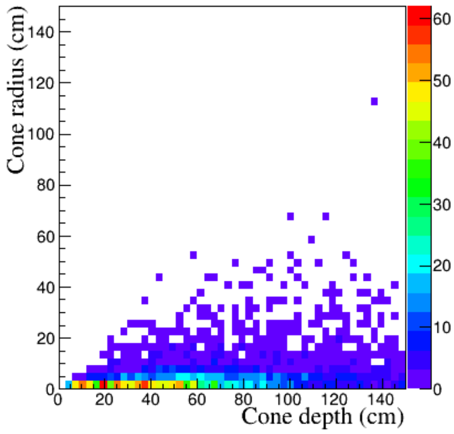

(b) μ^-

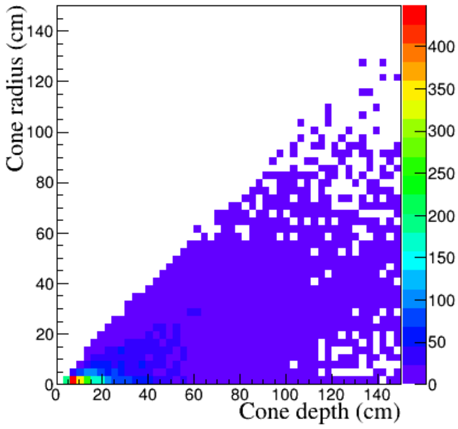

(c) π^+

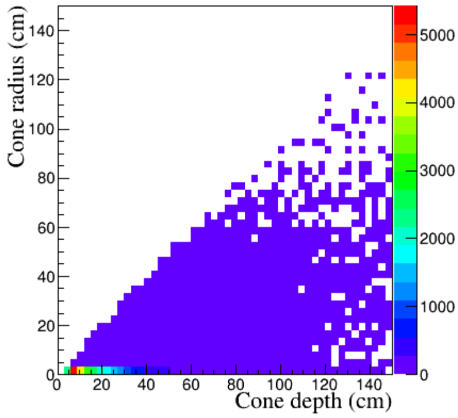

(d) p

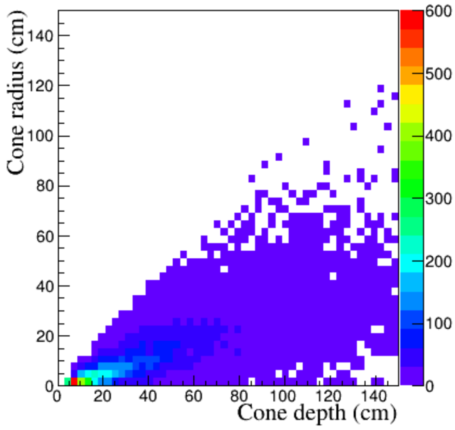

(e) γ

Figure 5.10: Distribution of the cone depth and cone radius for each particle gun sample.

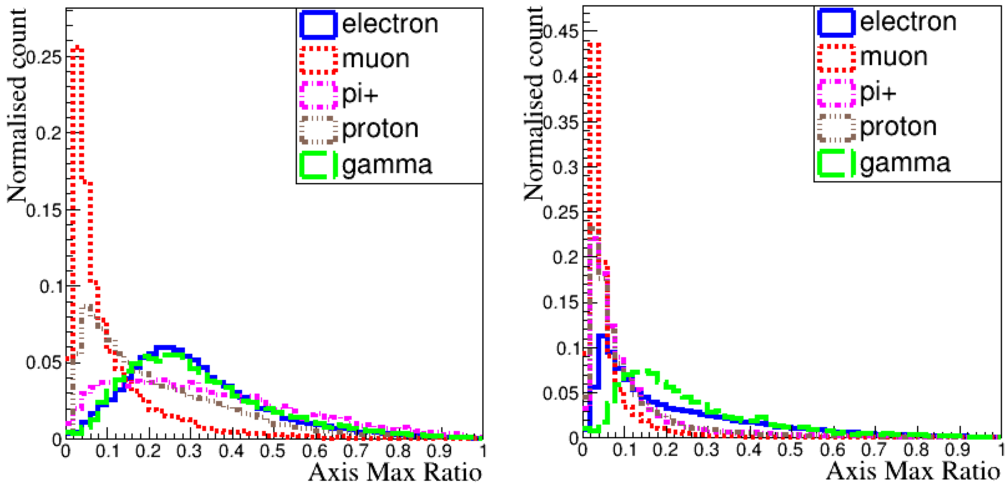

(a) Contained particles **(b)** Escaping particles

Figure 5.11: Axis max ratio (AMR) distributions for each particle gun sample.

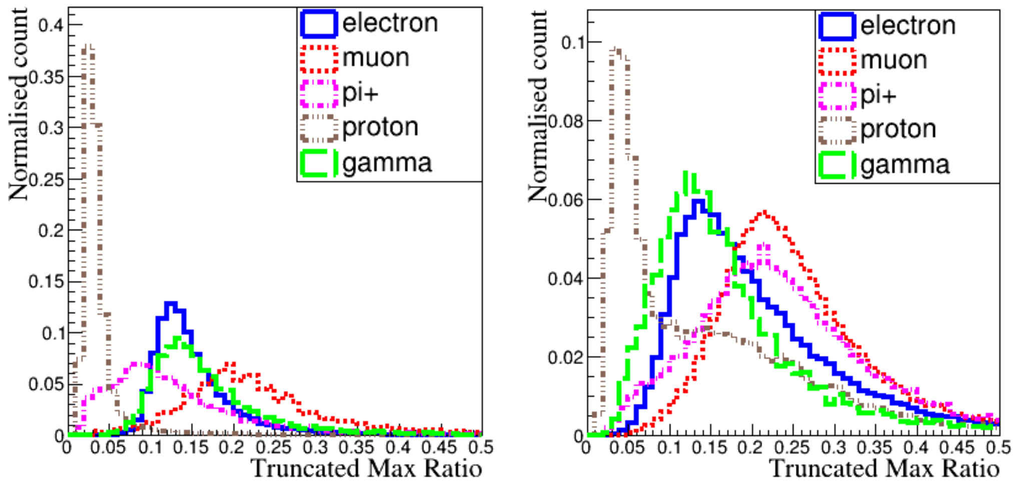

(a) Contained particles **(b)** Escaping particles

Figure 5.12: Truncated max ratio (TMR) distributions for each particle gun sample

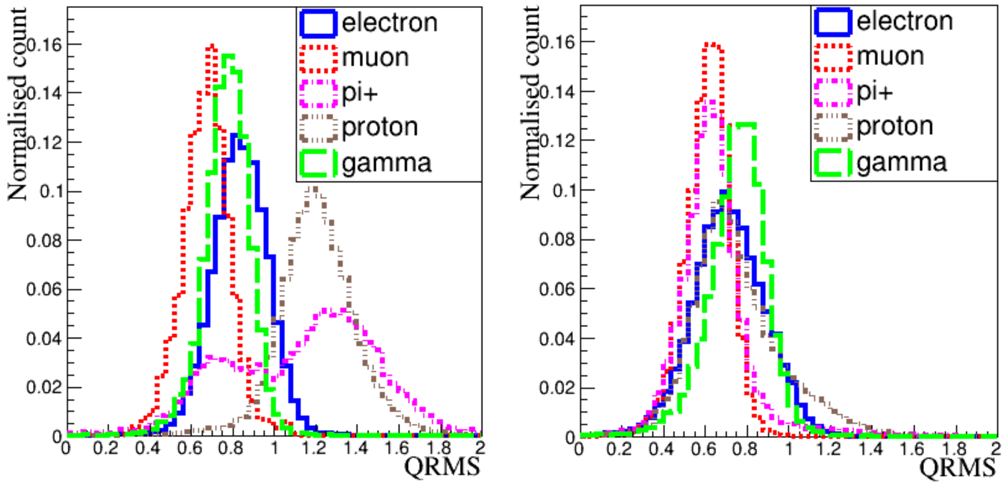

(a) Contained particles **(b)** Escaping particles

Figure 5.13: QRMS distributions for each particle gun sample.

Q Root Mean Square (QRMS)

The Q root mean square (QRMS) gives a variance of the hit charge distribution. It is defined as

$$q_{\mathrm{RMS}} = \frac{1}{\bar{q}} \sqrt{\sum_{i}^{N} \frac{(q_i - \bar{q})^2}{N}}, \tag{5.2}$$

where q_i is the charge of each hit, $\bar{q}$ is the mean hit charge and N is the number of hits within the cone. This value should be smaller for escaping tracks and larger for stopping tracks and showers. The distribution of QRMS for each particle gun sample is shown in Figure 5.13.

Front Back Ratio (FBR)

The front back ratio (FBR) gives a characteristic of the energy deposit in each end of the cone. Along the cone axis, we divide all the hits into four equal length quarters. Then the FBR is calculated by

$$\mathrm{FBR} = \frac{\text{Total charge in the back quarter}}{\text{Total charge in the front quarter}}. \tag{5.3}$$

MIPs should have an FBR value close to 1 while it will be larger when they stop inside the detector. Showering particles have smaller values because they deposit larger fraction of their energy towards the end of the shower. The distribution of FBR for each particle gun sample is shown in Figure 5.14.

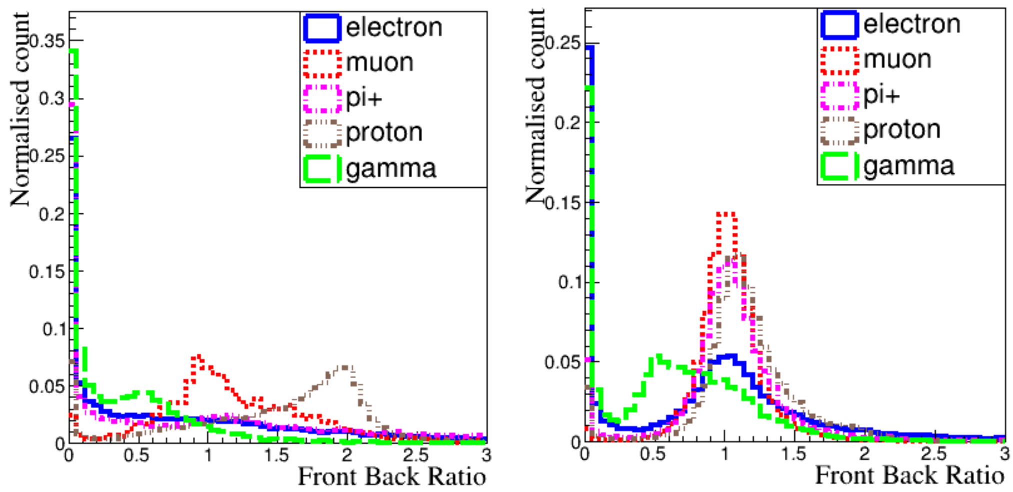

(a) Contained particles **(b)** Escaping particles

Figure 5.14: FBR distributions for each particle gun sample.

Maximum Hit Position (MHP)

The maximum hit position (MHP) gives the relative position of the most energetic hit in the cone. The position is expressed as a normalized depth of the hit. Stopping track have a value close to 1 while EM showers have smaller values. In addition to that, gammas should have a value very closer to 0 since they have a overlap region of an electron-positron pair around the starting point. The distribution of MHP for each particle gun sample is shown in Figure 5.15.

It is desirable that the input variables are independent of each other to simplify the construction of the PID discriminator. Figures 5.16, 5.17, 5.18, and 5.19 show the correlation matrices of the input variables for signal particle (e^-) and background particles (μ^-, π^+, p), respectively.

Some variables have correlations with each other in a certain sample, but not in all samples. For instance, there are strong correlations between TMR and QRMS for e^-, μ^- and π^+ samples, but it cannot be seen in the proton sample. In electron samples, the total energy deposit is also strongly correlated with the number of connected tracks and matched tracks though it has a correlation with the length of the primary track in other samples. As a conclusion, we adapt all of these variables as inputs for the multivariate analysis.

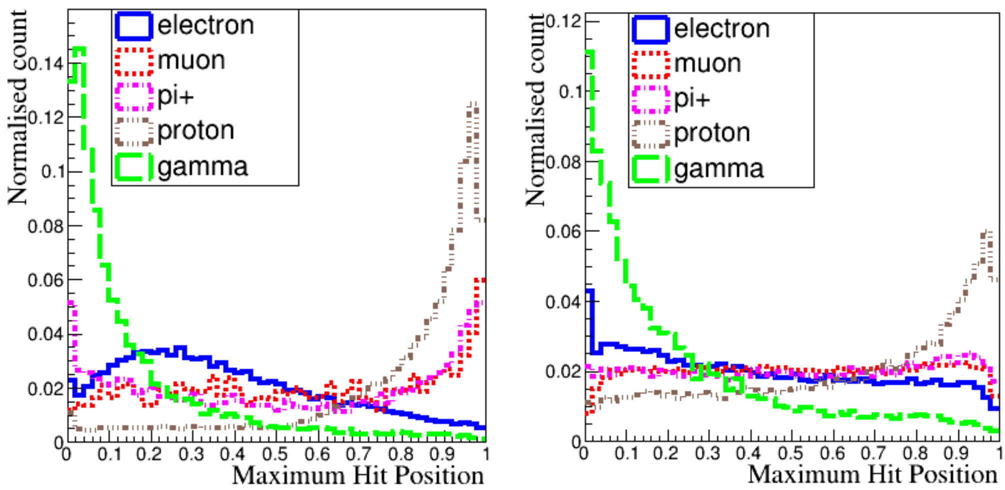

(a) Contained particles

(b) Escaping particles

Figure 5.15: MHP distributions for each particle gun sample.

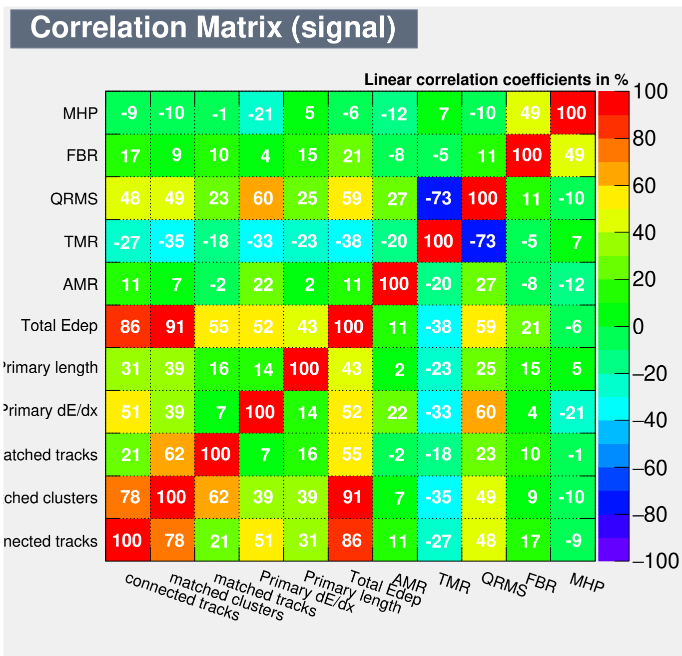

Figure 5.16: Correlation matrix of input variables for signal (e^-)

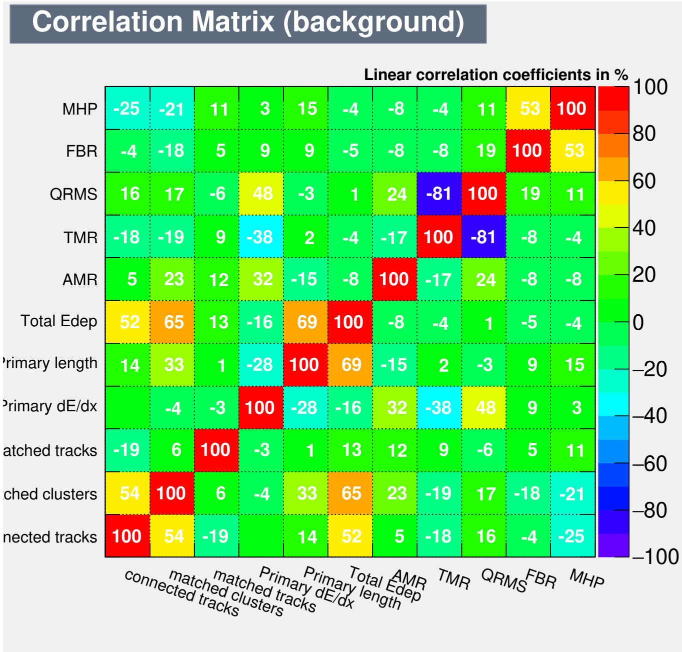

Figure 5.17: Correlation matrix of input variables for background (μ^-)

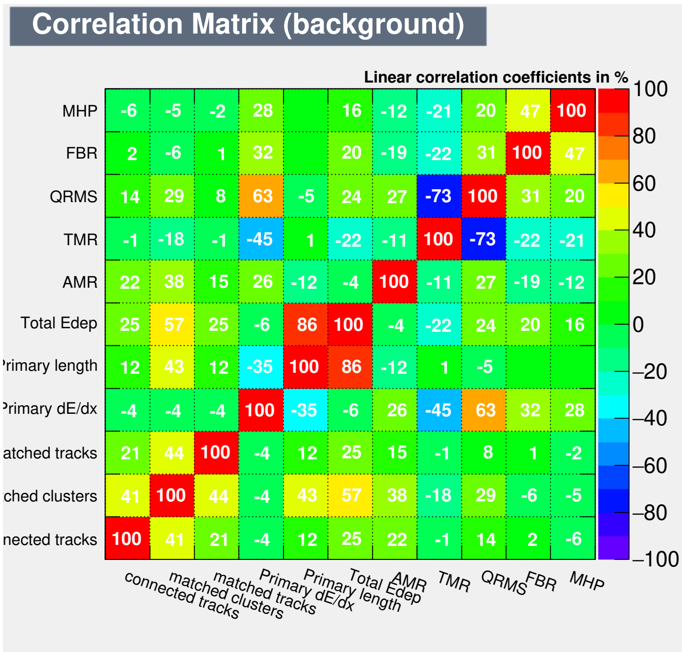

Figure 5.18: Correlation matrix of input variables for background (π^+)

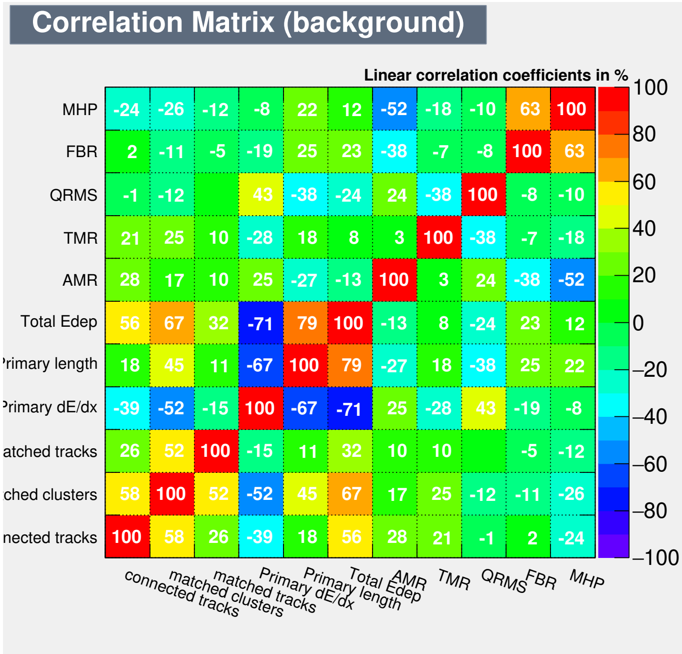

Figure 5.19: Correlation matrix of input variables for background (p)

5.2.2 Multivariate analysis

With the discrimination variables just introduced, we create 5 PID discriminators with using a multivariate analysis method:

- Contain_EM_MIP
  for separating contained e^-/γ from contained μ^-
- Contain_EM_HIP
  for separating contained e^-/γ from contained p
- Contain_EM_Pion
  for separating contained e^-/γ from contained π^+
- Escape_EM_MIP
  for separating escaping e^-/γ from escaping μ^-/π^+
- Escape_EM_HIP
  for separating escaping e^-/γ from escaping p

These variables give separations between the EM shower and other particles. We can select EM showers by combing these variables. Tracks have different input variable characteristics when they are contained in the detector or

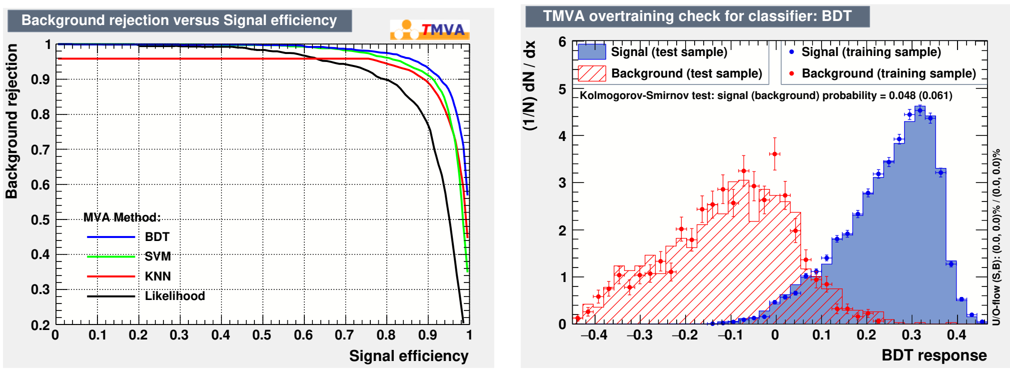

(a) ROC curve **(b)** BDT response

Figure 5.20: Training and test result for Contain_EM_MIP discriminator

escaping. Thus, we prepare three discriminators for contained tracks and two for escaping tracks. If the primary track has a hit in the outermost layer of the SuperFGD, it is assigned as escaping and applied with the discriminators for escaping events. Otherwise it is handled as a contained event.

In order to decide which multivariate analysis method to use for the PID discriminator construction, we compared the selection capability of several methods:

1. Boosted decision tree (BDT)
2. k-nearest neighbor method (kNN)
3. Support vector machine (SVM)
4. Maximum likelihood method (Likelihood)

Details of these methods are described in Appendix D.

Five discriminators are trained with corresponding particle gun samples. The results of the training and test of contained particle samples are shown in Figures 5.20, 5.21, and 5.22. Figures 5.23 and 5.24 show the results for escaping samples. As we expected, escaping tracks have weaker separation than that of contained tracks. This is because they do not have a Bragg peak or do not cause much EM shower before escaping, which gives less information for the PID. In every case, BDT shows the best separation, so we use BDT responses in the following selection.

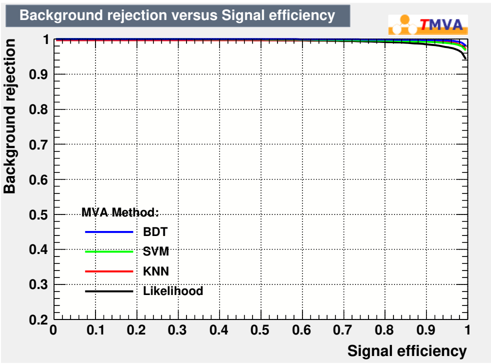

(a) ROC curve

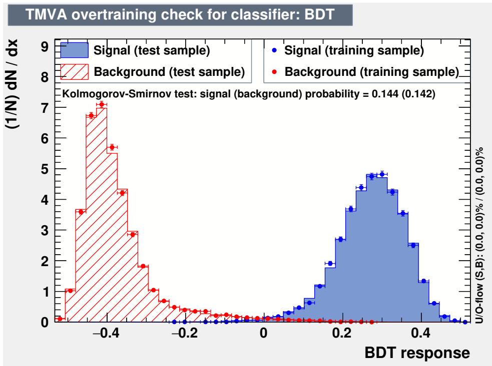

(b) BDT response

Figure 5.21: Training and test result for Contain_EM_HIP discriminator

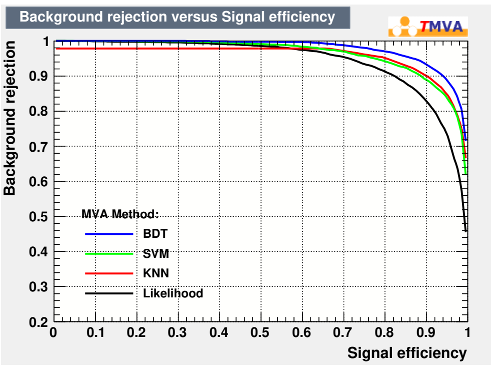

(a) ROC curve

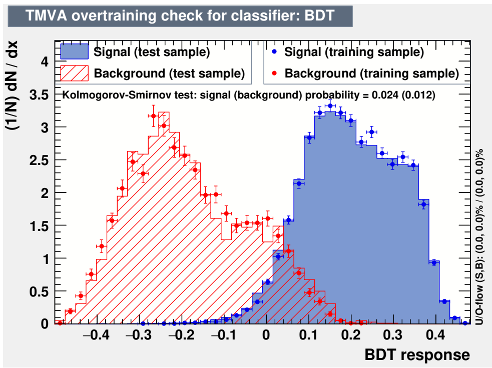

(b) BDT response

Figure 5.22: Training and test result for Contain_EM_Pion discriminator

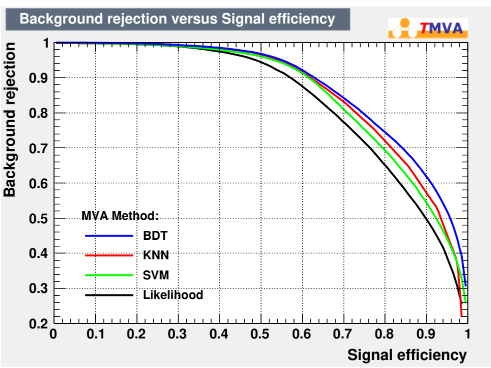

(a) ROC curve

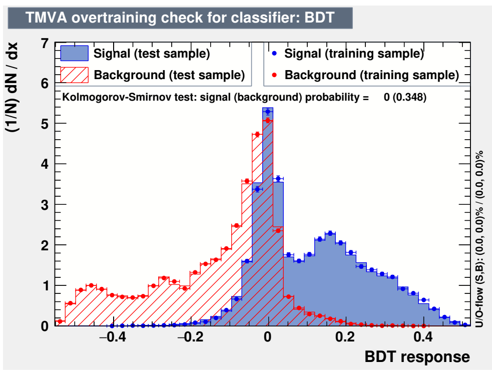

(b) BDT response

Figure 5.23: Training and test result for Escape_EM_MIP discriminator

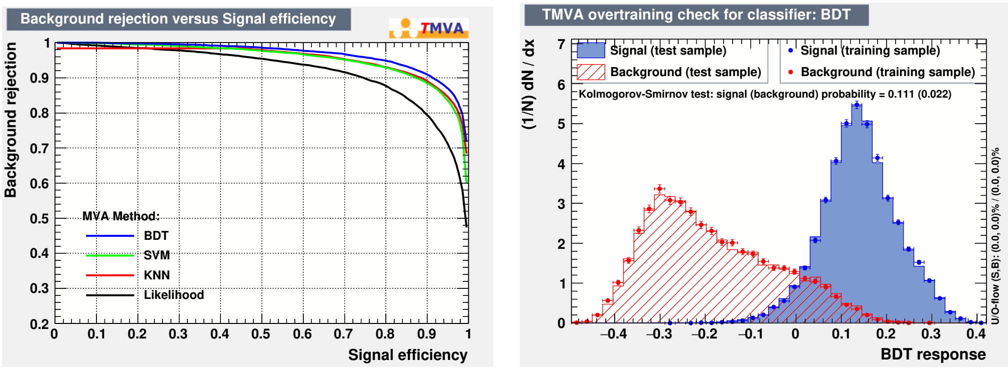

(a) ROC curve

(b) BDT response

Figure 5.24: Training and test result for Escape_EM_HIP discriminator

5.3 Gamma rejection

In order to select an electron track, it is not enough to select EM shower events since there is a huge contamination of gamma background. We apply a gamma cut after the EM shower selection.

5.3.1 Basic strategy for gamma rejection

Basic strategy of gamma rejection is to identify the gamma converted electron positron pair based on the energy deposit around the starting point. They pass through the same cubes until they are split by the magnetic field as shown in Figure 5.25. Thus, cubes where the electron and positron pair's trajectories are overlapped are expected to have the twice larger energy deposit than that of a single electron (positron) track.

5.3.2 Cube dE/dx method

Taking the full advantage of SuperFGD's high granularity, we calculate the energy loss of the particle in each cube along the primary track. This is called as a cube dE/dx method. Cube dE/dx is calculated from the charge and the path length in each cube after track fitting.

Figure 5.26 shows the cube dE/dx of first fifteen cubes for electrons and gamma events. Figure 5.27 shows the sum of them. For the cubes close to the starting point, we can clearly see two different peaks for electron samples and gamma samples. Gammas have a peak around 450 p.e./cm which is approximately twice larger than that of electrons. Since gamma converted electron-positron pair is split after traveling a few cubes, gamma samples

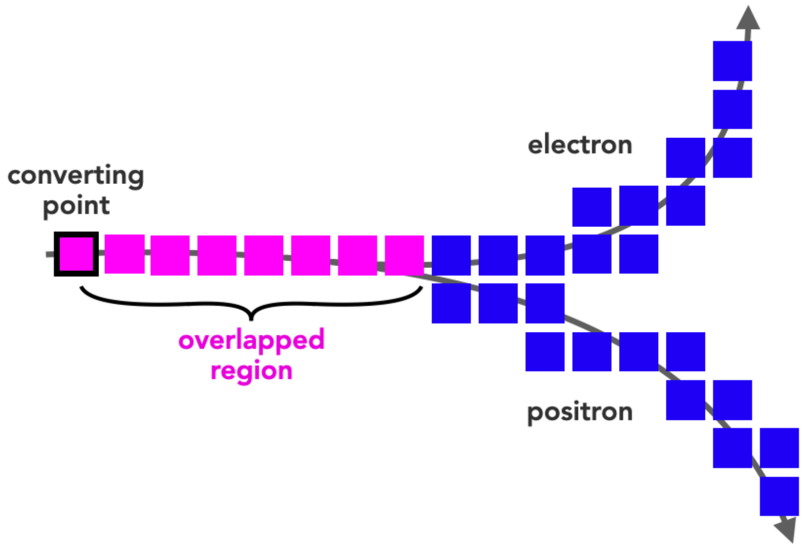

Figure 5.25: Schematic image of a gamma conversion

start to have a left-side tail, which finally gives almost the same peak as electrons. This is because gamma converted electron-positron pairs give the same energy loss as a single electron track after split.

5.3.3 Multivariate analysis

We use multivariate analysis methods to construct an $e^{\pm}/\gamma$ discriminator with the cube dE/dx values of first fifteen cubes. Also, we give the average dE/dx and the length between the starting point and the first junction point. Gamma converted electron-positron pairs tend to have shorter length compared to electrons. While electrons sometimes have no secondary tracks, gammas more likely to have secondary tracks because of the electron-positron pair splitting. Thus, the number of connected tracks is also fed to multivariate analysis. Figure 5.28 shows the distribution of these input variables. In Figure 5.28b, gamma samples show a two-peak distribution. As we have seen in Figure 5.26, the right-side peak corresponds to the overlap of the gamma converted electron-positron pair. Thus it shows that the segmentation of the gamma converted tracks is working correctly and we are correctly taking the average dE/dx of the overlap region. However, when they have asymmetric energies and one of them cannot be seen clearly, it can fail to find the correct junction point. In that case we could take the average dE/dx of not-overlapped region, which gives a smaller value of dE/dx.

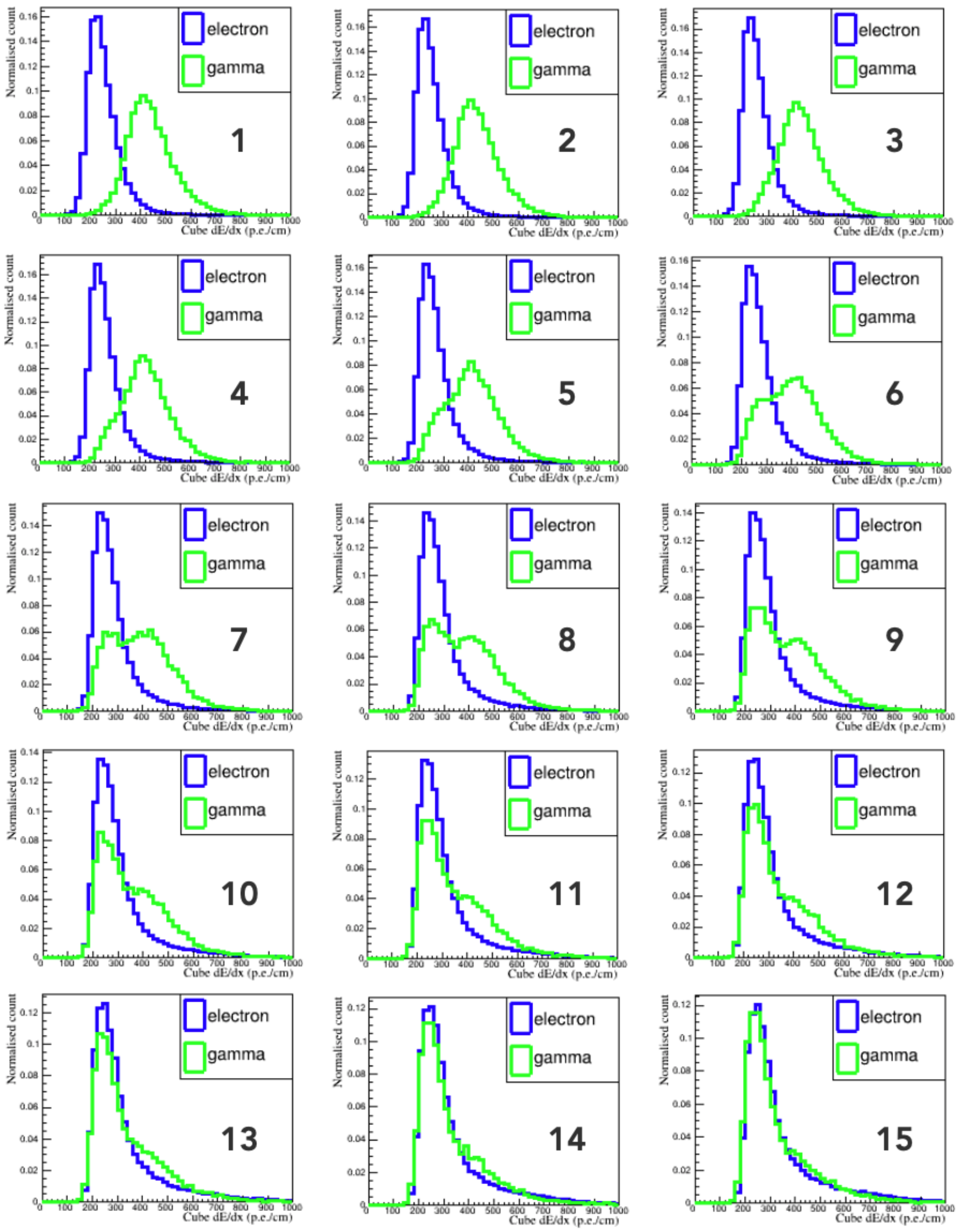

Figure 5.26: Cube dE/dx distributions of first fifteen cubes for electron and gamma particle gun samples. For each distribution, the area is normalized to 1.

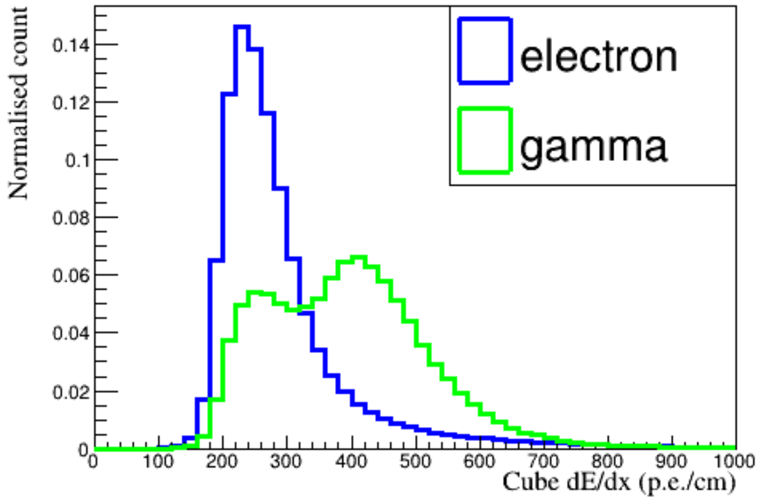

Figure 5.27: Cube dE/dx distribution of all the first fifteen cubes for electron and gamma particle gun samples. For each distribution, the area is normalized to 1.

Training of the $e^{\pm}/\gamma$ discriminator is done with particle gun samples. The result is shown in Figure 5.29.

For $e^{\pm}/\gamma$ discriminator, BDT shows the best separation. Thus we use BDT response in the following selection analysis.

5.4 Evaluation with particle gun samples

We evaluated the electron selection efficiency with particle gun samples.

The response of each PID discriminator is shown in Figure 5.30. All of them give a good separation of the signal and background samples.

The PID discriminator responses as a function of the particle momentum for signal and background samples are shown in Figures 5.31 and 5.32, respectively. At the low momentum region, the responses of Contain_EM_MIP and Contain_EM_Pion for electrons get worse and have some overlaps with that of the background samples. This is because low momentum electrons does not have enough energy to produce EM shower and behave as a MIP track. High momentum protons have closer responses to that of electrons. This is also because protons behave as a MIP at the region above a few GeV/c. Since escaping protons does not have a clear Bragg peak, this effect is much clearer for the Escape_EM_HIP response.

The PID discriminator responses as a function of the particle angle for

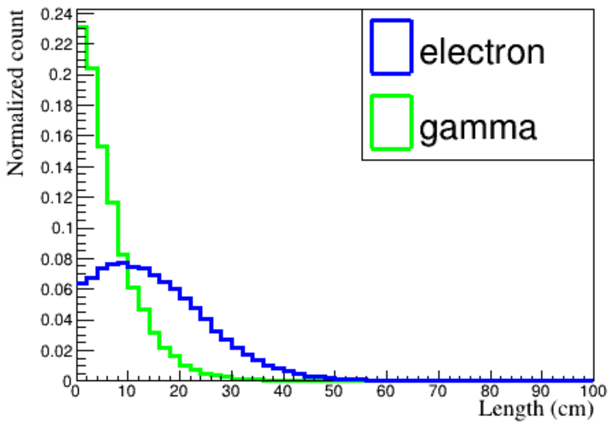

(a) Length between the starting point to the first junction.

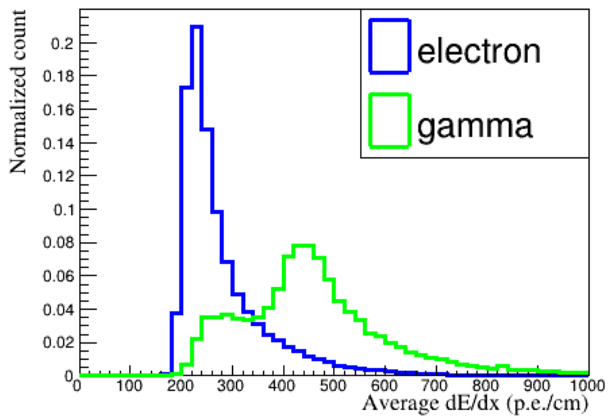

(b) Average dE/dx between the starting point to the first junction.

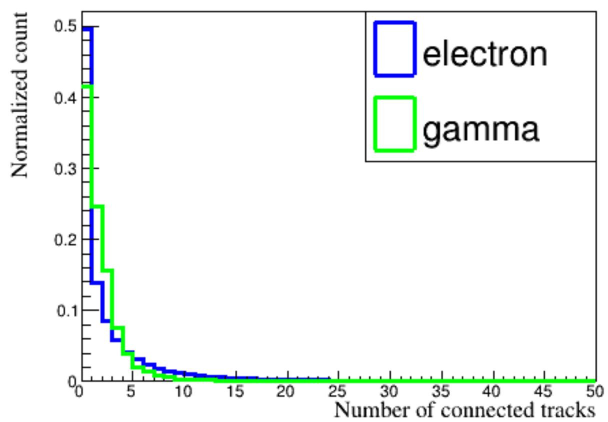

(c) Number of connected tracks.

Figure 5.28: Input variables for $e^{\pm}/\gamma$ discrimination

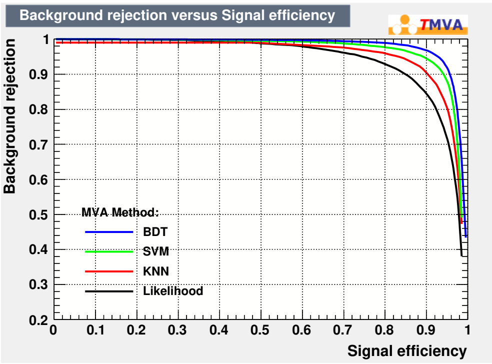

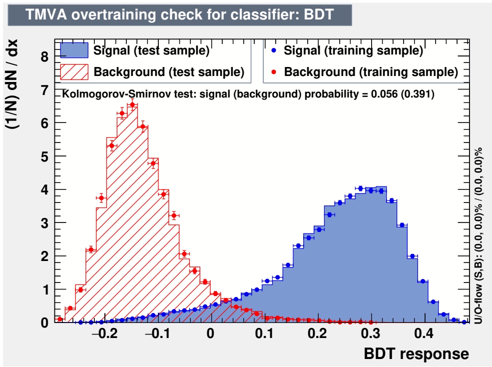

(a) ROC curve

(b) BDT response

Figure 5.29: Training and test result for E_Gamma discriminator

signal and background samples are shown in Appendix E.

We set threshold for each discriminator to select electron samples. Thresholds are decided so that the misidentification rate of the background particle should be less than 1%. For contained events, thresholds are

$$\begin{aligned} &\text{Contain\_EM\_MIP} > 0.15 \\ \& \quad &\text{Contain\_EM\_HIP} > 0.0 \\ \& \quad &\text{Contain\_EM\_Pion} > 0.15 \\ \& \quad &\text{E\_Gamma} > 0.1. \end{aligned} \tag{5.4}$$

For escaping events, we set more strict thresholds as:

$$\begin{aligned} &\text{Escape\_EM\_MIP} > 0.2 \\ \& \quad &\text{Escape\_EM\_HIP} > 0.15 \\ \& \quad &\text{E\_Gamma} > 0.1, \end{aligned} \tag{5.5}$$

in order to reduce the contamination of the backgrounds.

The number of selected events at each step is summarized in Table 5.1. For contained events, we achieved 50% efficiency for electron samples while keeping the misidentification rates for other particles less than $\sim 0.5\%$. This selection capability satisfies the required precision for the ν_e selection. The EM selection cut works extremely well and reduce the misidentification rate for other particles with the order of 100 or more. Also, the gamma cut reduces gamma contribution to 1/50.

For escaping particle gun samples, the efficiency gets lower than the contained ones. This is because escaping electrons does not cause much EM shower in the detector and hard to be tagged. However, the misidentification rates for other particles are good enough to perform the ν_e selection.

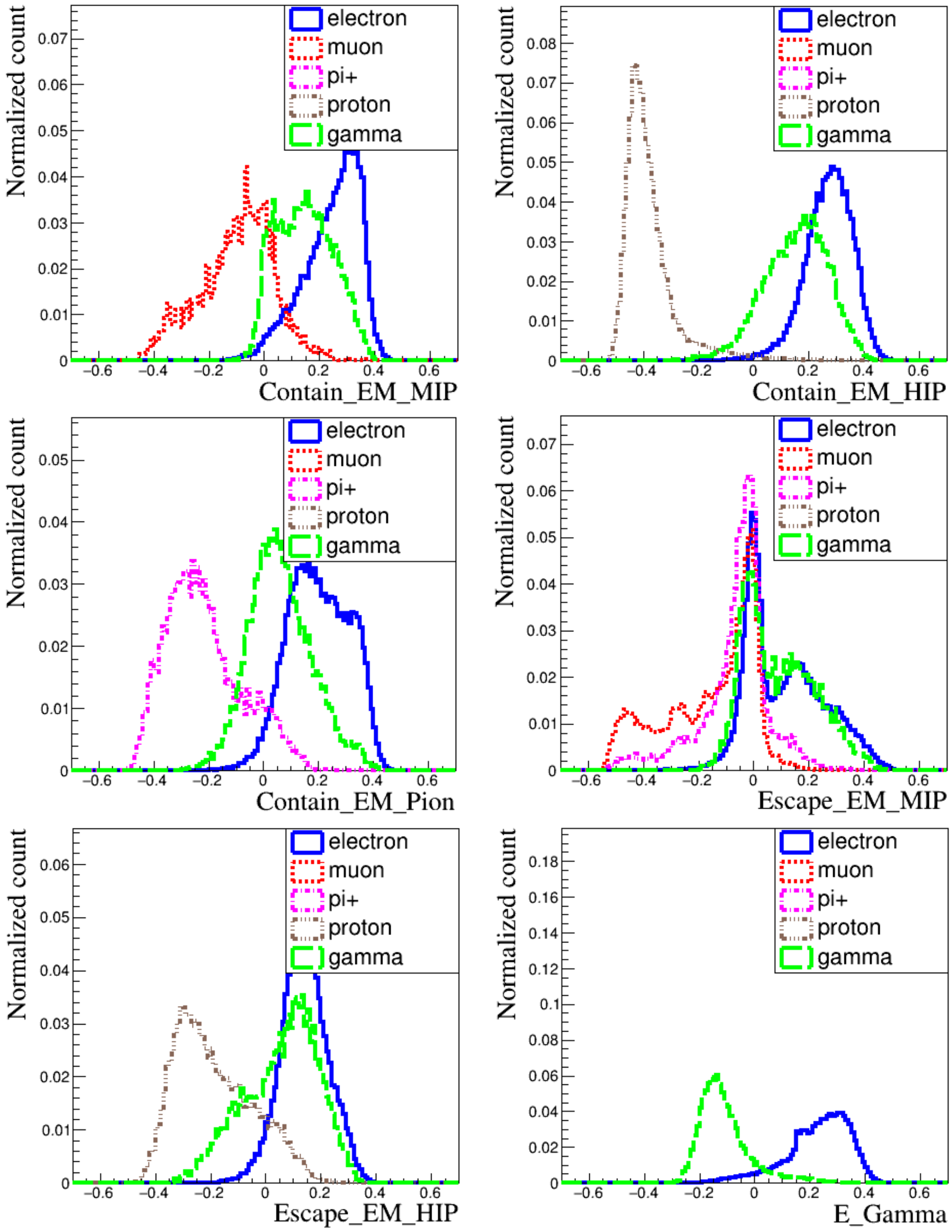

Figure 5.30: PID discriminator responses for each particle gun samples.

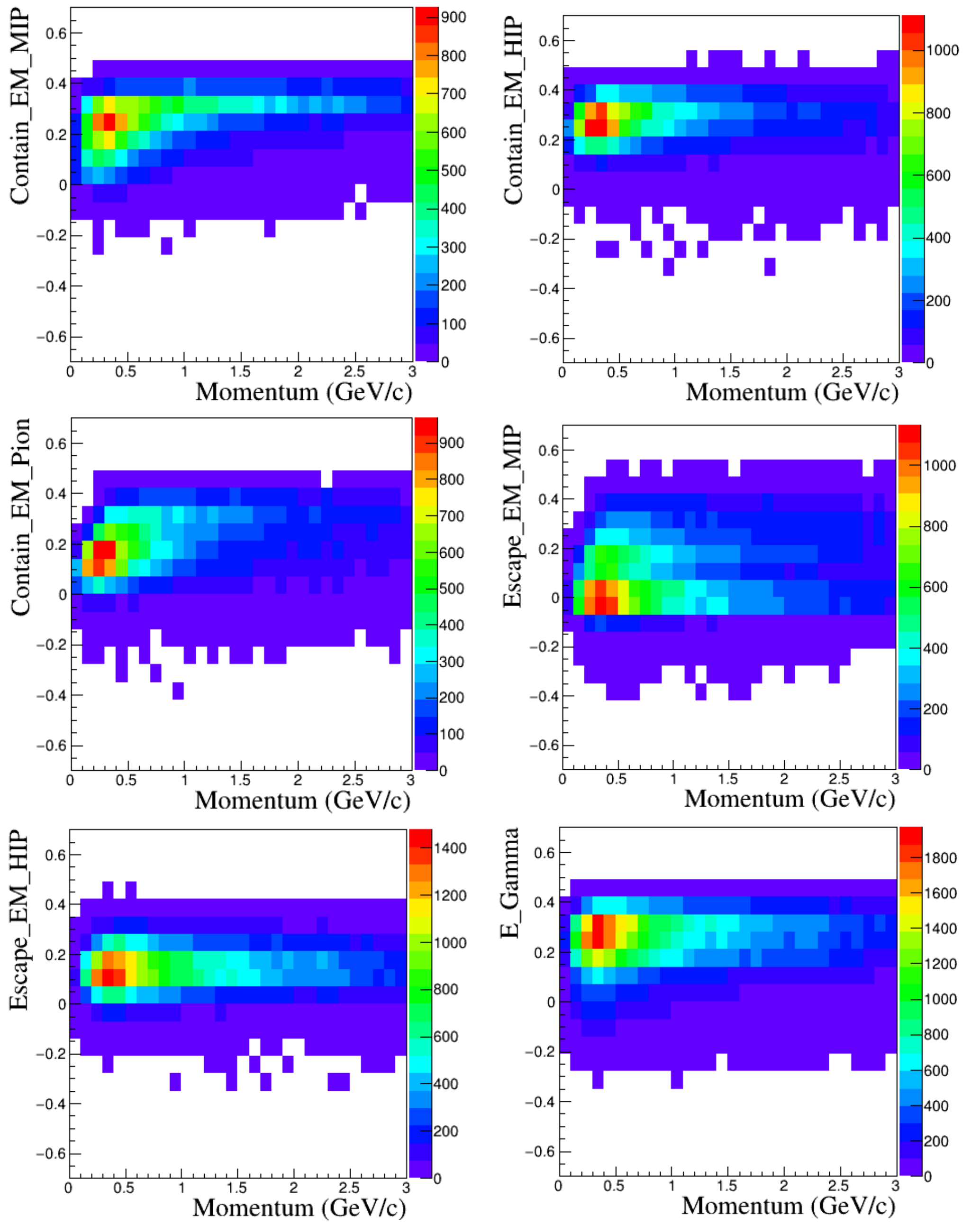

Figure 5.31: PID discriminator responses as a function of the momentum for signal (e^-) particle gun samples.

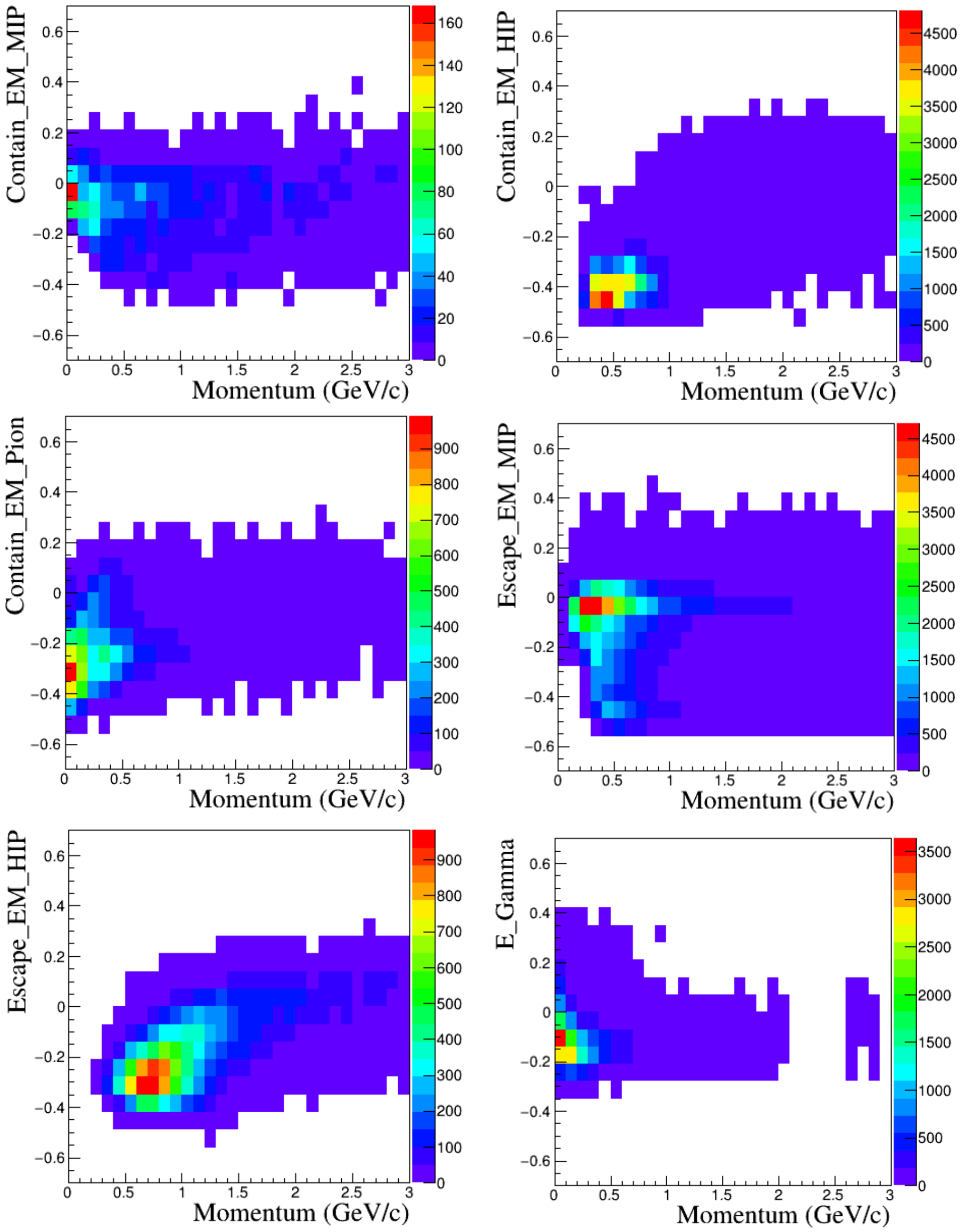

Figure 5.32: PID discriminator responses as a function of the momentum for background particle gun samples.

Table 5.1: Selection results with particle gun samples.

	e^-	μ^-	π^+	p	γ
Contained	34243	12987	51013	50322	18286
Quality cut	34157	12978	50822	50235	18189
Timing cut	34130	3279	17979	49371	18188
Kink cut	32588	3016	14754	48252	17557
EM selection	20061	29	44	27	3462
Gamma cut	18433	27	35	16	91
Efficiency (%)	53.82	0.2	0.06	0.03	0.49
	e^-	μ^-	π^+	p	γ
Escaping	54215	74346	27292	26995	9071
Quality cut	53839	74329	27214	26938	8964
Timing cut	53832	73774	25313	26814	8964
Kink cut	53623	73759	25180	26743	8899
EM selection	11690	75	122	58	1471
Gamma cut	10438	59	85	39	30
Efficiency (%)	19.25	0.07	0.31	0.14	0.33
	e^-	μ^-	π^+	p	γ
Total	88458	87333	78305	77317	27357
Quality cut	87996	87307	78036	77173	27153
Timing cut	87962	77053	43292	76185	27152
Kink cut	86211	76775	39934	74995	26456
EM selection	31751	104	166	85	4933
Gamma cut	28871	86	120	55	121
Efficiency (%)	32.63	0.09	0.15	0.07	0.44

The event displays of the misidentified particle gun samples are shown in Appendix E.

The selection efficiencies and the misidentification rates for contained and escaping particles as a function of the particle momentum are shown in Figures 5.33 and 5.34. In every plots, error bars show only statistical errors. There is no event around 2.5 GeV/c region for gamma samples, thus the misidentification rate gets 0. In the actual data, gamma background with such a high momentum is quite rare and does not strongly affect the analysis.

Currently we are using the constant thresholds for the entire momentum region. However, once we will construct a momentum reconstruction method, we could further improve the efficiency by adopting the momentum-dependent thresholds. This will be a future task.

The selection efficiencies and the misidentification rates as a function of

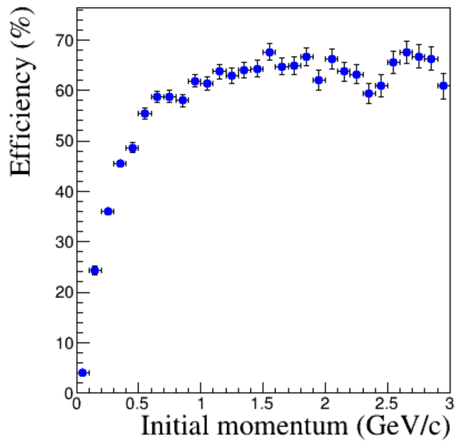

(a) Efficiency for e^-

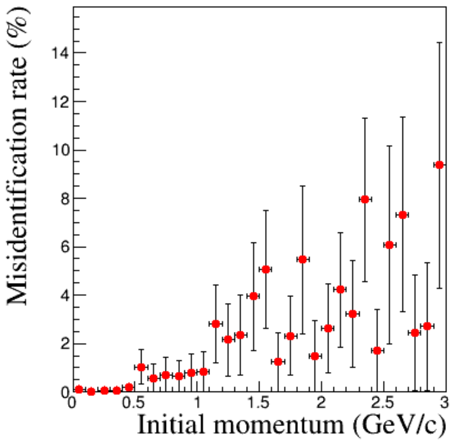

(b) Misidentification rate for μ^-

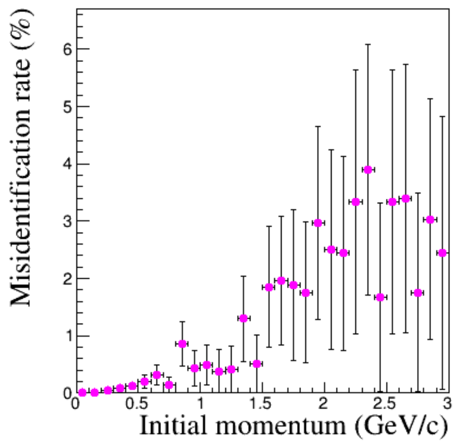

(c) Misidentification rate for π^+

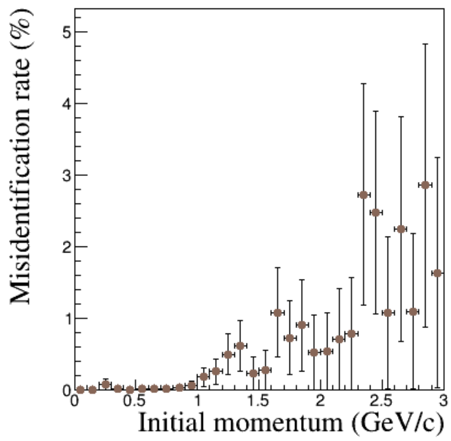

(d) Misidentification rate for p

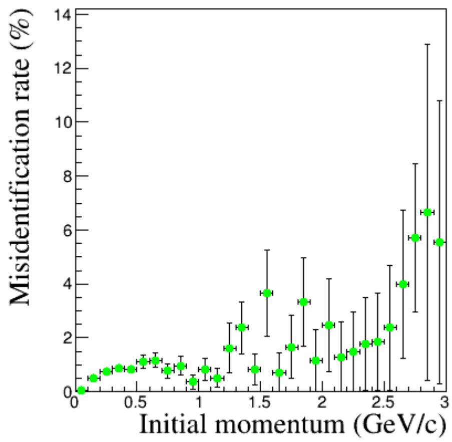

(e) Misidentification rate for γ

Figure 5.33: Selection efficiency and misidentification rate for contained particle gun samples as a function of momentum.

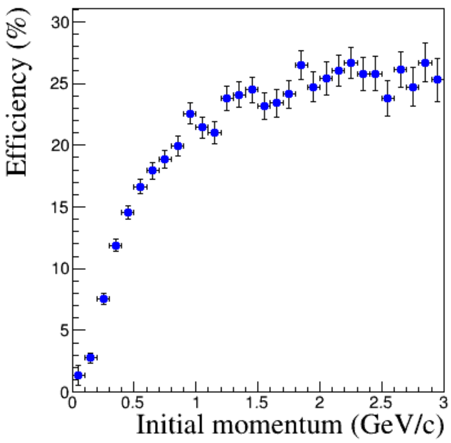

(a) Efficiency for e^-

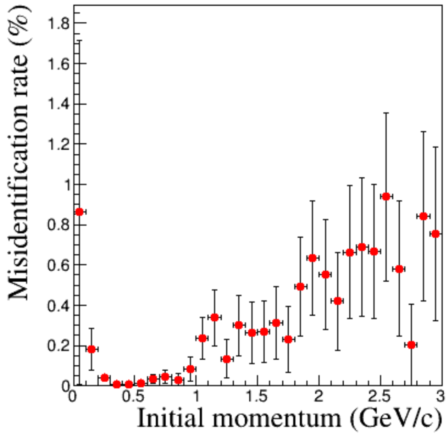

(b) Misidentification rate for μ^-

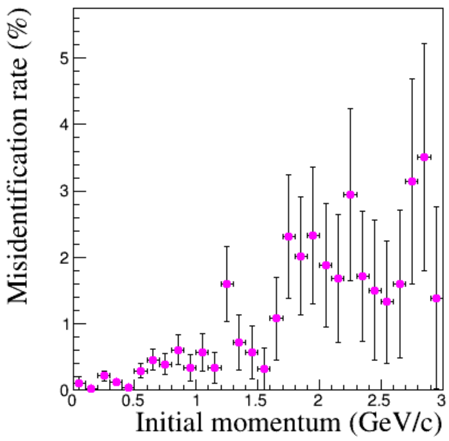

(c) Misidentification rate for π^+

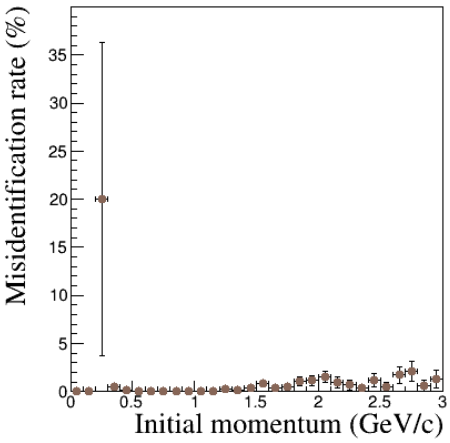

(d) Misidentification rate for p

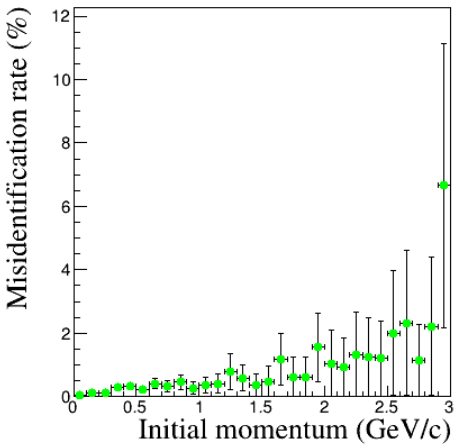

(e) Misidentification rate for γ

Figure 5.34: Selection efficiency and misidentification rate for escaping particle gun samples as a function of momentum.

the particle angle are shown in Appendix E.

Chapter 6

Selection with neutrino interaction MC samples

6.1 CC-ν_e interaction event selection flow

6.1.1 Neutrino interaction MC sample categorization

With using the PID discriminators constructed in Chapter 5, we select ν_e interaction events from the neutrino interaction MC samples. In the following study, both of the CC-ν_e and CC-ν_μ samples include their counterpart antineutrino interaction events ($\bar{\nu}_e$ and $\bar{\nu}_\mu$, respectively) for the simplicity. Neutrino interaction samples are divided into several categories based on the true information of the leading particle in the event. In CC-ν_e and CC-ν_μ events, the leading particle is defined as the primary lepton. For NC events, the highest momentum charged primary particle is regarded as the leading particle. Also, for γ events, the one of the gamma converted electron-positron pair with the higher momentum is assigned as the leading particle.

When the leading particle escapes from SuperFGD and enter the surrounding TPCs, it will be identified with TPC because TPC has greater capability of momentum reconstruction and particle identification. When it enters ECals, PID will also be performed by the combination with them. Thus, in the following study, we focus on the events whose leading particle is fully contained in SuperFGD.

In γ events, we have two primary particles starting from the conversion point. If both of them enter TPC, we can reject such event with the invariant mass cut. However, such kind of events are rare ($\sim 0.4\%$) for γ backgrounds in SuperFGD since converted electron-positron pairs are usually contained in SuperFGD due to its large volume. Thus, we take into account all of the γ backgrounds converted in the SuperFGD FV in the following selection study.

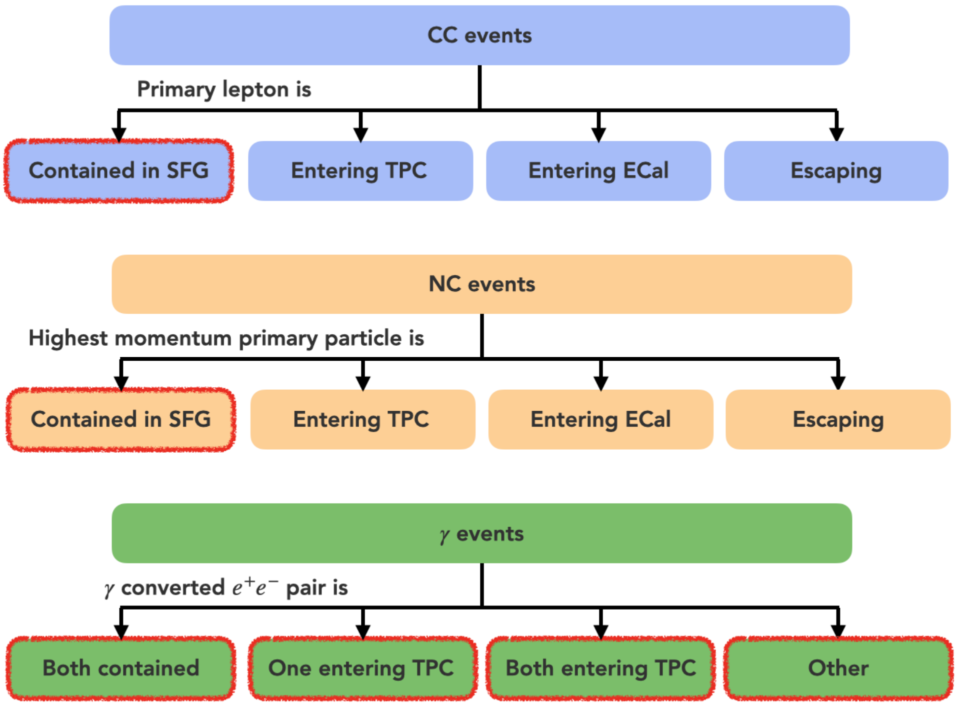

Figure 6.1: Classification of the leading particle for CC, NC, and γ events. The samples used in this study are marked with a red line.

The categorization of the neutrino interaction samples based on the leading particle is shown in Figure 6.1. The corresponding number of events in each category is summarized in Tables 6.1 and 6.2.

After requiring the leading particle is contained in SuperFGD in CC and NC samples, the fractions of CC-ν_e events to the total events are 1.4% and 1.1% for the basket flux sample and the magnet flux sample, respectively. Also, the fraction of the contained events for ν_e interactions in SuperFGD is approximately one third of the total ν_e events. The momentum and angular distributions of these categories for ν_e events are shown in Figure 6.2.

6.1.2 CC-ν_e interaction selection with SuperFGD

The CC-ν_e interaction event selection flow with SuperFGD is shown in Figure 6.3.

We first divide events into two groups based on the number of reconstructed primary tracks, which are defined as the tracks starting from the given vertex. We give a true neutrino interaction vertex for CC and NC event samples, and a true γ conversion point for γ events in this study. Then we

Table 6.1: Number of events in each category for the basket flux sample (1×10^{21} POT). These numbers shows only the SuperFGD FV events.

Sample category	CC-ν_e	CC-ν_μ	NC	Sample category	γ
Contained	1047	21039	27024	Both contained	16527
Enter TPC	956	100008	5994	One enters TPC	3798
Enter ECal	58	9073	601	Both enter TPC	1463
Other	930	22552	808	Other	1558
Total	2991	152672	34438	Total	23346

Table 6.2: Number of events in each category for the magnet flux sample (1×10^{20} POT). These numbers shows only the SuperFGD FV events.

Sample category	CC-ν_e	CC-ν_μ	NC	Sample category	γ
Contained	111	2073	2649	Both contained	3869
Enter TPC	81	10057	608	One enters TPC	740
Enter ECal	10	943	69	Both enter TPC	255
Other	88	2286	58	Other	298
Total	290	15359	3384	Total	5162

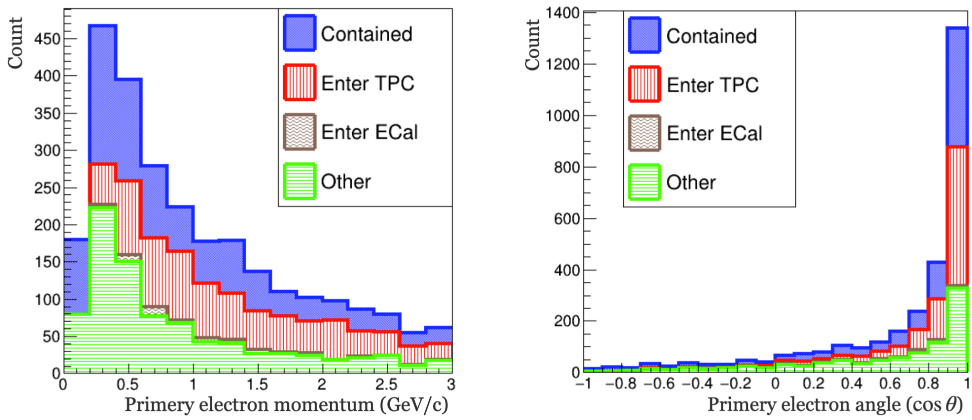

(a) True momentum distribution.

(b) True angular distribution.

Figure 6.2: The true momentum and angular distributions of the categorised ν_e events for the basket flux sample (1×10^{21} POT).

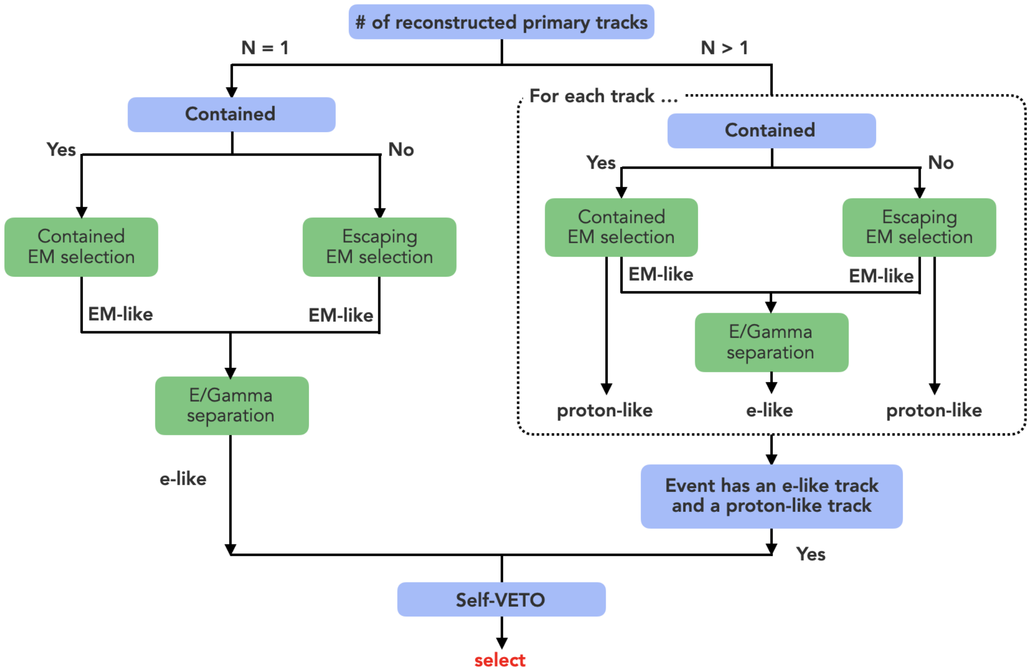

Figure 6.3: Selection flow for the CC-ν_e interaction events with SuperFGD.

apply the EM shower selection and the γ cut for each primary track to select electron-like track. When we have several reconstructed primary tracks, we require that the event has 1 or more proton-like track since the most CC-ν_e interaction give primary protons. Proton-like track is selected with:

$$\begin{aligned} &\text{Contain\_EM\_HIP} < -0.2 \text{ (for contained track)} \\ \text{or} \quad &\text{Escape\_EM\_HIP} < -0.2 \text{ (for escaping track)}. \end{aligned} \tag{6.1}$$

For selected events with above criteria, SuperFGD self-VETO is applied to further reject γ contamination. Events are rejected if there are more than one distant tracks which are not matched with any primary tracks since such an event mainly comes from the γ background. Figure 6.4 shows the number of not-matched distant tracks for events after all the above selection.

6.2 PID method optimization

The biggest difference between the neutrino interaction samples and particle gun samples is that we have several primary tracks from the same vertex in neutrino interactions. Thus, in neutrino interaction cases, track overlaps can affect the particle identification. In order to eliminate the effect of track

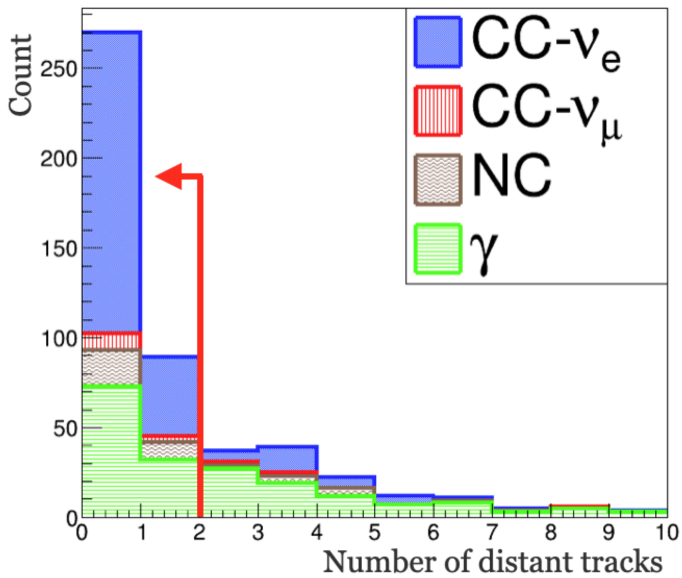

Figure 6.4: Number of not-matched distant tracks in SuperFGD after the ν_e event selection with the basket flux (1×10^{21} POT).

overlapping, we exclude the hits inside a 5 cm sphere around the vertex when calculating the variables used for the EM shower PID. The length of the primary track, which is not affected by overlapping, is however, calculated as the same as the previous one. After excluding hits around the vertex, we re-trained and tested the selection algorithms with particle gun samples. The results are shown in Table 6.3. The efficiency got slightly worse than the previous results in Table 5.1. The biggest difference comes from the quality cut, which requires at least 5 hits outside the 5 cm sphere around the vertex.

6.3 Final selection result

We applied the SuperFGD CC-ν_e event selection for the neutrino interaction samples after the correction of the PID method. For the basket flux sample, 359 events are selected out of 72456 events. The breakdown of the number of events is shown in Table 6.4. The selection efficiency for CC-ν_e events is 20.24%. The purity of the selected sample is 59.05%.

The momentum and angular distributions of the total and selected events for the basket flux sample are shown in Figure 6.5 and 6.6.

We further reduce γ backgrounds by applying VETO with other detectors. Since other detector reconstruction tools are not ready yet, we use the true information to simulate this VETO cut. If a γ event satisfies these conditions:

Table 6.3: Selection results with particle gun samples after excluding hits around the vertex.

	e^-	μ^-	π^+	p	γ
Contained	34243	12987	51013	50322	18286
Quality	33804	12563	44708	39281	16847
Timing	33777	2976	13243	38426	16846
Kink	32243	2714	10068	37328	16237
EM selection	19798	28	61	30	3712
Gamma cut	18194	25	49	20	98
Efficiency (%)	53.13	0.19	0.09	0.03	0.53
	e^-	μ^-	π^+	p	γ
Escaping	54215	74346	27292	26995	9071
Quality	49629	71386	24576	24383	7637
Timing	49622	70852	22876	24262	7637
Kink	49414	70837	22747	24194	7574
EM selection	11567	76	123	73	1490
Gamma cut	10287	54	92	51	29
Efficiency (%)	18.97	0.07	0.33	0.18	0.31
	e^-	μ^-	π^+	p	γ
Total	88458	87333	78305	77317	27357
Quality	83433	83949	69284	63664	24484
Timing	83399	73828	36119	62688	24483
Kink	81657	73551	32815	61522	23811
EM selection	31365	104	184	103	5202
Gamma cut	28481	79	141	71	127
Efficiency (%)	32.19	0.09	0.18	0.09	0.46

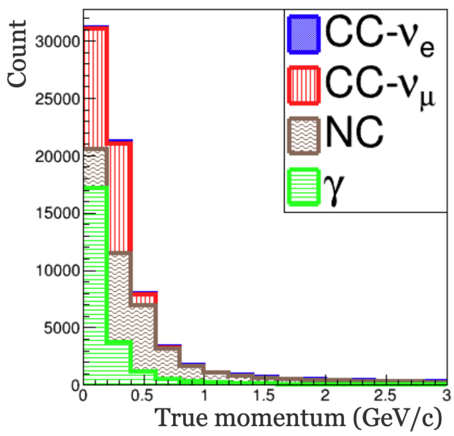

(a) Total events.

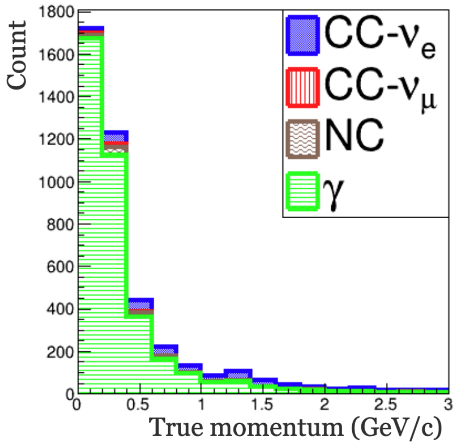

(b) After EM selection.

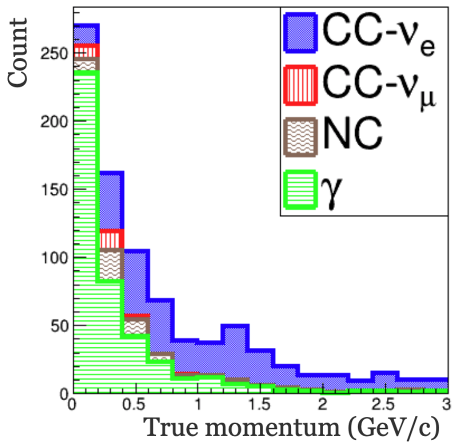

(c) After γ rejection.

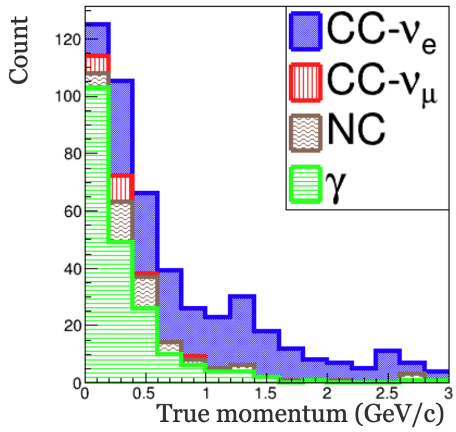

(d) After p track cut.

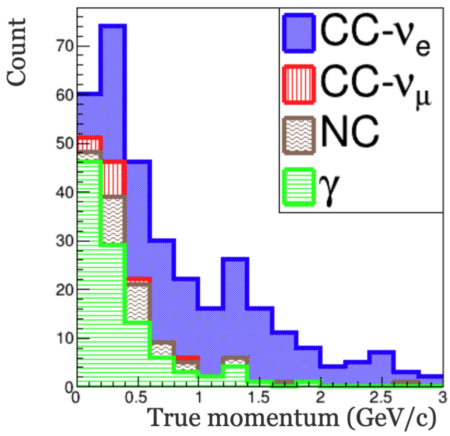

(e) After self-VETO.

Figure 6.5: The true momentum distribution of the leading particle at each selection step for the basket flux sample (1×10^{21} POT).

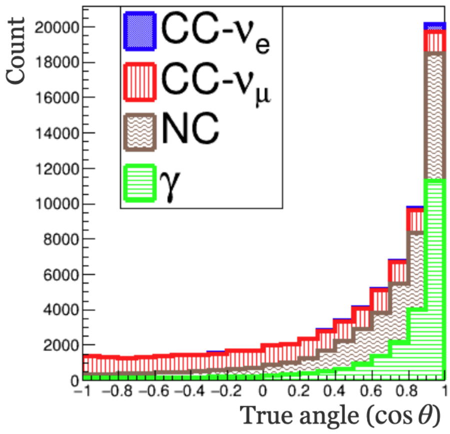

(a) Total events.

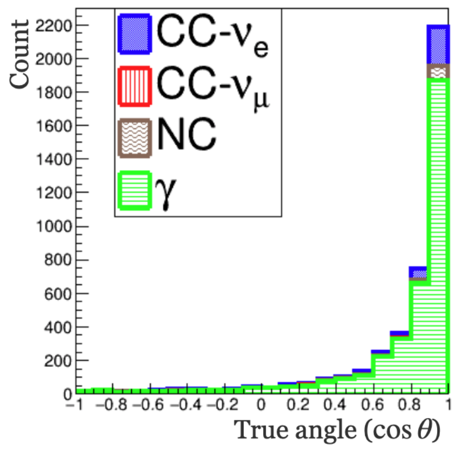

(b) After EM selection.

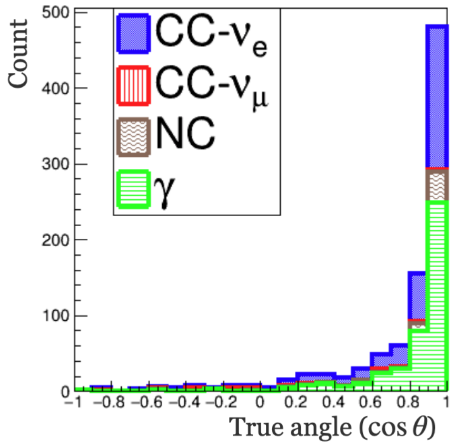

(c) After γ rejection.

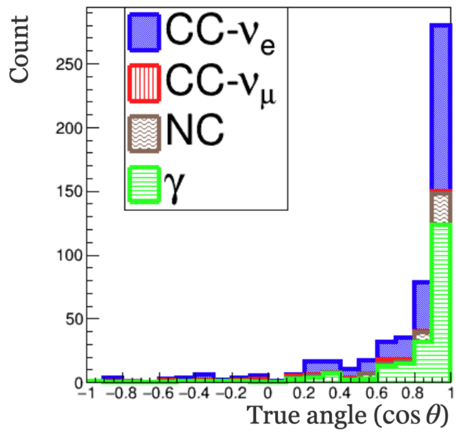

(d) After p track cut.

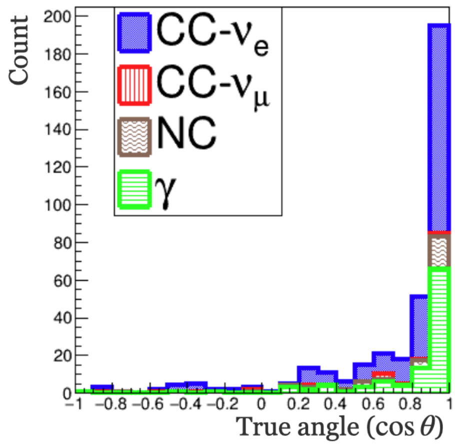

(e) After self-VETO.

Figure 6.6: The true angular distribution of the leading particle at each selection step for the basket flux sample (1×10^{21} POT).

Table 6.4: Selection result with the basket flux sample (1×10^{21} POT).

	ν_e	ν_μ	NC	γ	Total
Total	1047	21039	27024	23346	72456
$N_{\mathrm{prim}} = 1$	187	4752	19520	17263	41722
EM-like	89	0	68	3242	3399
γ cut	20	0	2	26	48
Self-VETO	16	0	1	10	27
$N_{\mathrm{prim}} > 1$	860	16287	7504	6083	30734
$N_{\mathrm{EM-like}} = 1$	356	28	63	407	854
$N_{\mathrm{proton-like}} > 0$	231	17	44	181	473
Self-VETO	196	12	29	95	332
Selected total	212	12	30	105	359
Efficiency (%)	20.2	0.05	0.11	0.45	
Fraction (%)	59.1	3.3	8.4	29.3	

Table 6.5: Selection result with the basket flux sample (1×10^{21} POT) after applying the other detector VETO.

	ν_e	ν_μ	NC	γ	Total
Total	1047	21039	27221	23346	72653
SuperFGD selection	212	12	30	105	359
Other detector VETO	212	12	30	24	278
Efficiency (%)	20.2	0.05	0.11	0.1	
Fraction (%)	76.3	4.3	11	8.6	

1. position of the original neutrino interaction vertex is inside the other detector including TOFs, TPCs, FGDs, and ECals;

2. there are 1 or more charged particles generated from the neutrino interaction,

it is rejected.

The momentum and angular distribution of the selected samples after requiring the other detector VETO are shown in Figure 6.7.

The final selection result is summarized in Table 6.5.

Figure 6.8 shows the final selection efficiency for ν_e events and misidentification rates for ν_μ and γ background events for the basket flux sample as a function of the momentum of the leading particle. The one as a function of the angle of the leading particle is also shown in Figure 6.9.

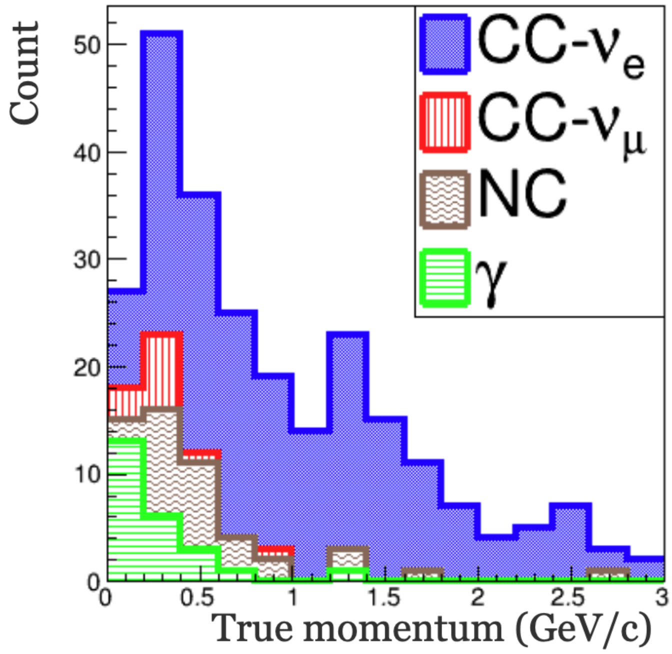

(a) Momentum distribution.

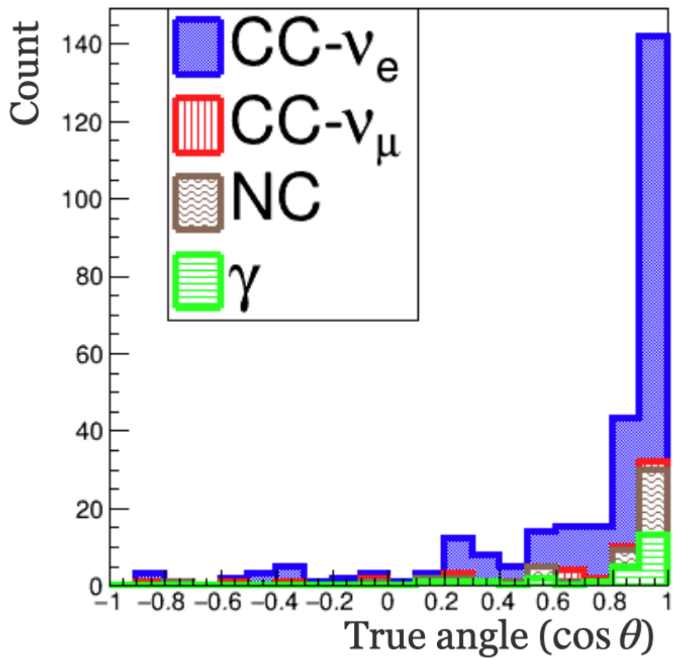

(b) Angular distribution.

Figure 6.7: The true (a) momentum and (b) angular distributions of the the leading particle after applying other detector VETO for the basket flux sample (1×10^{21} POT).

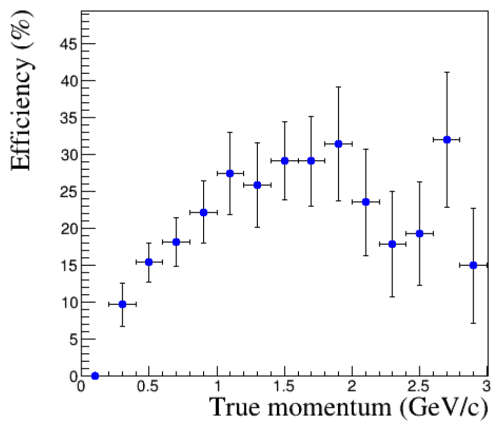

(a) Efficiency for ν_e samples.

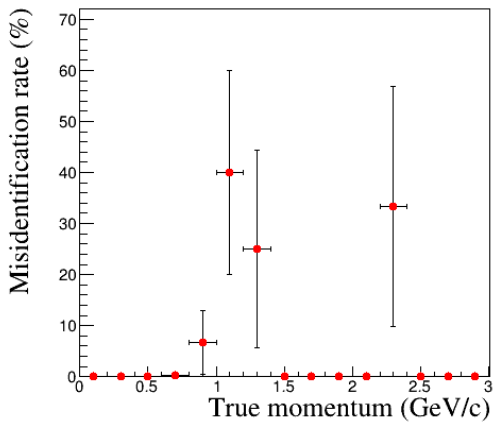

(b) Misidentification rate for ν_μ samples.

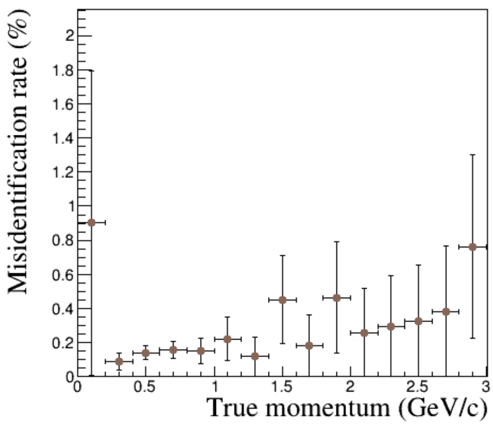

(c) Misidentification rate for NC samples.

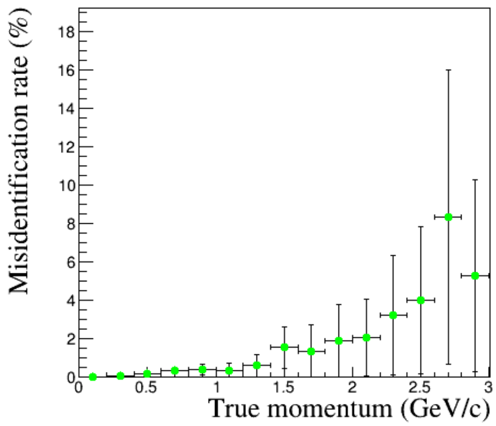

(d) Misidentification rate for γ

Figure 6.8: Selection efficiency and misidentification rate for each MC samples as a function of the true momentum of the leading particle with the basket flux sample (1×10^{21} POT).

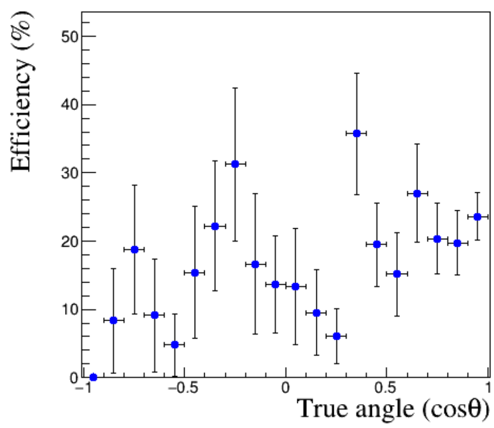

(a) Efficiency for ν_e samples.

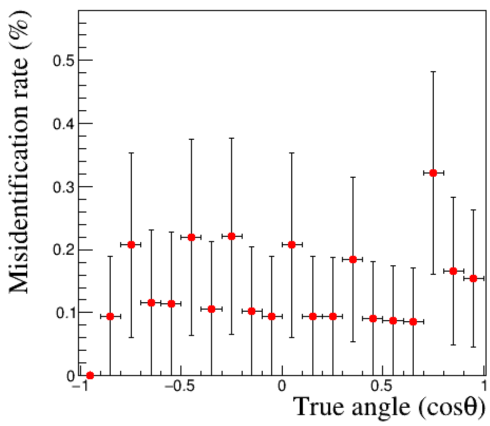

(b) Misidentification rate for ν_μ samples.

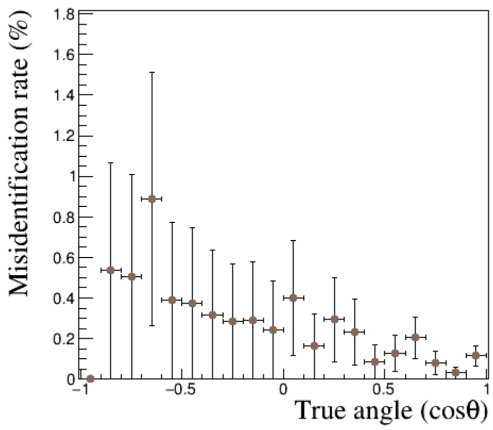

(c) Misidentification rate for NC samples.

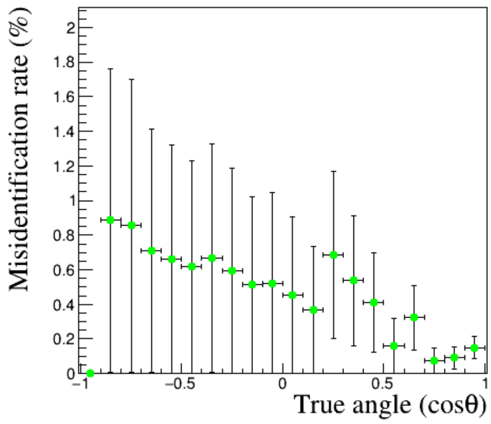

(d) Misidentification rate for γ

Figure 6.9: Selection efficiency and misidentification rate for each MC samples as a function of the true angle of the true leading particle with the basket flux sample (1×10^{21} POT).

Table 6.6: Selection result with the magnet flux sample (1×10^{20} POT).

	ν_e	ν_μ	NC	γ	Total
Total	111	5162	2073	2649	9995
$N_{\text{prim}} = 1$	24	1925	497	3862	6308
EM-like	15	3	0	496	514
γ cut	4	0	0	3	7
Self-VETO	3	0	0	1	4
Other-VETO	3	0	0	0	3
$N_{\text{prim}} > 1$	87	724	1576	1300	3687
$N_{\text{EM-like}} = 1$	27	7	2	54	90
$N_{\text{proton-like}} > 0$	19	4	1	19	43
Self-VETO	16	3	1	12	32
Other-VETO	16	3	1	6	26
Selected total	19	3	1	6	29
Efficiency (%)	17.11	0.11	0.04	0.11	
Fraction (%)	66	10	3	21	

We also applied the same selection to the magnet flux sample of 1×10^{20} POT. The selection result is shown in Table 6.6. The statistics of the sample is too small to give a conclusion with this result. However, since the magnet flux sample originally has about 2.2 times of γ events compared to the basket flux sample, their results make an agreement when the number of selected γ in the basket flux is multiplied by 2.2. When we correct the number of selected γ events in the basket flux, the purity of the signal decreases from 76.3% to 69%.

6.4 Discussion

6.4.1 Capability of the ν_e cross section measurement

In this section, we discuss the possibility of ν_e cross section measurement with SuperFGD based on the ν_e interaction selection results with MC samples. As discussed in Chapter 2, T2K has performed the ν_e cross section measurement only in a limited phase space ($p > 300$ MeV/c and $\theta < 45°$) [11]. This is because the low momentum $p < 300$ MeV/c and large scattering angle $\theta > 45°$ region is contaminated with a large γ background.

We have shown that SuperFGD has a capability of γ rejection because of its high granularity. Using only SuperFGD and the VETO of other detector, we achieved the 20.2% efficiency with the purity of about 70% in the full phase space. Although the signal efficiency is a few percent lower than the current ND280 measurement, the purity is improved from the performance of current ND280 (54%). This is of great importance especially in the low momentum region ($p < 300$ MeV/c) where we have not been able to measure the ν_e cross section directly. From the obtained result shown in Figure 6.7, we can expect to bring down this momentum threshold to the level of 200 MeV/c with using SuperFGD. Since the selection threshold for electrons produced by ν_e interactions is 100 MeV/c at SK, it is important to directly measure the ν_e cross section of that momentum range. One of the reasons which allow us to reduce the background contamination at the low momentum region is that we can use the information around the conversion point of γ backgrounds in SuperFGD. This γ cut is applicable not only to SuperFGD-contained particles but also to TPC-entering particles.

Furthermore, SuperFGD shows the good selection efficiency not only for forward going tracks but also for tracks with large scattering angles. This is also critical for the T2K oscillation analysis because SK has a full polar acceptance while the current ND280 has a limited tracking efficiencies for the large angle region with regard to the beam direction. From the result of this study, we expect that SuperFGD has the full angle acceptance for electrons from ν_e interactions.

In the upcoming T2K-II phase, we are planning to collect total data of 10×10^{21} POT. When we simply normalize the previous selection result to this POT number, we could expect 2120 ν_e events selected only with SuperFGD. With the correction to the γ events in the basket flux sample, the expected number of total ν_e candidates is 2924, which corresponds to the statistical error of $\sqrt{2924}/2120 \simeq 2.6\%$. In the low momentum bin of [0.2,0.4] GeV/c, the expected number of total and signal events are 546 and 280, respectively. This indicates that we will be able to measure the ν_e cross section at [0.2,0.4] GeV/c with a statistical error of $\sqrt{546}/280 \simeq 8.3\%$.

From these point of view, we conclude that SuperFGD has a good capability of ν_e cross section measurement. We also expect to measure the ν_e cross section at low momentum and large scattering angle region, where no direct measurements have been performed so far.

6.4.2 Future tasks

There are several remaining tasks to be done before starting to take data with upgraded near detectors.

Selection algorithms for the RHC mode

In this thesis, we developed selection algorithms mainly for electron neutrinos in FHC. For antineutrinos in RHC, we have to develop different selection algorithms since they have different kind of particles in the final state. While CCQE interactions of neutrinos have protons in the final state, that of antineutrinos have neutrons which have no charge and cannot be directly detected with the detector. Also, the contamination of the neutrinos will be more crucial for antineutrino cross section measurements in RHC than that of the antineutrinos in FHC. These differences will be taken into account when developing new algorithms for the RHC mode.

EM shower energy reconstruction with SuperFGD

In the current ND280 analysis, we mainly use TPCs to reconstruct the momentum of particles. However, since one third of the ν_e events that interact in the SuperFGD FV are contained in SuperFGD, we have to develop a method to reconstruct the EM shower energy only with SuperFGD. This is important for the precision measurement of the ν_e cross section.

Vertex reconstruction

In this thesis, the true position of the vertex is given for the event selection study. In EM shower events, the reconstruction of the vertex is not trivial compared to the ν_μ interaction events. Thus, this will be a very important future task to develop a vertex reconstruction tool for upgrade near detector setup.

Combined analysis with other sub-detectors

Since other detector reconstruction tools are not ready at the moment, we performed the selection study only with SuperFGD in this thesis. The development of the all sub-detector combined reconstruction and selection algorithm will be a important future task.

Chapter 7

Summary

The T2K (Tokai-to-Kamioka) experiment is a long baseline neutrino oscillation experiment in Japan. We are measuring neutrino oscillations through the detection of electron neutrinos which is originally produced as muon neutrinos at the Japan Proton Accelerator Research Complex (J-PARC) by the Super-Kamiokande detector. We aim to observe the CP violation in lepton sector for the first time in the world. Until now, T2K has rejected the CP conservation in neutrino oscillations with more than 95% confidence level. The uncertainty on the ν_e cross section is one of the largest systematic errors in the current oscillation analysis.

In order to observe the CP violation with higher precision, T2K is proposing to upgrade the near detectors in 2022 and introduce a new tracking detector SuperFGD (Super Fine Grained Detector). In this thesis, we developed selection algorithms with SuperFGD for the interactions of the intrinsic ν_e components in the neutrino beam and evaluated them with the Monte Carlo samples. We achieved the ν_e selection efficiency of 20% with the signal purity over 70% for the ν_e events whose out-coming electron is contained in SuperFGD. The results show the capability of ν_e cross section measurement with SuperFGD, especially in low momentum ($p < 300$ MeV/c) and large scattering angle ($\theta > 45°$) region where no prior direct measurement has been performed so far.

Acknowledgment

First of all, I would like to express my special thanks to my supervisor, Prof. Hiroaki Aihara for giving me such an opportunity to conduct my research activity. I also would like to thank Prof. Masashi Yokoyama for his support during my master's course. He gave me a lot of advice which always helped me to carry my research toward the good direction. I want to express my special gratitude to the members of the Aihara-Yokoyama Laboratory in the University of Tokyo, Onuki-san, Nakagiri-san, Iwamoto-san, Matsushita-san, Kikutani-kun, Ogawa-san, Yoshimi, and Kono-san. I received a lot of advice and support which are related not only with physics but also with the daily lives in the laboratory.

I appreciate the support and feedback from the members of the software and reconstruction group in T2K, Davide Sgalaberna, Clark McGrew, Mathieu Guigue, Claudio Giganti, and Mahesh Jakkapu. It was always helpful to discuss with them about the reconstruction and analysis. I could not have done this work without their kind support.

I also want to thank members in the T2K collaboration, Ichikawa-san, Minamino-san, Matsubara-san, Kikawa-san, Ogawa-san, Yasutome-san, Giorgio Pintaudi, Takuji Arihara, Takuya Kobata, Takashi Honjo, and Katayama Yuna.

Finally I would like to show my special appreciation to my family for all the kind support they gave me.

Appendix A

Neutrino interactions

In this appendix, we briefly review the several types of neutrino-nucleus interactions. Figure A.1 shows the diagrams of various neutrino interaction modes with a nucleus.

A.1 Quasi-elastic scattering

Quasi-elastic (QE) scattering is the two-body process between a neutrino and a nucleus. This is the main target neutrino interaction mode in the T2K experiment. It produces a charged lepton and a nucleus in the final state:

$$\nu_l + n \to l^- + p \tag{A.1}$$

$$\bar{\nu}_l + p \to l^+ + n. \tag{A.2}$$

By assuming that a nucleon is at rest, the initial neutrino energy is reconstructed only with the lepton kinematics as

$$E_\nu = \frac{2m_n E_l - m_l^2 + (m_p^2 - m_n^2)}{2(m_n - E_l + p_l \cos\theta)}, \tag{A.3}$$

where E_l, p_l, and m_l are the energy, momentum, and mass of the out-coming lepton. m_p and m_n are the mass of the proton and neutron, respectively. θ is the scattering angle of the lepton track with regard to the incoming neutrino direction.

The cross section of quasi elastic scattering process can be written as [33]:

$$\frac{d\sigma}{dQ^2}\begin{pmatrix}\nu n \to l^- p \\ \bar{\nu} p \to l^+ n\end{pmatrix} = \frac{M^2 G_F^2 \cos^2\theta_c}{8\pi E_\nu^2}\left(A(Q^2) \pm B(Q^2)\frac{s-u}{M^2} + C(Q^2)\frac{(s-u)^2}{M^4}\right), \tag{A.4}$$

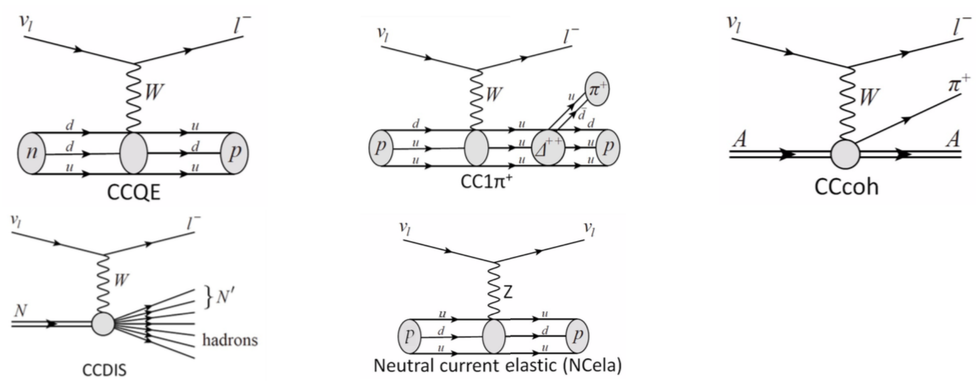

Figure A.1: The diagrams of various neutrino-nucleus interaction modes. Captions CCQE, CCcoh, and CCDIS stand for CC quasi-elastic scattering, CC coherent π^+ production, and CC deep inelastic scattering, respectively. The diagram of CC1π^+ corresponds to the resonance scattering.

where M is the nucleon mass, G_F is the Fermi coupling constant, θ_c is the Cabbibo angle, and s, u are the Mandelstam kinematics variables. Q^2 is the four-momentum transfer from the lepton to the hadron. The functions $A(Q^2)$,$B(Q^2)$, and $C(Q^2)$ depend on the nucleon form factors as:

$$
\begin{aligned}
A(Q^2) = \frac{m_l^2 + Q^2}{M^2} \Big[& (1+\tau)|F_A|^2 - (1-\tau)|F_V^1|^2 \\
& + \tau(1-\tau)|\xi F_V^2|^2 + 4\tau \mathrm{Re} F_V^{1*} \xi F_V^2 - 4\tau(1+\tau)|F_A^3|^2 \\
& - \frac{m_l^2}{4M^2} \left(|F_V^1 + \xi F_V^2|^2 + |F_A + 2F_p|^2 \right. \\
& \left. -4(1+\tau)\left(|F_V^3| + |F_P|^2\right)\right) \Big] \qquad \text{(A.5)} \\
B(Q^2) = {} & 4\tau \mathrm{Re} F_A^* (F_V^1 + \xi F_V^2) \\
& - \frac{m^2}{M^2} \mathrm{Re}\left[\left(F_V^1 - \tau\xi F_V^2\right)^* F_V^3 - (F_A - 2\tau F_P)^* F_A^3 \right] \qquad \text{(A.6)} \\
C(Q^2) = {} & \frac{1}{4}\left(|F_A|^2 + |F_V^1|^2 + \tau|\xi F_V^2|^2 + 4\tau|F_A^3|^2 \right), \qquad \text{(A.7)}
\end{aligned}
$$

where $\tau = Q^2/4M^2$ and $\xi = \mu_p - \mu_n = 3.71$ is the difference between the anomalous magnetic momentum of the proton and the neutron. F_V^1 and F_V^2 are the vector and F_A and F_P are the axial form factors of the first class currents. F_V^3 and F_A^3 are form factors associated with the second class current.

A.2 Resonance scattering

At the neutrino energy region around a few GeV, the most dominant interaction process is the resonance scattering (RES). In the resonance scattering process, a nucleon struck by a neutrino is able to be a baryon resonant state [34]. It decays into a final state with a nucleon and a single pion, kaon, η, or γ.

For example, the resonant pion production process can be written as

$$\nu_l + N \to N^* + l^- \to N' + l^- + \pi \tag{A.8}$$

where N, N' are the nucleon and N^* is the resonant state. The resonant pion production can occur via neutral-current (NC) as well.

A.3 Deep inelastic scattering

At the neutrino energy region around 10 GeV, deep inelastic scattering (DIS) process dominantly contributes. In DIS process, neutrino directly interact with quarks inside a nucleon [35]. It breaks the nucleon and produces a jet of hadrons as written by

$$\nu_l + N \to l + N' + \text{hadrons}. \tag{A.9}$$

A.4 Coherent pion production

In coherent pion production process, neutrino interacts with entire nucleus and produces a pion without changing the quantum state of nucleus [36].

$$\nu_l + N \to l + N' + \pi. \tag{A.10}$$

This interaction occurs with low energy transfer. The cross section of the coherent pion process is a few percent of CCQE and it is not a dominant process.

A.5 Correction to the interaction models

Neutrino interaction models introduced in the previous sections are well describing the experimental results which are conducted with light nucleus target such as hydrogen and deuteron [37]. However, the detectors used in the T2K experiment are mainly using ^{12}C or ^{16}O nucleus as a target. In such cases, one have to take into account the contribution of the other effects. For instance, the initial momentum of the nucleon inside a nucleus can affect the neutrino interaction, which is referred to as the initial state effect. The structure of a nucleus is too complicated to exactly describe. Thus some models have been proposed in order to approximate the initial state effect [38, 39, 40]. In ^{12}C or ^{16}O nucleus, the target nucleon is not free but bound in nucleus. Thus we need to take into account the multi-nucleon effect such as 2-particle 2-hole process (2p2h) [41, 42]. The final state particles such as pions and nucleons produced at a neutrino interaction process can reinteract while transported inside the nuclear medium [25]. This is called as a final state interaction (FSI). It means that observed particles are not always the same as the ones generated by the neutrino interaction.

When reconstructing the neutrino energy, T2K uses the kinematics of the selected out-going lepton assuming that the interaction is quasi-elastic. However, nuclear effects such as those discussed above can bias this energy reconstruction. These effects are not fully understood from the experimental results so far and give systematic uncertainties on neutrino oscillation analysis. It is important to reduce such uncertainties through the precise measurement of neutrino cross sections.

Appendix B

Simulation process

In the T2K ND280 anlaysis, the MC simulation follows these processes: neutrino interaction generation, Geant4 simulation, detector response simulation, sub-detector reconstruction, and physics analysis such as cross section measurements. In this appendix we will describe the simulation processes for MC data.

B.1 Neutrino interaction generation

We use an external program library NEUT [43, 25] for simulating the neutrino interactions. This library is built for simulating the neutrino interactions with nucleon and nucleus. It is originally designed to simulate neutrino interaction only on hydrogen and oxygen targets since it was developed to study the atmospheric neutrino and nucleon decay in a water cherenkov detector. Now various nuclei targets including carbon, argon, and iron are available.

Using this NEUT library, we simulate neutrino interactions at ND280. It takes the neutrino type, target, neutrino energy, and flux as inputs, and return the kinematics of out-going particles as the output. Thus, given a neutrino beam flux and detector geometries, NEUT can simulate the event rate and interactions of neutrinos at ND280. The information of out-going particles is passed to the next Geant4 simulation step.

B.2 Geant4 simulation

Geant4 is a toolkit for simulating the passage of particles through matter [44]. In this step, given the kinematics of the initial particles and detector geometries, we simulate the interaction process of each particle along with its passage. At each interaction process, referred to as a hit, the position,

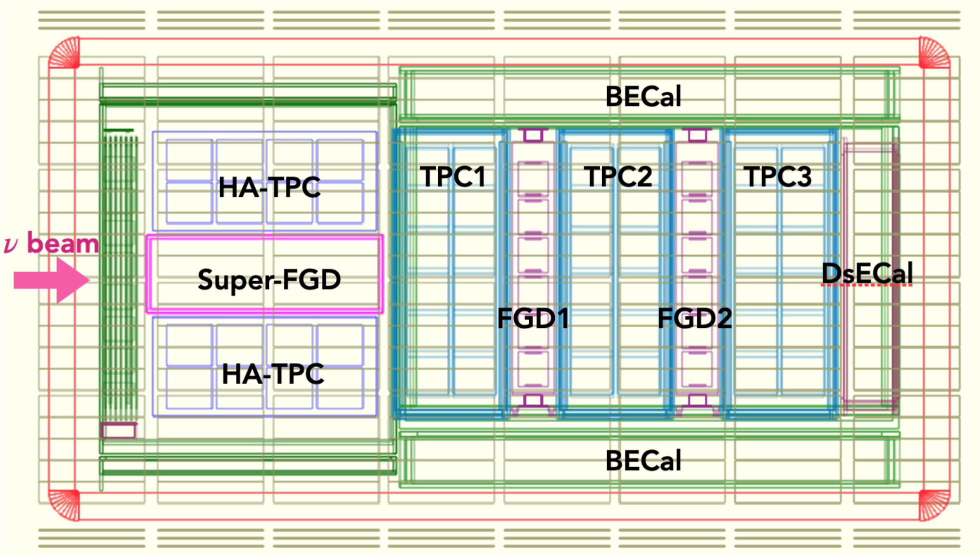

Figure B.1: Input detector geometries for Geant4 simulation (side view).

Table B.1: SuperFGD geometry values.

Variable	Value (mm)
Cube length	10.27
Hole position	3.0
Hole radius	0.75
Fiber radius	0.50
Coating thickness	0.1

timing, and energy deposition are computed. These kinds of information are passed to the next electronics simulation step.

Figure B.1 shows the input detector geometries. Tracker detector fields including SuperFGD, FGDs, TPCs, and Downstream ECal are referred to as a basket. The basket is surrounded by P0D ECals, Barrel ECals, and the magnet. All of these detector configurations are stored in the Geant4 simulation package.

SuperFGD consists of $192 \times 56 \times 184$ scintillator cubes. Each cube has though holes in three directions for WLS fibers. Figure B.2 shows the input geometries for scintillator cubes and WLS fibers. Corresponding values are listed in Table B.1.

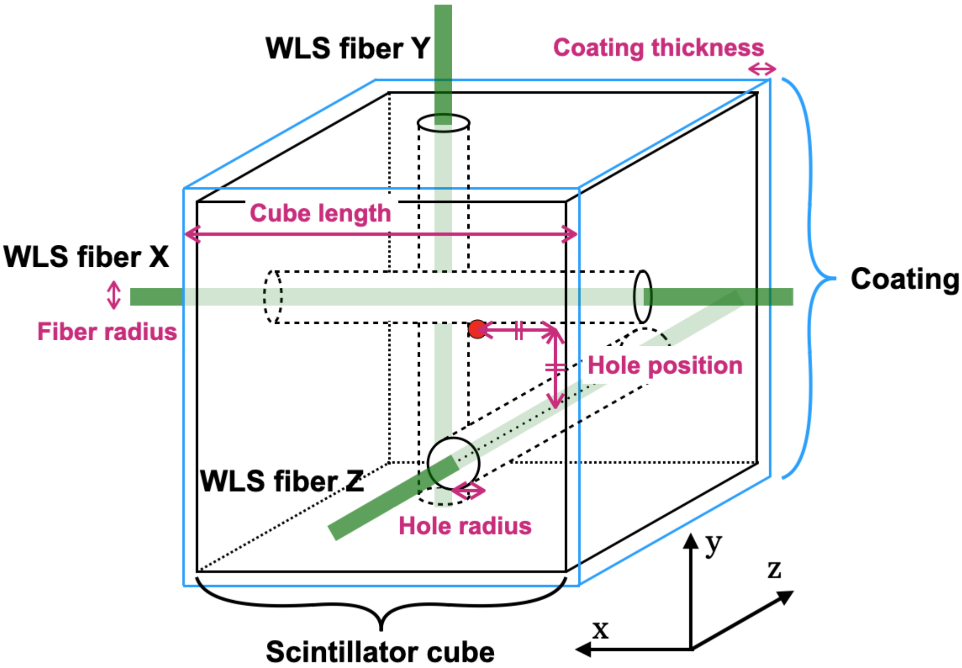

Figure B.2: Input geometries for scintillator cube. Values of the parameters used in the simulation are summarized in Table B.1.

B.3 Detector response simulation

In this step, we simulate the response of detectors and electronics in order to convert the Geant4 simulation outputs into observable electronic signals. The simulation process is different for each sub-detector since they have different configurations.

The simulation flow for SuperFGD part is shown in Figure B.3.

Given a hit timing and an energy deposit in each scintillator cube, first we compute the number of photo-electrons (p.e.) collected by fibers that are passing through the cube. This process includes the light attenuation within a scintillator cube, probability of the light entering a WLS fiber and the trapping efficiency of light inside a WLS fiber. Since it will be computationally too expensive if we compute all of these effects, this time we simply converted the energy deposit into the number of photo-electrons (p.e.) with the equation:

$$\text{Number of photo-electron (p.e.)} = 310 \times \text{Deposit energy (MeV)}. \qquad \text{(B.1)}$$

This conversion constant is decided based on the beam test result [31]. This process also involves the light leakage to neighbor cubes which is referred to

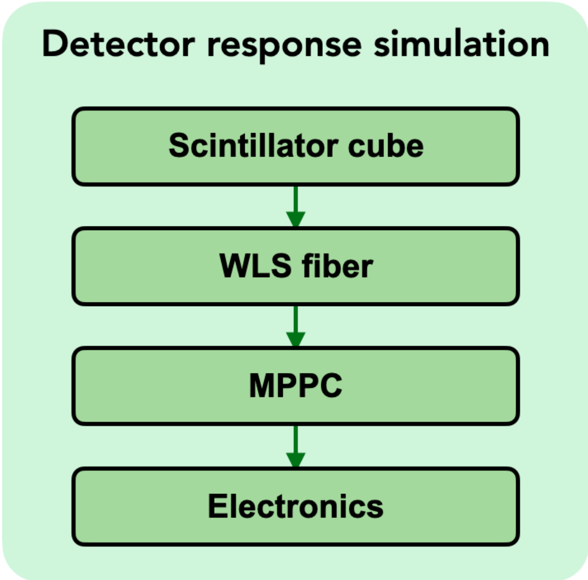

Figure B.3: The detector response simulation flow for SuperFGD.

as a crosstalk. This crosstalk rate is set to be approximately 6% in total (1% for each cube surface) from a beam test result.

As a second step, we compute the attenuation of the light while traveling through fibers according to the distance between the cube and the MPPC. For the photons generated in a cube whose distance from the MPPC is d, the attenuation A is calculated with the equation [16]:

$$A = LY_0 \left(\alpha e^{\frac{-d}{L_S}} + (1 - \alpha) e^{\frac{-d}{L_L}} \right) \tag{B.2}$$

where LY_0 is unattenuated light yield, α is a weighting factor, and L_S and L_L are short and long attenuation constants, respectively. Input variables used in this detector response simulation are listed in Table B.2.

As a third step, we simulated the response of MPPCs. Photons collected along a fiber are detected with the MPPC at one side of the fiber edge. In each MPPC channel, photons are converted into pixel hits. We assume a Gaussian distribution to determine which pixel is struck by a photon. Then we simulate the dark noise hit, pixel cross-talk and after-pulse for each pixel. Input variables used in this MPPC response simulation are listed in Table B.3.

Finally, we simulate the response of the read-out electronics. Here we assume a CITIROC module [30] as a read-out electronics. From the hit timing and charge information of all the pixel, we construct a pulse and compute the hit timing and the charge in each channel.

Table B.2: Input values for the scintillator cube response and the fiber attenuation simulation in SuperFGD.

Variable	Value
Generated photons per MeV	310
Crosstalk rate along X axis	0.0097
Crosstalk rate along Y axis	0.0097
Crosstalk rate along Z axis	0.0097
WLS fiber light velocity	160 mm/ns
WLS fiber long fraction (α)	0.77
WLS fiber long component (L_L)	4634 mm
WLS fiber short component (L_S)	332 mm

Table B.3: Input values for MPPC and electronics response simulation in SuperFGD.

Variable	Value
Dark noise rate	3000 Hz
Gate duration	15000 ns
Gain	7.1×10^5
Pixel crosstalk probability	0.005
After pulse probability	0.005
Photon detection efficiency (PDE)	0.25

Appendix C

Reconstruction process

In this appendix, we will introduce the detail reconstruction processes for SuperFGD.

C.1 SuperFGD reconstruction

The SuperFGD reconstruction follows the steps shown in Figure C.1.

Time slice

In order to collect hits from one neutrino interaction, we break the MPPC hits into groups separated by an 100 ns gap. First we sort all the MPPC hits according to the timing order and check the timing difference from the first to last hit. Then, if there is a gap longer than 100 ns, we break the hits into separate clusters there. This criteria is just a tentative value and will be tuned with the actual beam property. In actual data, the beam has an eight-bunch structure in each spill which has 580 ns spacing between every bunches. We accept the hits if they are within 4σ (using $\sigma = 15$ ns) from the centeral timing of one of the bunches.

3D hit building

Detector response simulation gives us 2-dimensional (2D) hit projections for three orthogonal directions. We convert this group of 2D hits into 3D hits by assigning every possible combinations of fiber cross point as hits. Then charge is assigned to each cube based on the event topology by using a maximum

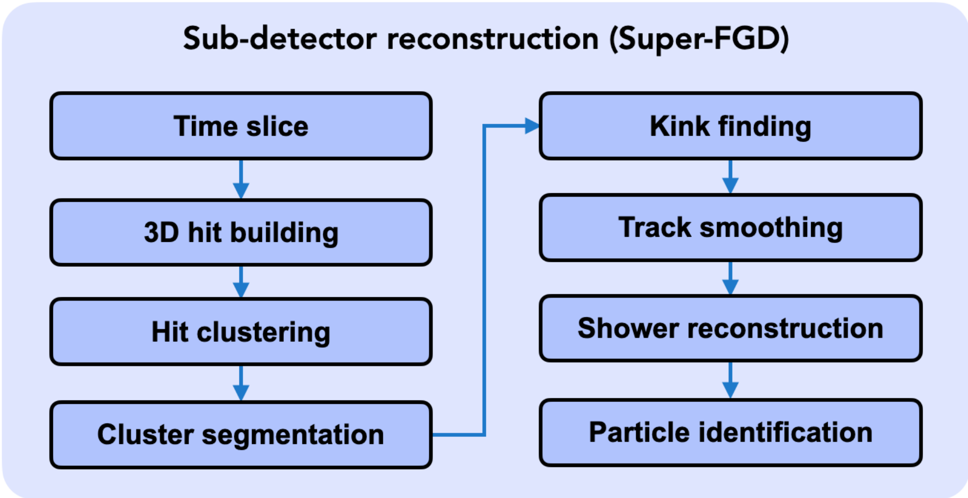

Figure C.1: SuperFGD reconstruction flow

likelihood fit. The log-likelihood for each fiber is defined as:

$$\ln \mathcal{L}^{\text{cube}} = \sum_{i=1}^{3} \ln \mathcal{L}_i^{\text{fiber}} \tag{C.1}$$

$$\ln \mathcal{L}_i^{\text{fiber}} = \frac{(\sum_j^{\text{cubes}} Q_{ij} - Q_i^{\text{obs}})^2}{Q_i^{\text{obs}}}, \tag{C.2}$$

where Q_{ij} is the expected charge after attenuation in the j-th cube on the i-th fiber and Q_i^{obs} is the observed charge for the i-th fiber. We decide a set of cube charges that maximizes this likelihood. Besides, we set a constraint that the sum of the charge from all cubes on a fiber, which is corrected with fiber attenuation, should be equal to the measured MPPC charge. The deposited charge in each cube is also constrained to be positive. In order to break degeneracies, we also require that it maximize the entropy defined as

$$\epsilon = -\sum_{i}^{\text{all cubes}} Q_i \ln Q_i. \tag{C.3}$$

This requirement slightly prefers that all the cubes have the same charge. Without this constraint, we can have cases where there are cubes giving a degenerated likelihood. Under all of these constraints, the set of cube charges is calculated so that it maximize the likelihood. This procedure is referred to as a “charge sharing”.

There can be fake hits coming from the ambiguity when matching the three 2D views into 3D. When matching the coordinates of the fibers that

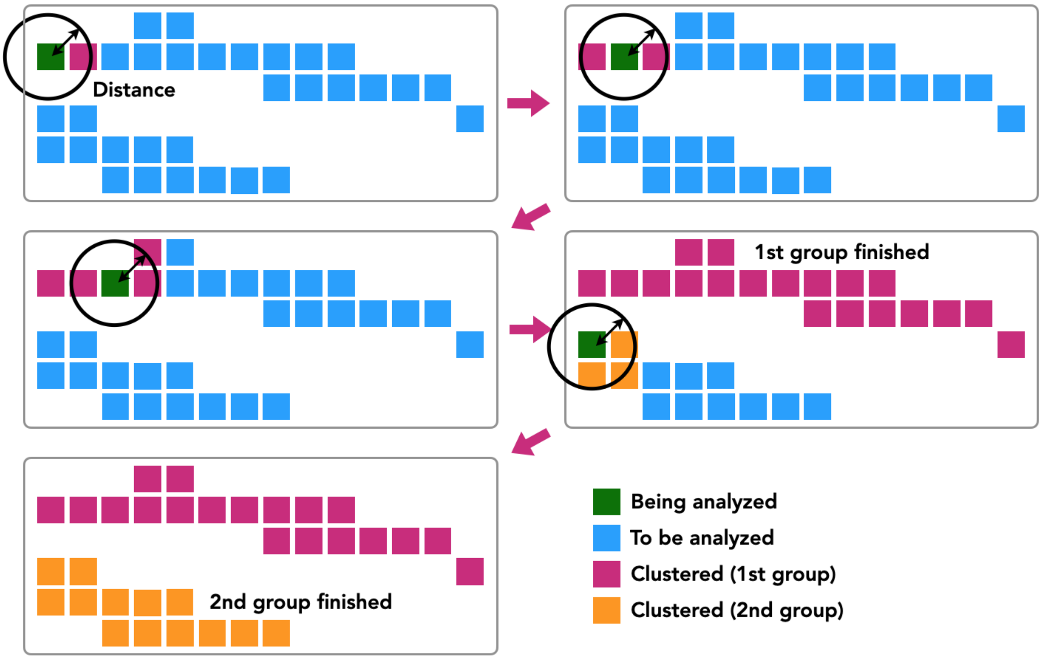

Figure C.2: DBSCAN flow

recorded energy deposition, hits may appear where no true signal exists which are called ghost hits [45]. They tend to be reconstructed as low charge hits in this charge sharing step.

In addition to the charge sharing, we also reconstruct the timing information for each cube from the three readout MPPC hit timings. After correcting the delay in each fiber, we check the three MPPC hit timings are within a time window of 2.5 ns. If they are all in the same time window, we take the average of the three MPPC hit timings as a cube hit timing. However, if one of the MPPC hits catch a photon from another cube along the same fiber, it can have a hit timing out of the window. In such case, the cube hit timing is set to the average of the rest MPPC hits that are in coincidence. If none of the MPPC hits are in coincidence, we take the timing of the latest hit.

Hit clustering

Hit clustering is done by using DBSCAN method [46]. Starting from an arbitrary hit, we connect neighboring hits within 16 mm radius and iterate over connected hits until we can find no more neighboring hits. Then, starting from another unconnected hit, we repeat the same process for all the left hits. Figure C.2 shows the DBSCAN clustering steps.

At this point, all the hits are stored as the cluster objects.

Cluster segmentation

For the cluster segmentation, we use Prim's algorithm to make a minimum spanning tree (MST) [47]. The MST problem of a connected graph is to find a spanning tree with minimum total edge weight. In this case, each hit is taken as a separate vertex and the connections between every two hits are taken as edges. Every hits in a cluster are connected via edges in the initial state, but only the edges in a MST will be kept in the final state. The weight on each edge is decided based on the geometrical distance between two hits and the charge factor. Charge factor is defined as

$$f = \exp[-(Q_1 + Q_2)] \tag{C.4}$$

which makes the edge weight between the lower charge cubes smaller.

An illustration of the MST construction is shown in Figure C.3. The construction of the MST is repeated twice; the first round is to search for the deepest hit in a cluster and the second round is to construct a final minimum spanning tree. We first choose an arbitrary hit in a cluster and connect the nearest neighbor hit. When a hit has several edges, we choose the one with the smallest weight as a nearest neighbor. This is repeated until reaching the last hit that has no more neighbor hit. The last hit should be the start or end point of the track. Then going back to the junction hit that has two or more edges, we repeat connecting rest of the hits in the same way. After connecting all the hits in a cluster, we chose a farthest hit from the starting hit as the deepest hit. Then we repeat the same thing again, this time starting from the deepest hit. This two-step MST construction process allows us to make sure that the starting point is at one end of the track. After constructing a minimum spanning tree, we break the cluster at every junction hits that has two or more edges. Every hits are sorted according to the order in the MST. Thus the first and the last hits in each cluster correspond to the hits at the branching point in the tree.

Kink finding

A kink is defined as the point where a cluster is bent. This can be a candidate of a neutrino interaction point where two visible tracks are coming from or a scattering point of hadrons. A kink is searched by scanning over every seven consecutive hits in a cluster and finding the place where the middle hit is furthest from the line between the two end hits. An illustration of the kink finding method is shown in Figure C.4. If the distance is larger than a

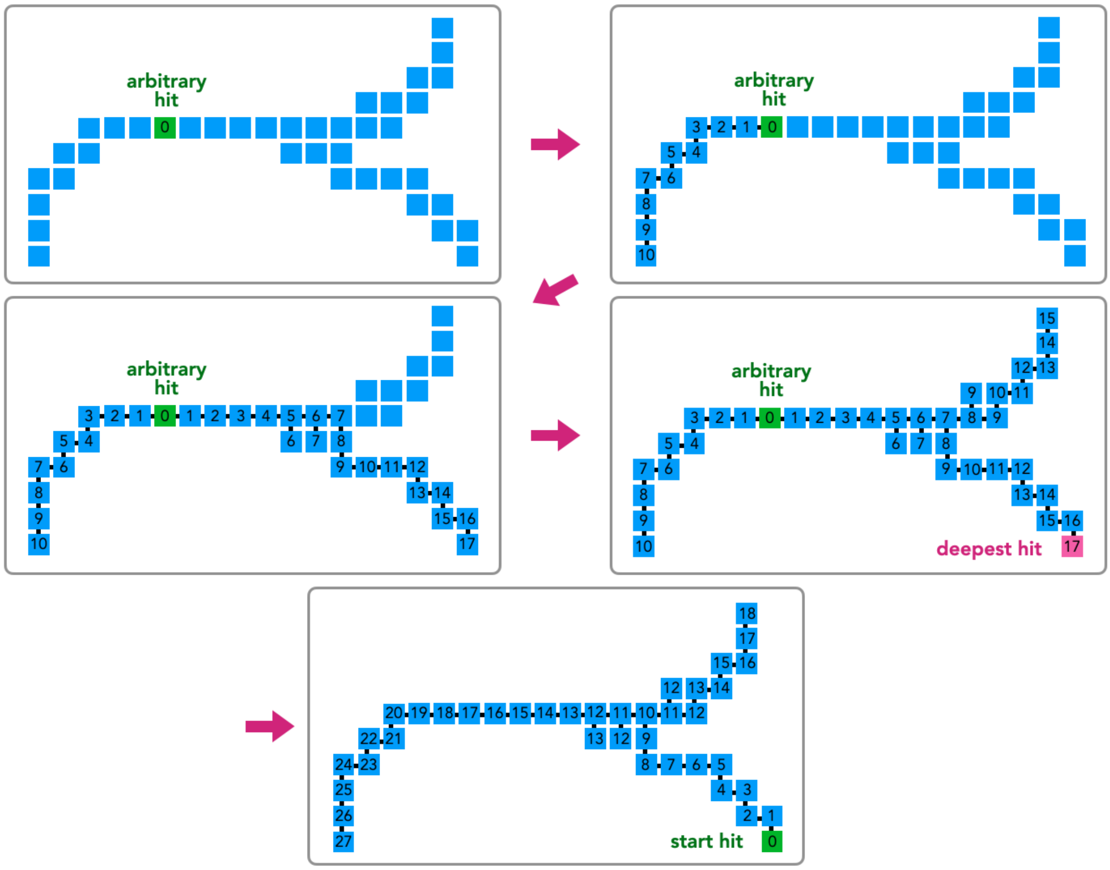

Figure C.3: Illustration of the construction of a minimum spanning tree.

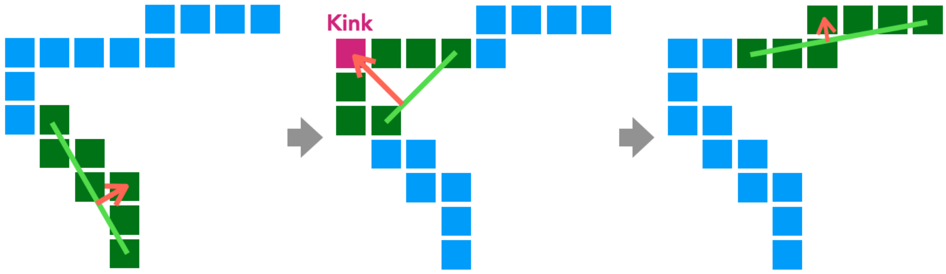

Figure C.4: Kink finding method

criteria, the furthest hit is assigned as a kink. If we find a kink in a cluster, we split it into two clusters at the kink position.

Cluster growth

Up to this point, we have small cluster segments connected via junctions and kinks. We grow such smaller clusters into larger track-like clusters. For cluster pairs that share a single hit, we compute a goodness of matching and combine them if they meet the criteria. The result of the linear fitting that is defined as the change in χ^2 to a line,

$$\Delta\chi^2 = \chi^2_{1+2} - \chi^2_1 - \chi^2_2, \tag{C.5}$$

is calculated. If this is less than 8.0, we combine these clusters. The χ^2 is for a single degrees of freedom and 8.0 has a p-value of about 0.5%. We continue this until there are no more candidates that can be combined.

Track construction and fitting

Track objects are constructed from the clusters created in the previous steps when they meet the average charge and the hit number criteria. We require the average charge larger than 15 photo-electrons per hit and at least 4 hits in the cluster. Each hit is saved as a node in track objects and will be used in the following track fitting.

We use the Sequential Importance Resampling (SIR) particle filter for track fitting in SuperFGD reconstruction. The detail explanation of the SIR particle filter is given in Section C.3. In order to apply the particle filter to the track fitting, we replace the time development with the cube-based objects ordered in a certain direction. These cube-based objects are referred to as nodes. Nodes are first generated from every cube hits that contribute to the track, but it will be handled as not attached to a single cube in the following reconstruction steps.

Then the track fitting is done in the following way:

1. Choose $M = 1000$ samples from an assumed prior distribution.
   (a) Choose 1000 points inside the first cube with directions toward the second cube.
2. Update the distribution by sequentially adding measurements.
   (a) Propagate each sample to the next measurement including the effect of the magnetic field and multiple scattering assuming a 500 MeV/c muon.
   (b) Weight each sample based on the likelihood of the measurement so that the weighted samples describe the posteriors including the measurements.
   (c) Calculate the sample average and covariance and save them as the track state at each node.
   (d) Repeat until the last node.
3. Resample the posterior when the number of samples that have a zero weight is larger than a threshold.
4. Use forward/backward smoothing to find the final state at each node.

After the track fit, we compute the local timing and local average charge per length for the track at each node. Local charge per length is calculated as an average of the charge measured near the node using a 30 mm Gaussian window to estimate the charge deposition at a node.

Track growth

After constructing and fitting tracks, we combine pairs of tracks that have a good match. The goodness of the track match is defined with the distance and direction of the end points of the two tracks. If the χ^2 of the linear fit between the end states is less than 16.0 and the changes in direction and the distance are small enough, we combine the track pair into one. The angle and the distance thresholds are 15.0° and 15.0 mm, respectively.

Cross-talk hits merging

For all hits that have not been reconstructed as a track, we check if they can be merged as cross-talk hits. We search for the highest charge neighbor hit that is part of a track and combine the hit into the track to which the neighbor belongs. After repeating this for all hits that are not associated with a track, we cluster them with using DBSCAN method again.

Shower reconstruction and particle identification

The shower reconstruction and the particle identification (PID) are the final steps in SuperFGD reconstruction. These are discussed in detail in the following sections.

C.2 Evaluation of the SuperFGD reconstruction performance

We evaluate the performance of the SuperFGD reconstruction in this section.

C.2.1 Charge reconstruction

We compare the true and reconstructed charge in cubes. The true charge is the true energy deposit converted into the number of photo-electrons with Eq. (B.1). The reconstructed charge is the sum of photo-electrons collected from three fibers after the correction of the fiber attenuation and the charge sharing.

Figure C.5 shows the relationships between the true charge deposit and the reconstructed charge deposit in a cube for μ^- particle gun samples. A soft linear correlation can be seen between the true and reconstructed charges. The ratio of the true charge to the reconstructed charge in a cube is shown in Figure C.6. Except for the low charge region, the ratio of the true charge to the reconstructed charge is around ~ 8. Since the half of the photo-electrons are wasted at one side of the fiber edge and the photon detection efficiency (PDE) of the MPPC is 25%, this is a reasonable value.

C.3 SIR particle filter for the track fitting

We use a Sequential Importance Resampling (SIR) particle filter for track fitting in SuperFGD reconstruction as described in Section C.1. A particle filter is a method to solve filtering problems [48]. In filtering problem, given

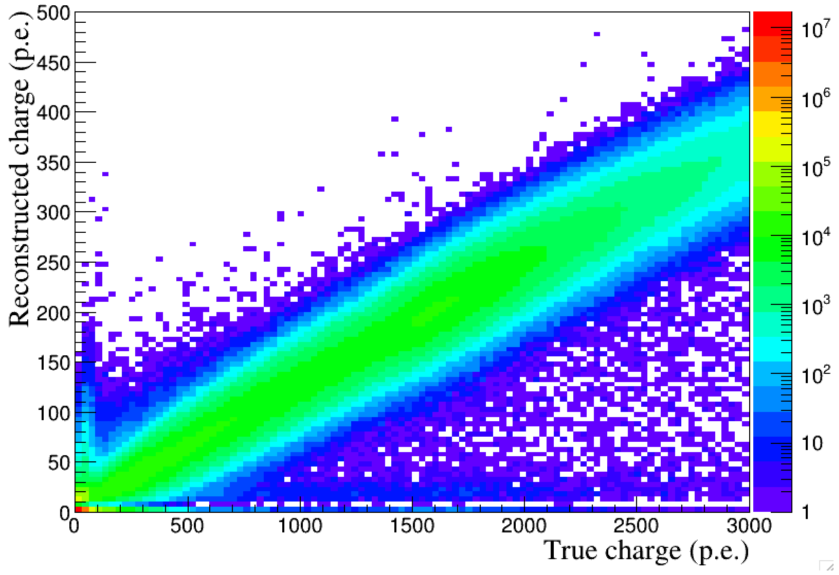

Figure C.5: Relationship between the true charge deposit and reconstructed charge in a cube for momentum-weighted μ^- particle gun samples. Charges are measured in terms of the number of photo-electrons.

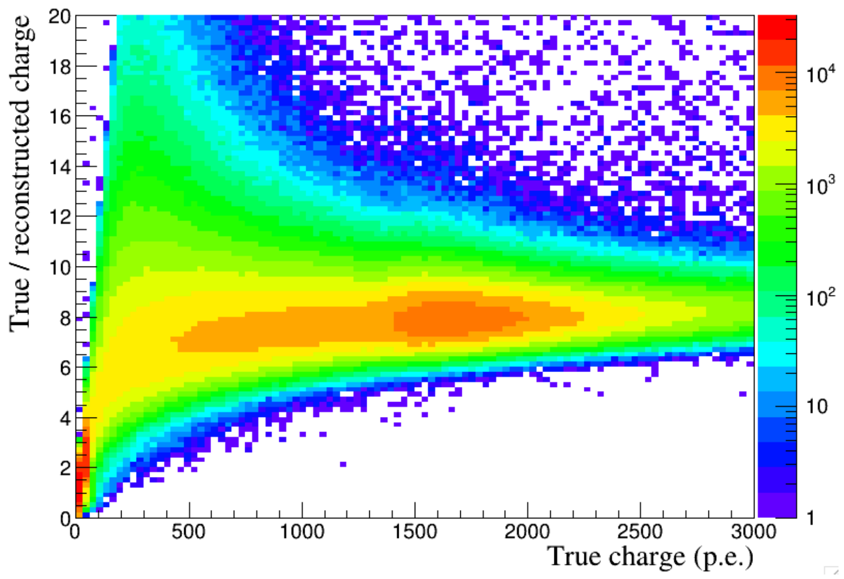

Figure C.6: Ratio of the true charge deposit to the reconstructed charge in a cube for momentum-weighted μ^- particle gun samples. Charges are measured in terms of the number of photo-electrons.

a set of partial observations for a dynamic system, we estimate the unobservable internal states. The unobservable states of the system at t is noted as $\boldsymbol{x}_t$. They follow the Markov process and evolve according to the transition probability density $p(\boldsymbol{x}_t|\boldsymbol{x}_{t-1}$. When the state is observed, the observed value is given as $\boldsymbol{y}_t$. The system equation and the observation equation is written as

$$\boldsymbol{x}_t = f(\boldsymbol{x}_{t-1}, \boldsymbol{\xi}_s, \boldsymbol{v}_t), \tag{C.6}$$

$$\boldsymbol{y}_t = h(\boldsymbol{x}_t, \boldsymbol{\xi}_m, \boldsymbol{\epsilon}_t). \tag{C.7}$$

where $\boldsymbol{v}_t$ is the system noise, $\boldsymbol{\epsilon_t}$ is the observation noise, and $\boldsymbol{\xi}_s$ and $\boldsymbol{\xi}_m$ are the parameters of the system equation and the observation equation. The goal of the filtering problem is to estimate the unknown state $\boldsymbol{x}_t$ with the observation $\boldsymbol{y}_t$ with using Eqn. (C.6) and (C.7).

Given a set of observation, a filtering distribution $p(\boldsymbol{x}|\boldsymbol{y}_{1:t})$ can be approximated as:

$$p(\boldsymbol{x}_t|\boldsymbol{y}_{1:t}) \simeq \sum_{i=1}^{M} \frac{w_t^i}{\sum_{i=1}^{M} w_t^i} \delta(\boldsymbol{x}_t - \boldsymbol{x}_{t|t-1}^i) \tag{C.8}$$

where $\boldsymbol{x}_{t|t-1}^i$ is the states generated by the Monte Carlo method with using Eqn. (C.6), w_t^i is the likelihood corresponding with the state $\boldsymbol{x}_{t|t-1}^i$, M is the number of trials with the Monte Carlo method. These states $\boldsymbol{x}_{t|t-1}^i$ and likelihood w_t^i are called particles (also called samples) and weights, respectively. Also, in the particle filter, we resample the particles at each step based on the weights. Noting the resampled particles as $\hat{\boldsymbol{x}}_t^i$, their weights are normalized into $1/M$ and the flitering distribution described in Eqn. (C.8) can be rewritten as:

$$p(\boldsymbol{x}_t|\boldsymbol{y}_{1:t}) \simeq \frac{1}{M} \sum_{i=0}^{M} \delta(\boldsymbol{x}_t - \hat{\boldsymbol{x}}_t^i). \tag{C.9}$$

The algorithm of the particle filter consists of (a) prediction, (b) likelihood calculation, and (c) resampling. At each step, we repeat the following procedures:

1. Repeat the following steps from $i = 1$ to $i = M$:

    (a) Prediction: produce particles $\boldsymbol{x}_{t|t-1}^i$ with Eqn. (C.6) by using the Monte Carlo method.

    (b) Likelihood calculation: calculate the weights from the predicted particles $\boldsymbol{x}_{t|t-1}^i$ and observed values $\boldsymbol{y}_t$ with Eqn. (C.7) as $w_t^i \simeq p(\boldsymbol{y}_t|\boldsymbol{x}_{t-1}^i)$.

2. Resampling: resample M particles from $\boldsymbol{x}^i_{t|t-1}$ $(i = 1, \ldots, M)$ so that the number of sampled particles are proportional to the weights w^i_t $(i = 1, \ldots, M)$.

3. Calculate Eqn. (C.9) with resampled particles $\hat{\boldsymbol{x}}^i_t$.

After finishing all steps $(t = 1, \ldots, T)$, the estimated state $\boldsymbol{x}_t$ is simply calculated by taking the median of $\hat{\boldsymbol{x}}_t$. Also, Eqn. (C.9) clearly shows that the distribution of $\hat{\boldsymbol{x}}_t$ $(i = 1, \ldots, M)$ corresponds to the probability density. Thus, the covariance of the estimated value can easily be computed.

Appendix D

Multivariate analysis methods

In this appendix, we describe the multivariate analysis methods used in this thesis. We use the Toolkit for Multivariate Data Analysis (TMVA) [49] provide by ROOT [50] for the analysis.

D.1 Boosted decision tree (BDT)

The decision tree is a binary tree structured classifier as shown in Figure D.1. Starting from the root node, samples are classified with repeated yes/no decisions on each node. The input phase space is split this way into many regions which classified as signal-like or background-like. The "leaf" nodes at the bottom end of the tree are labeled signal-like and background-like depending on the majority of samples that end up in the respective nodes. The decision tree has a weakness that it can easily affected by the statistical fluctuaitons in the training sample. Thus, we usually construct a set of decision trees which is so-called "forest". We classify samples based on the weighted vote of the classifications done by each tree in the forest.

When constructing a forest, we use a boosting algorithm called AdaBoost (adaptive boost). In AdaBoost, samples that are misclassified during the training of a decision tree are given a higher sample weight in the training of the following tree. The weights of the previously misclassified samples are multiplied by a common boost weight α, which compute with the misclassification rate of the privious tree ϵ as:

$$\alpha = \frac{1-\epsilon}{\epsilon}. \tag{D.1}$$

Then, the weights of the entire sample are normalized so that the sum of the weights should be constant. Finally, we decide the classification result with

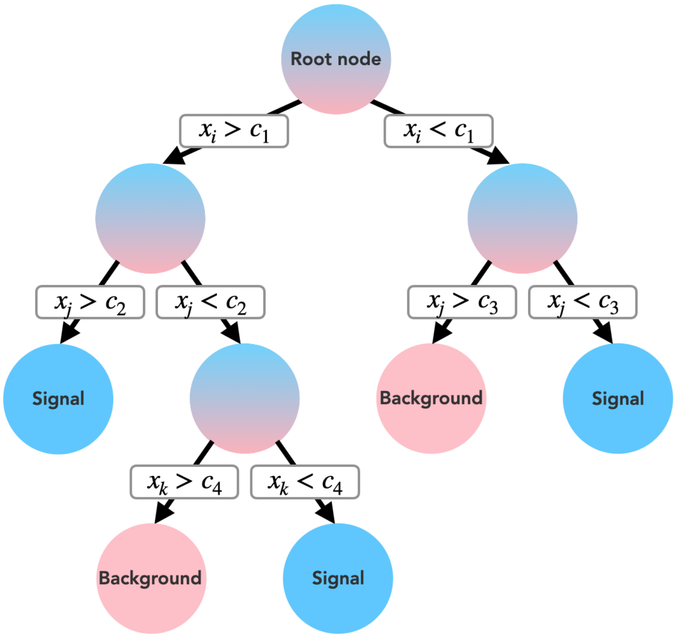

Figure D.1: Schematic view of a decision tree.

weighted vote of the all trees in the forest. The boosted sample classification $y_{\text{Boost}}(\boldsymbol{x})$ is given by

$$y_{\text{Boost}}(\boldsymbol{x}) = \frac{1}{N}\sum_{i=1}^{N} \ln(\alpha_i) h_i(\boldsymbol{x}), \tag{D.2}$$

where N is the number of trees in the forest and $h_i(\boldsymbol{x})$ is the result of i-th tree classifier, with encoded for signal and background as $h(\boldsymbol{x}) = +1$ and $h(\boldsymbol{x}) = -1$, respectively. Thus, a tree with smaller misclassification rate ϵ has a stronger contribution to the final classification result.

In this thesis, the depth of each tree is fixed at 3 and 800 trees are constructed.

D.2 k-nearest neighbor method (kNN)

The k-nearest neighbor method (kNN) compares a test sample to reference sample from a training data set. It searches for the number of adjacent samples in the feature phase space and decide the output from the plurality votes of neighbors as shown in Figure D.2. When searching for k samples that are closest to the test sample, closeness is measured using a metric function.

The simplest metric choice is the Euclidean distance:

$$R = \left(\sum_{i=1}^{n} |x_i - y_i|^2 \right)^{\frac{1}{2}}, \tag{D.3}$$

where n is the number of input variables used for the classification, x_i is the i-th coordinate of an event from a training sample and y_i is the i-th variable of an observed test sample. The k samples with the smallest values of R are selected as k-nearest neighbors. The number k is the sum of the number of signal and background training samples:

$$k = k_{\mathrm{S}} + k_{\mathrm{B}}. \tag{D.4}$$

Thus, the relative probability for the test sample being signal-like is given by:

$$P_{\mathrm{S}} = \frac{k_{\mathrm{S}}}{k_{\mathrm{S}} + k_{\mathrm{B}}} = \frac{k_{\mathrm{S}}}{k}. \tag{D.5}$$

In the actual application, input variables have different units and give a bias to the calculation of the distance. Thus, we put weights for each variables and rescale them based on the width of their distribution.

In this thesis, the number of k-nearest neighbors is fixed at 20.

D.3 Support vector machine (SVM)

The main idea of the support vector machine (SVM) algorithm is to build a hyperplane that separates signal and background samples using only a minimal subset of all training samples so-called "support vectors". The position of the hyperplane is obtained by maximizing the margin between it and the support vectors.

Considering a simple two-class classifier with oriented hyperplane, if the training data is linearly separable, it satisfy the constraints:

$$y_i(\vec{x}_i \cdot \vec{w} + b) - 1 \geq 0, \tag{D.6}$$

where $\vec{x}_i$ is the input vector of the i-th data, y_i is the desired output ($y_i = \pm 1$), and the pair $(\vec{w}, b)$ defines the hyperplane. For non-separatable data, the classification constraints are modified by adding a so-called "slack" variable ξ_i as :

$$y_i(\vec{x}_i \cdot \vec{w} + b) - 1 + \xi_i \geq 0. \tag{D.7}$$

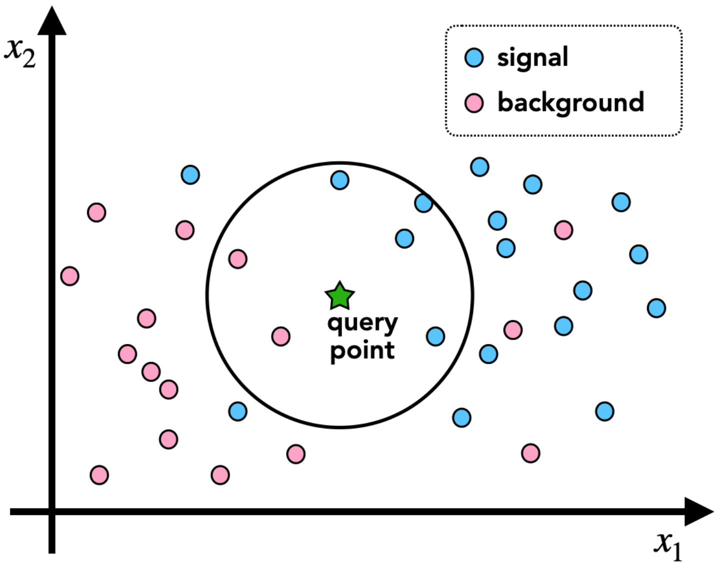

Figure D.2: Example for the k-nearest neighboring method in a two dimensional space. The k-NN algorithm searches for $k = 5$ nearest points and find 6 signal and 2 background points, thus the query point is classified as a signal.

The slack variable is $\xi_i = 0$ if the samples are properly classified, otherwise ξ_i is the distance to the dicision hyperplane ($\xi_i \geq 0$). This admits a certain amount of misclassification.

The classifier with the largest margin will give better separation. The margin for this linear classifier is just $2/|\vec{w}|$. Thus, the training algorithm minimize the cost function:

$$W = \frac{1}{2}|\vec{w}|^2 + C\sum_i \xi_i, \tag{D.8}$$

describing the trade-off between margin and misclassification. The illustration of an example of the SVM algorithm is shown in Figure D.3.

Also, the SVM can be extended to a nonlinear SVM which can classify nonlinear separable data. We use the Gaussian kernel function for this study.

D.4 Maximum likelihood method

The maximum likelihood method builds a probability density functions (PDF) from the signal and background input variables. For a given event, the likelihood for being of signal type is obtained by multiplying the signal probability

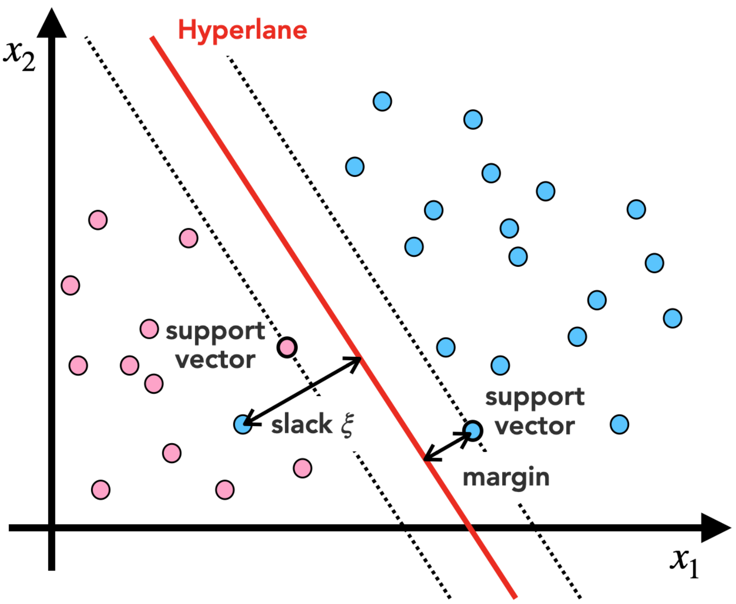

Figure D.3: Linear hyperplane classifier in a two dimensional phase space.

density of all input variables. Then it is normalized by the sum of the signal and background likelihoods. The likelihood ratio $y_{\mathcal{L}}(i)$ for sample i is defined by:

$$y_{\mathcal{L}}(i) = \frac{\mathcal{L}_{\mathrm{S}}(i)}{\mathcal{L}_{\mathrm{S}}(i) + \mathcal{L}_{\mathrm{B}}(i)}, \tag{D.9}$$

where

$$\mathcal{L}_{\mathrm{S(B)}}(i) = \prod_{k=1}^{n} p_{\mathrm{S(B)},k}(x_k(i)), \tag{D.10}$$

and where $p_{\mathrm{S(B)},k}$ is the signal (background) PDF for the k-th input variable x_k and n is the number of input variables.

Since the parametric form of the PDFs is generally unknown, the PDF shapes are approximated from the variable distributions of training data.

Appendix E

Supplemental plots and event displays

E.1 Plots

E.1.1 Angular dependence of the BDT response

The PID discriminator responses as a function of the particle angle for signal and background samples are shown in Figures E.1 and E.2, respectively. We cannot see any clear angular dependencies for the responses of the PID discriminators.

E.1.2 Momentum and angular distribution of selected particle gun events

Figures E.3 and E.4 show the momentum distributions of selected events for contained particle gun samples at each step of the selection. Also, figures E.5 and E.6 shows the angular distributions of selected events for contained particle gun samples at each step of the selection.

E.1.3 Particle gun selection efficiency as a function of angle

The selection efficiencies and the misidentification rates for contained and escaping particles as a function of the particle angle are shown in Figure E.7 and E.8. The angle is defined as the cosine between the particle direction and the beam direction (z-axis).

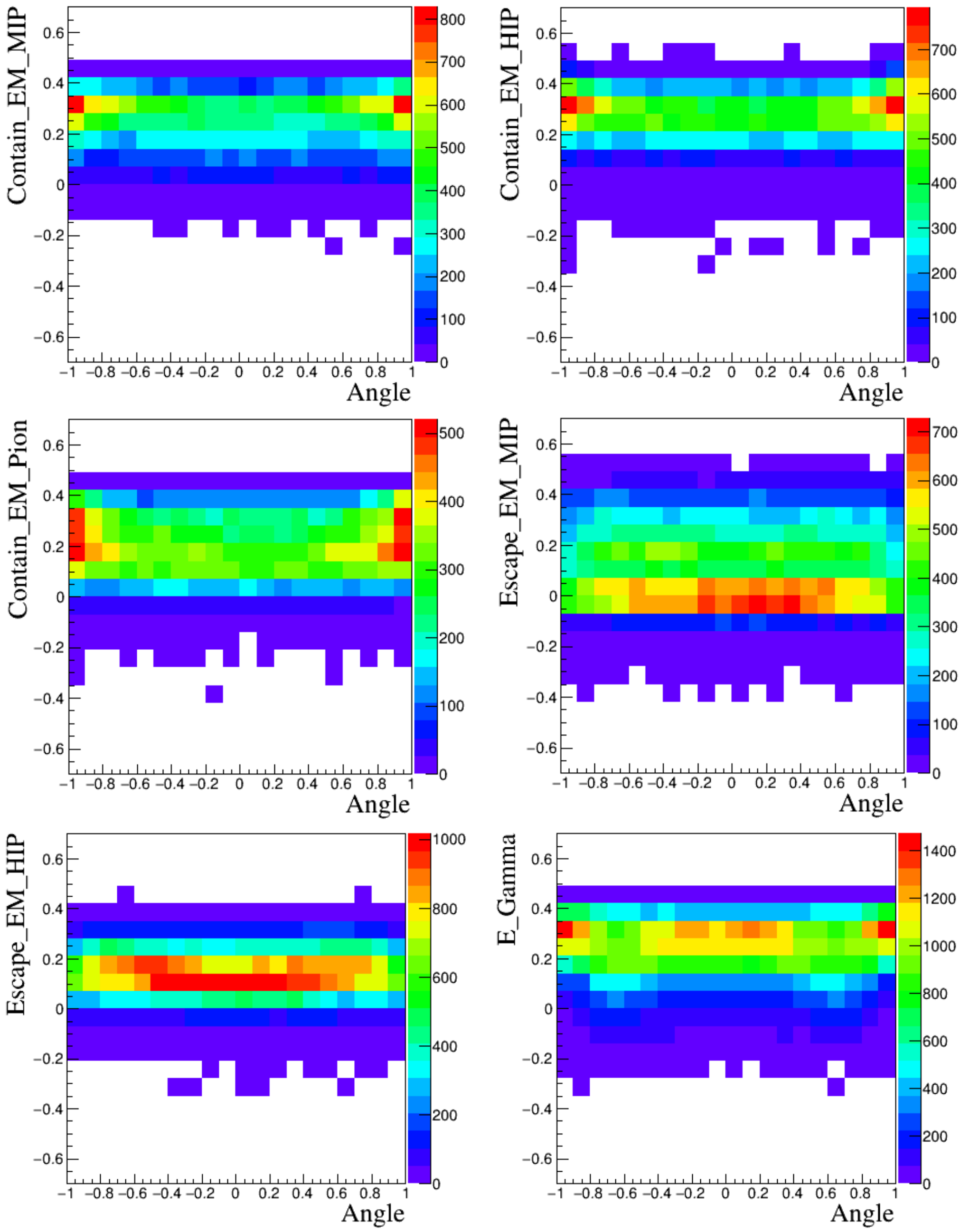

Figure E.1: PID discriminator responses as a function of the angle for signal (e^-) particle gun samples.

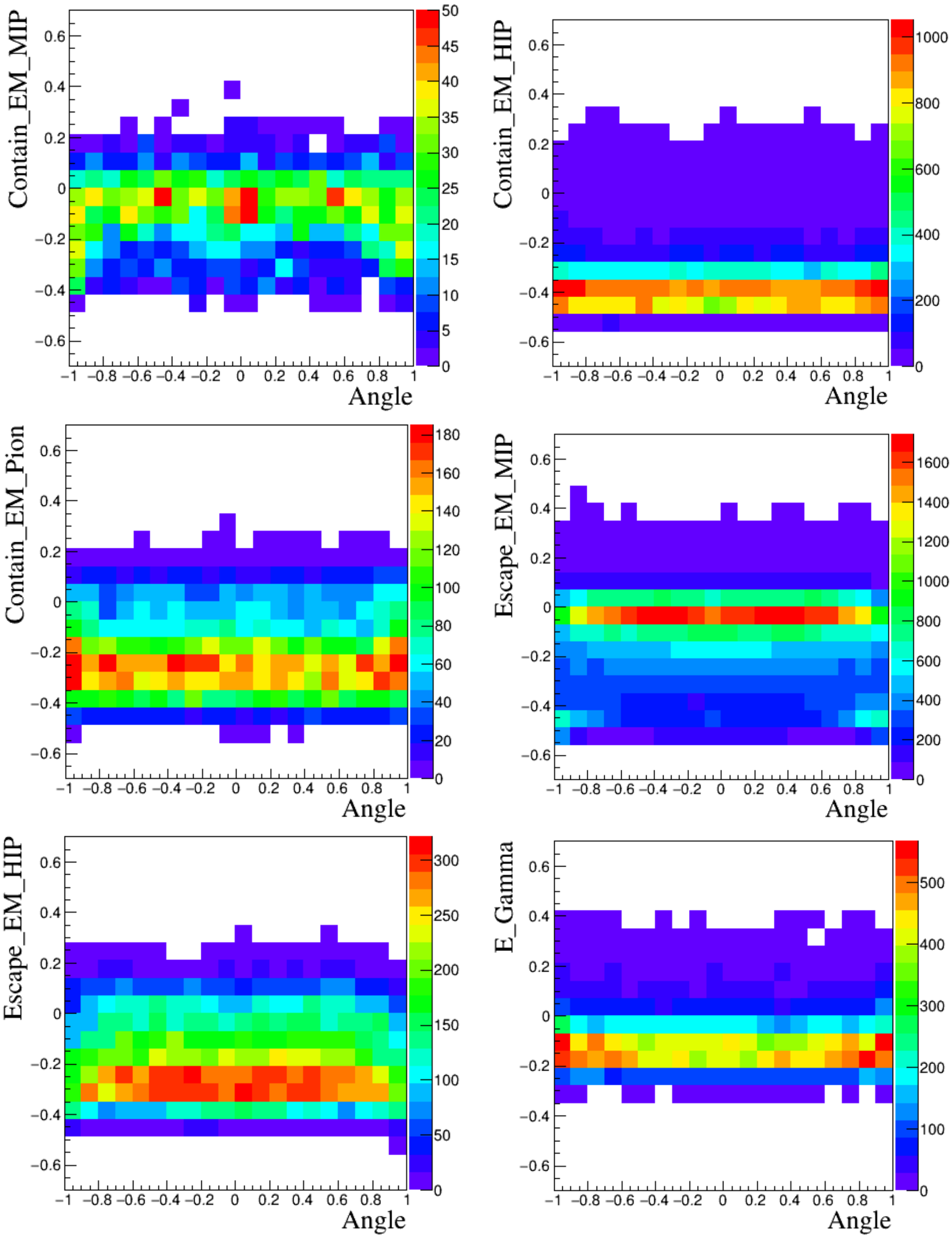

Figure E.2: PID discriminator responses as a function of the angle for background particle gun samples.

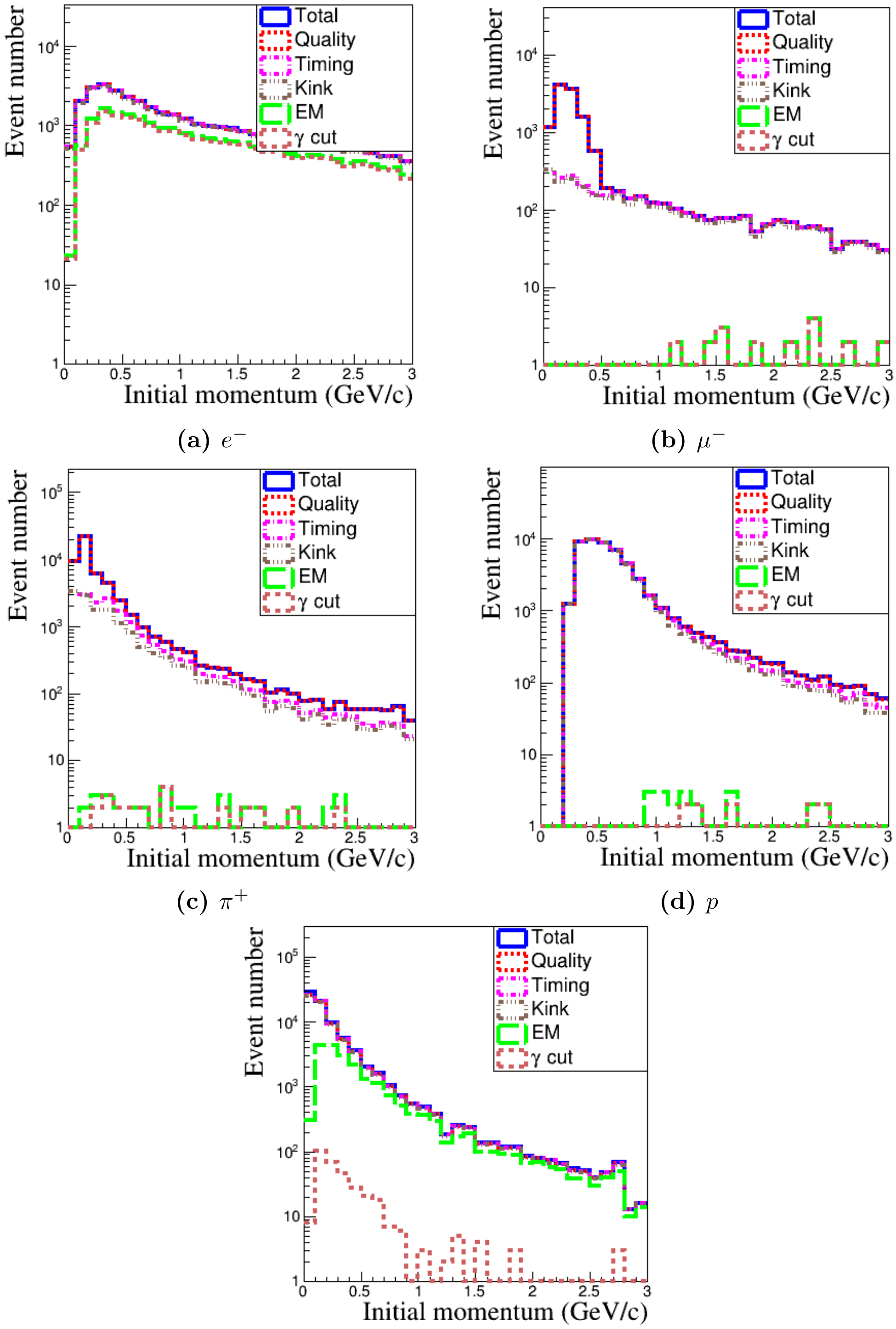

(a) e^- **(b)** μ^- **(c)** π^+ **(d)** p **(e)** γ

Figure E.3: Momentum distributions of selected events at each step of the selection for the contained particles.

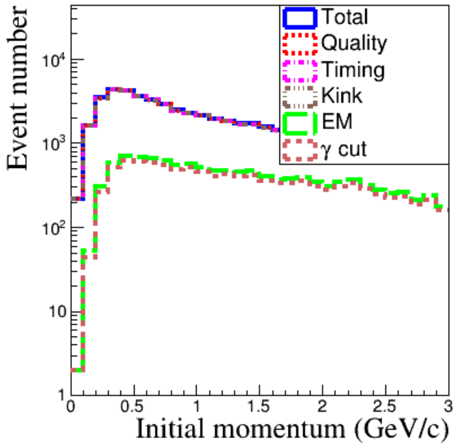

(a) e^-

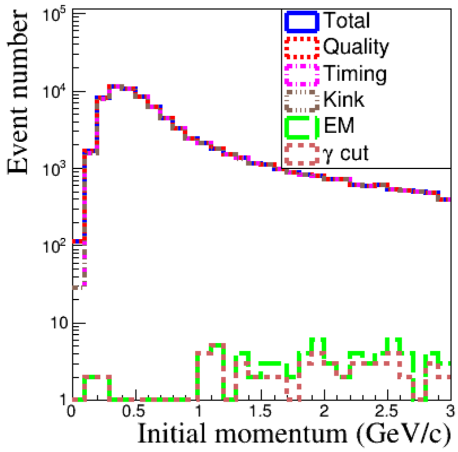

(b) μ^-

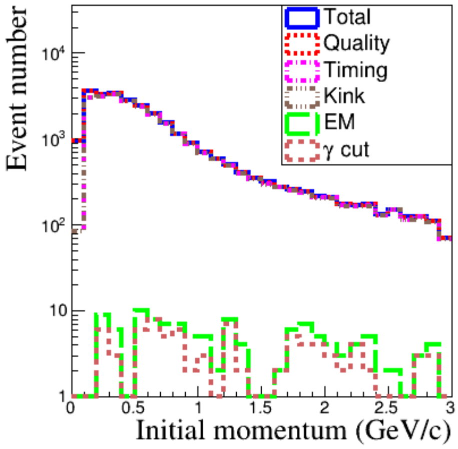

(c) π^+

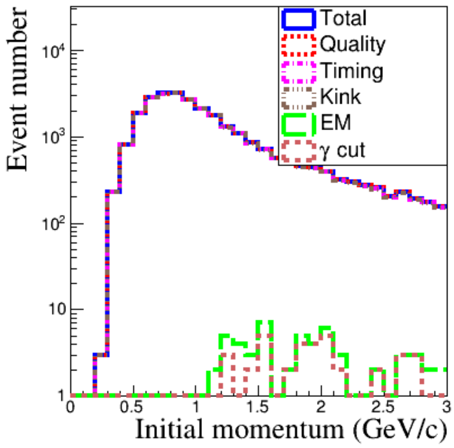

(d) p

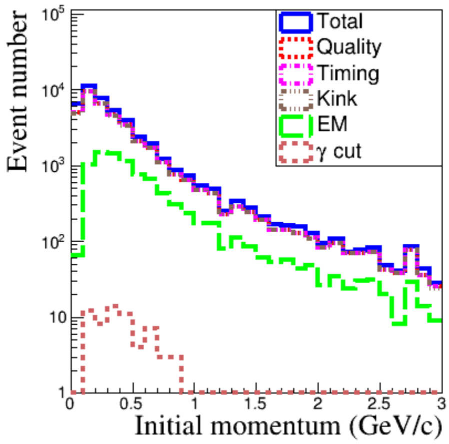

(e) γ

Figure E.4: Momentum distributions of selected events at each step of the selection for the escaping particles.

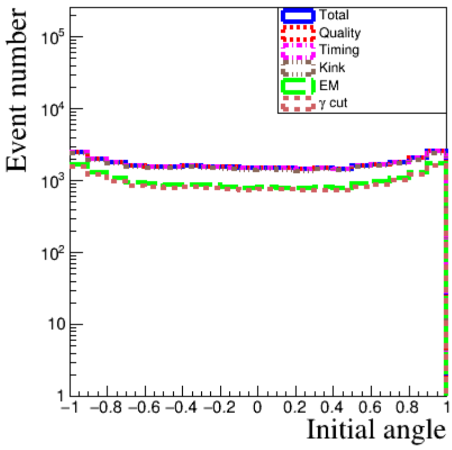

(a) e^-

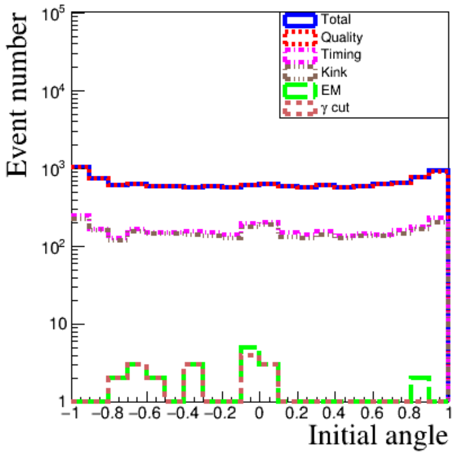

(b) μ^-

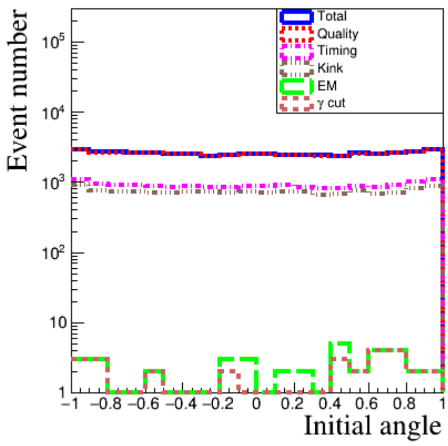

(c) π^+

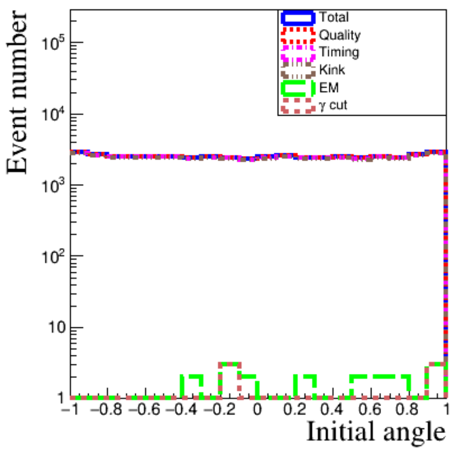

(d) p

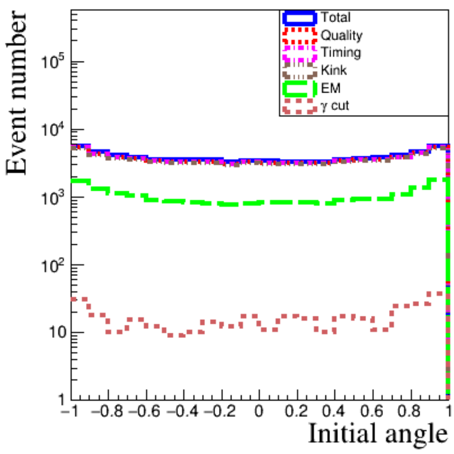

(e) γ

Figure E.5: Angular distributions of selected events at each step of the selection for the contained particles.

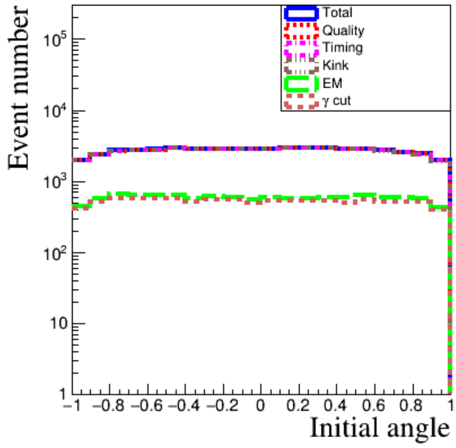

(a) e^-

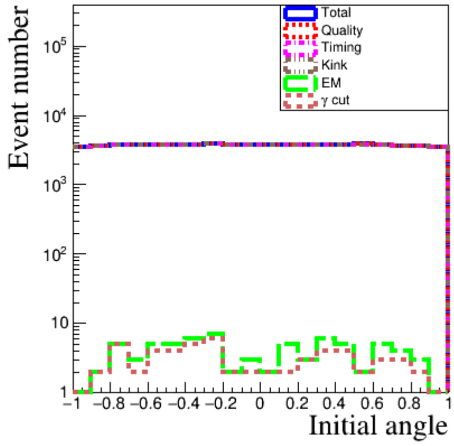

(b) μ^-

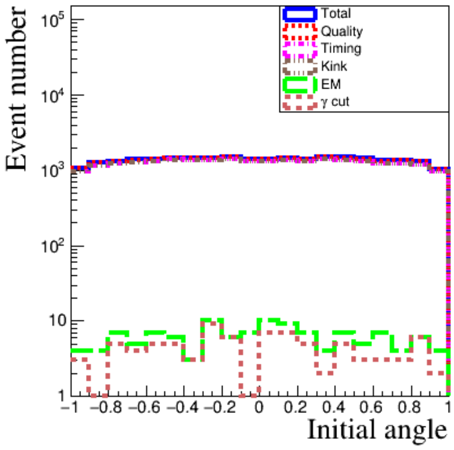

(c) π^+

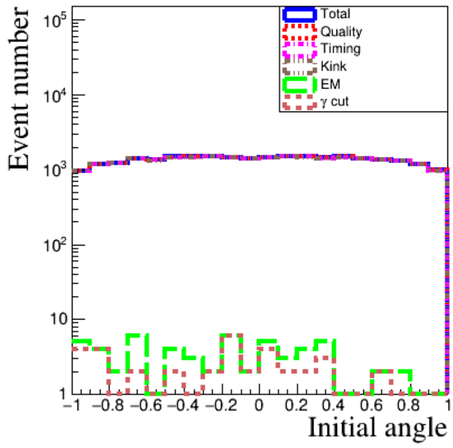

(d) p

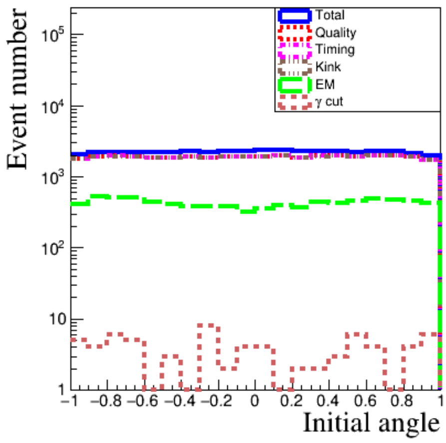

(e) γ

Figure E.6: Angular distributions of selected events at each step of the selection for the escaping particles.

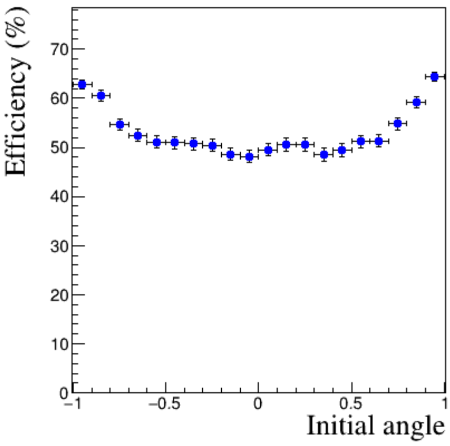

(a) Efficiency for e^-

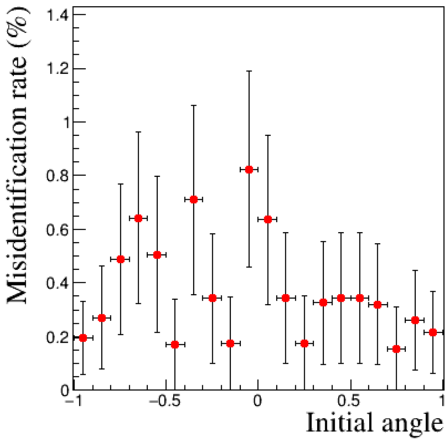

(b) Misidentification rate for μ^-

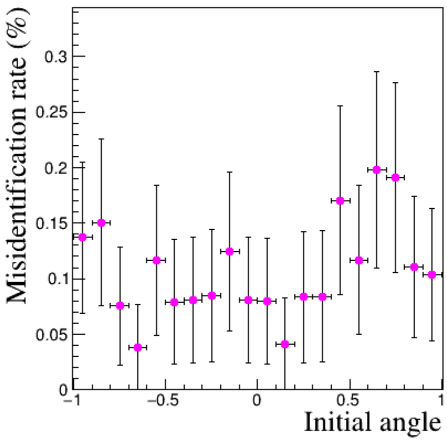

(c) Misidentification rate for π^+

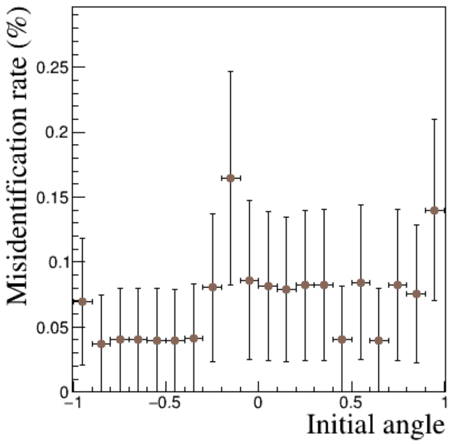

(d) Misidentification rate for p

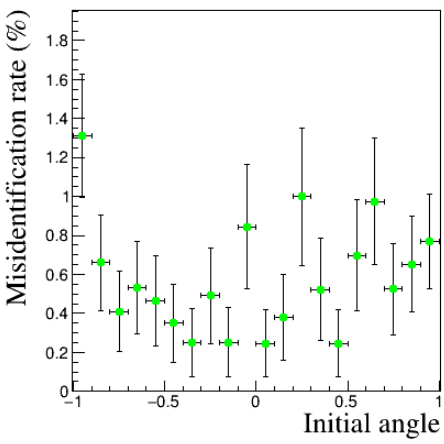

(e) Misidentification rate for γ

Figure E.7: Selection efficiency and misidentification rate for contained particle gun samples as a function of angle.

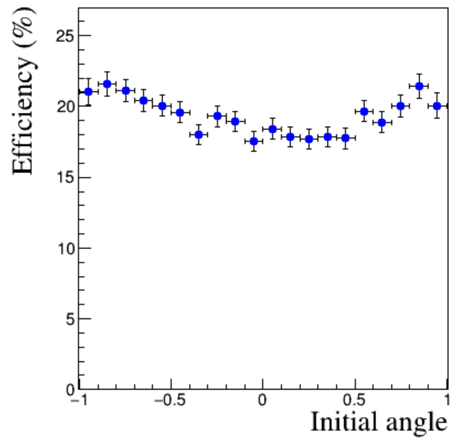

(a) Efficiency for e^-

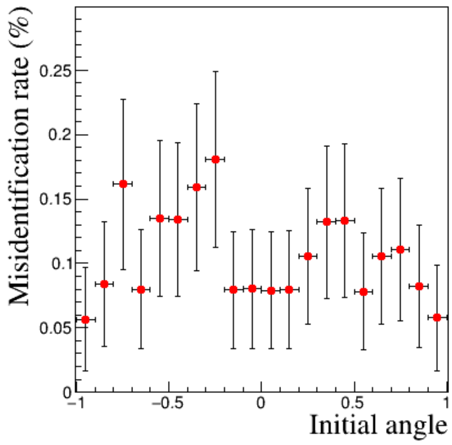

(b) Misidentification rate for μ^-

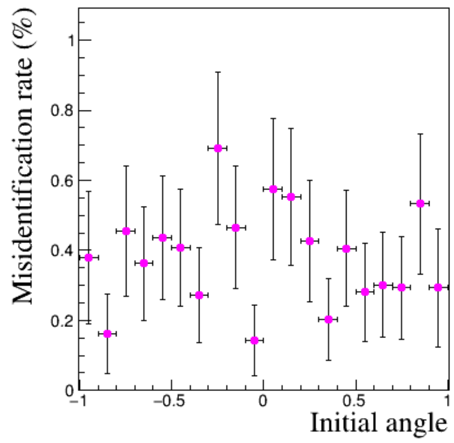

(c) Misidentification rate for π^+

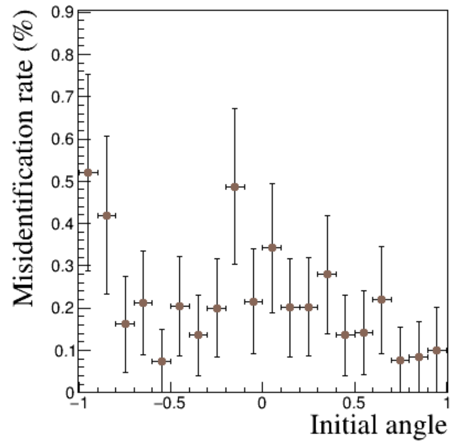

(d) Misidentification rate for p

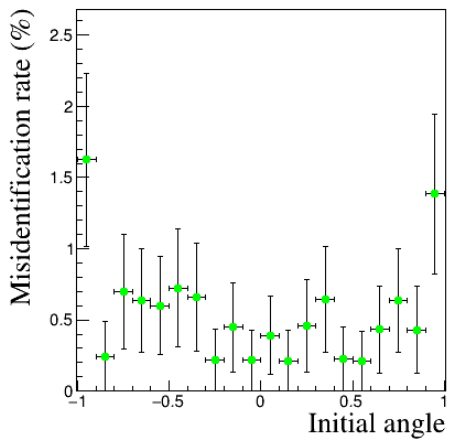

(e) Misidentification rate for γ

Figure E.8: Selection efficiency and misidentification rate for escaping particle gun samples as a function of angle.

E.2 Event displays

E.2.1 Timing cut

The event displays for the muon and pion tracks that are rejected with this Michel electron cut are shown in Figure E.9.

E.2.2 Kink cut

Event displays for the pion tracks that are rejected by this kink cut are shown in Figure E.10.

E.2.3 Misidentified particle gun samples

Figures E.11, E.12, E.13, and E.14 show the event displays of background samples that are misidentified as an electron.

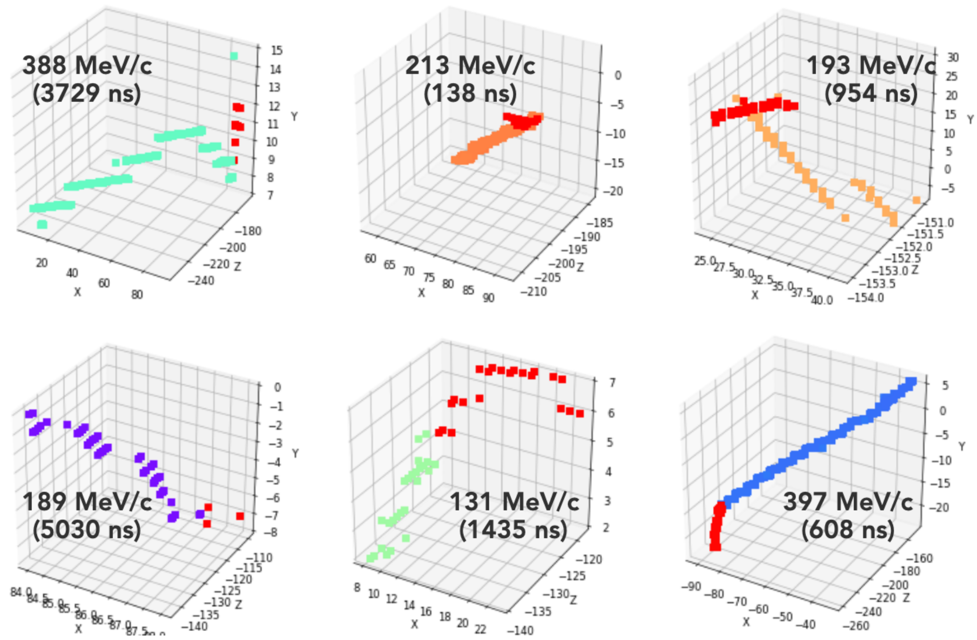

(a) μ^-

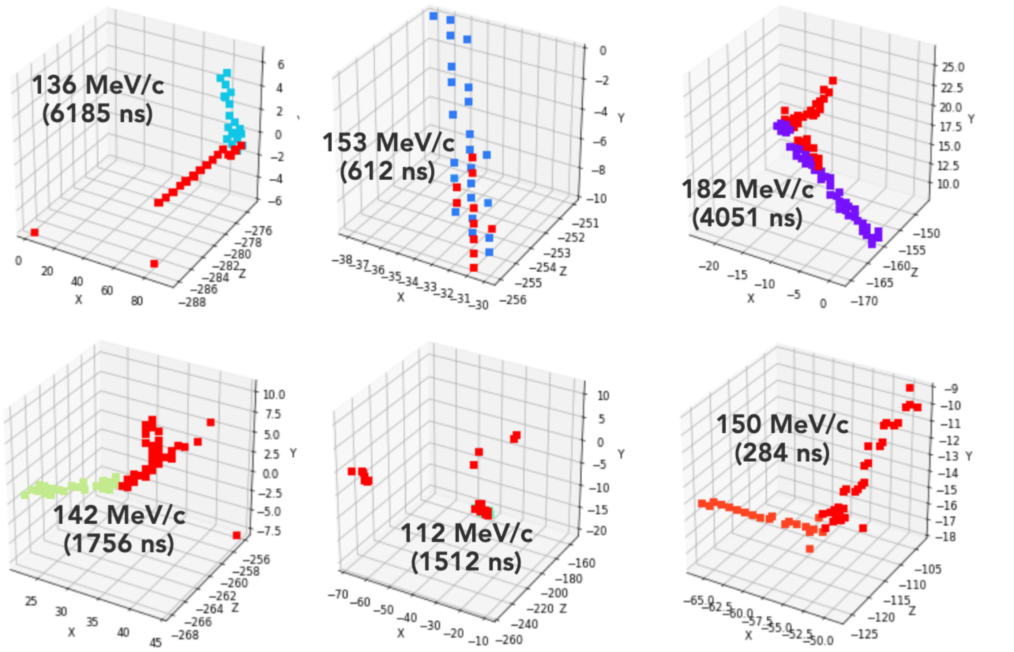

(b) π^+

Figure E.9: Event displays for the randomly chosen μ^- and π^+ particle gun samples that are rejected with the timing cut. Captions show the true momentum of the primary particle and the reconstructed timing difference. Colors corresponds to the reconstructed timing for each cube.

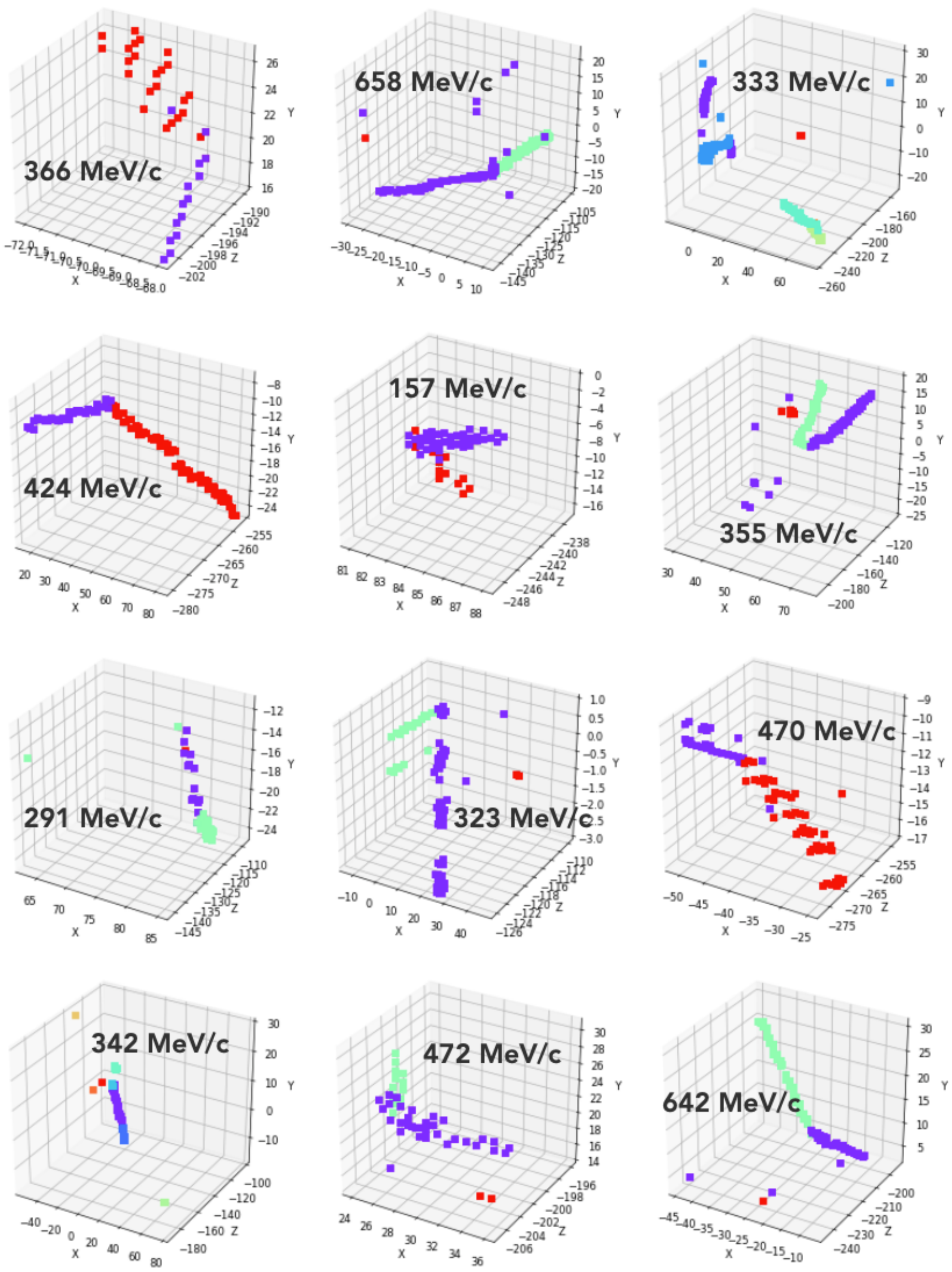

Figure E.10: Event displays for the randomly chosen pion events that are rejected with the kink cut. Captions show the true momentum of the primary particle. Colors correspond to the reconstructed track and cluster objects to which a hit belongs.

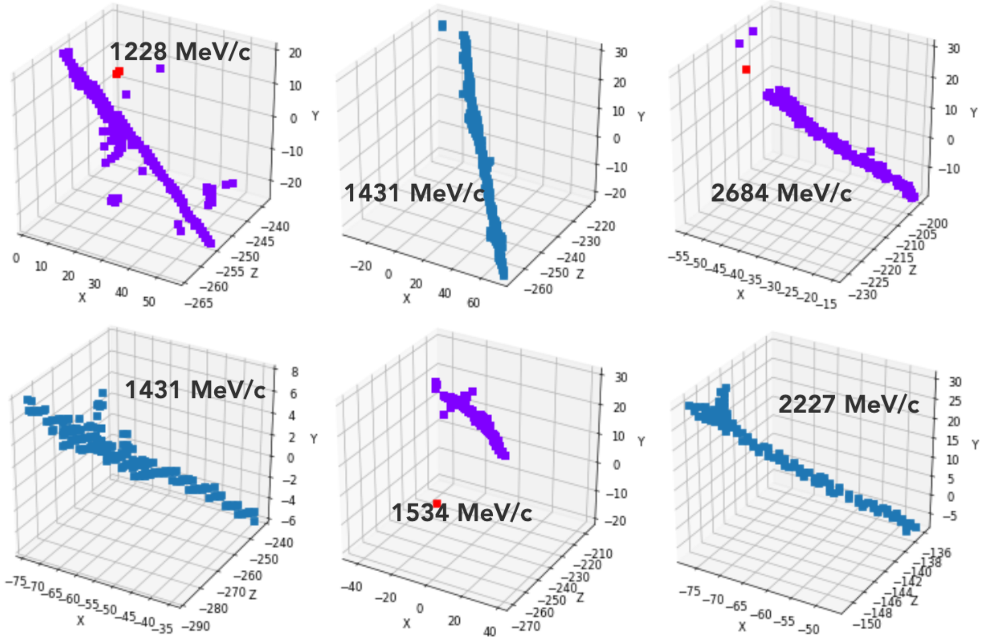

(a) Contained particle

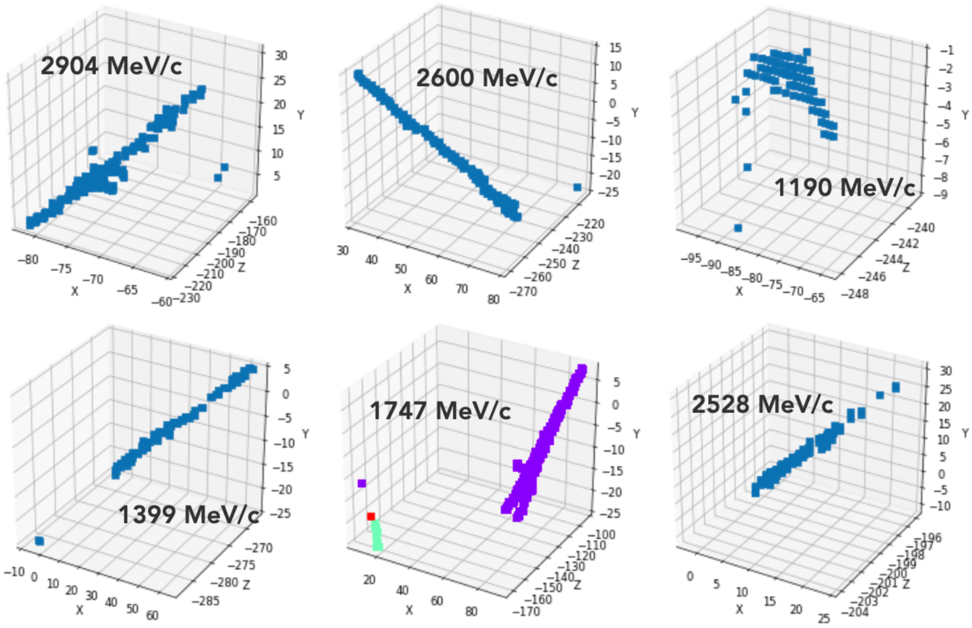

(b) Escaping particle

Figure E.11: Event displays for the randomly chosen μ^- events that are misidentified as an electron. Captions show the true momentum of the particle. Colors correspond to the reconstructed track and cluster objects to which a hit belongs.

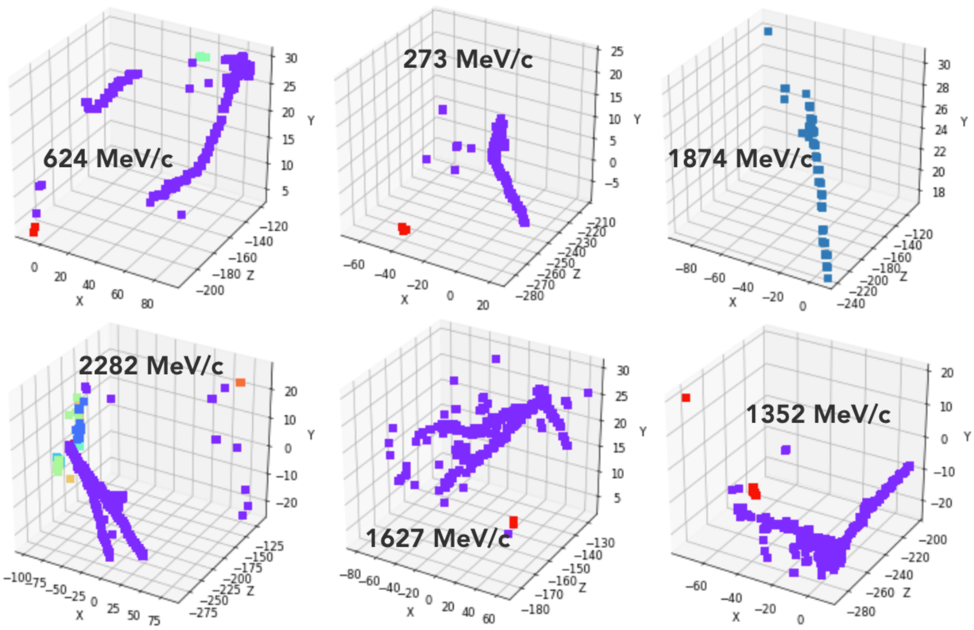

(a) Contained particle

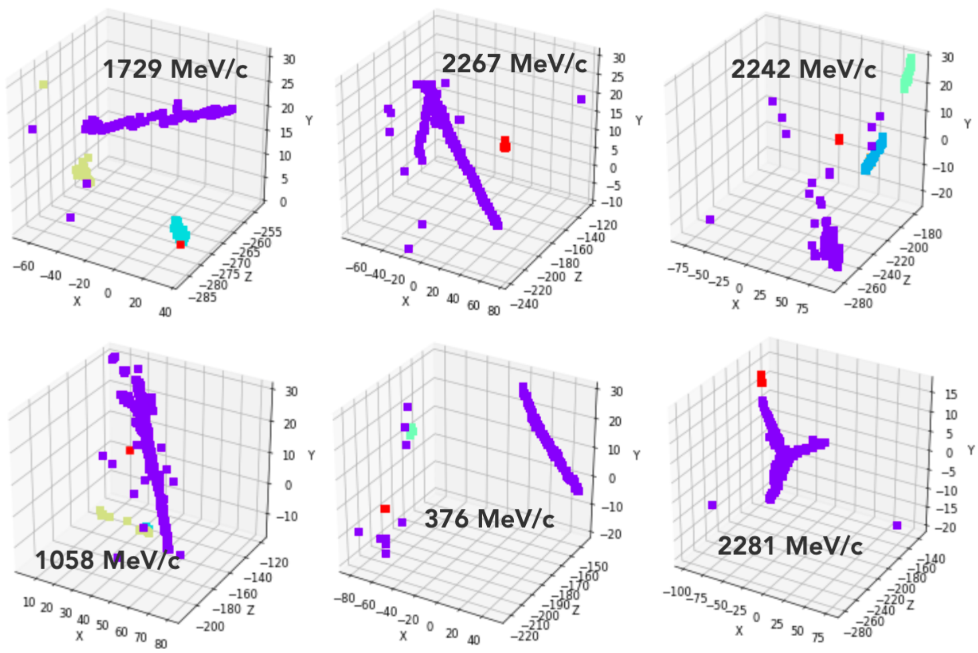

(b) Escaping particle

Figure E.12: Event displays for the randomly chosen π^+ events that are misidentified as an electron. Captions show the true momentum of the particle. Colors correspond to the reconstructed track and cluster objects to which a hit belongs.

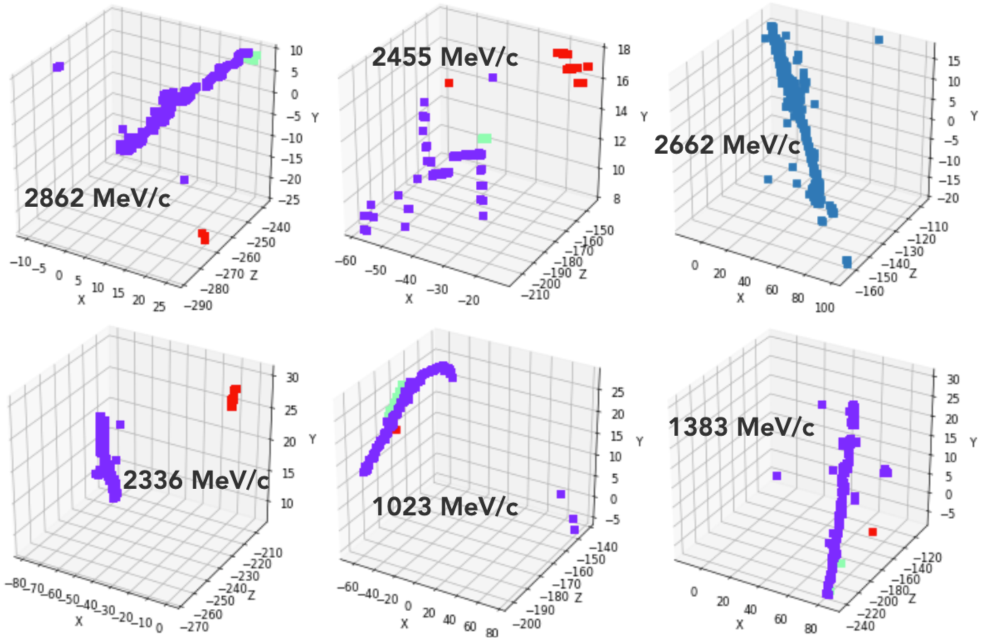

(a) Contained particle

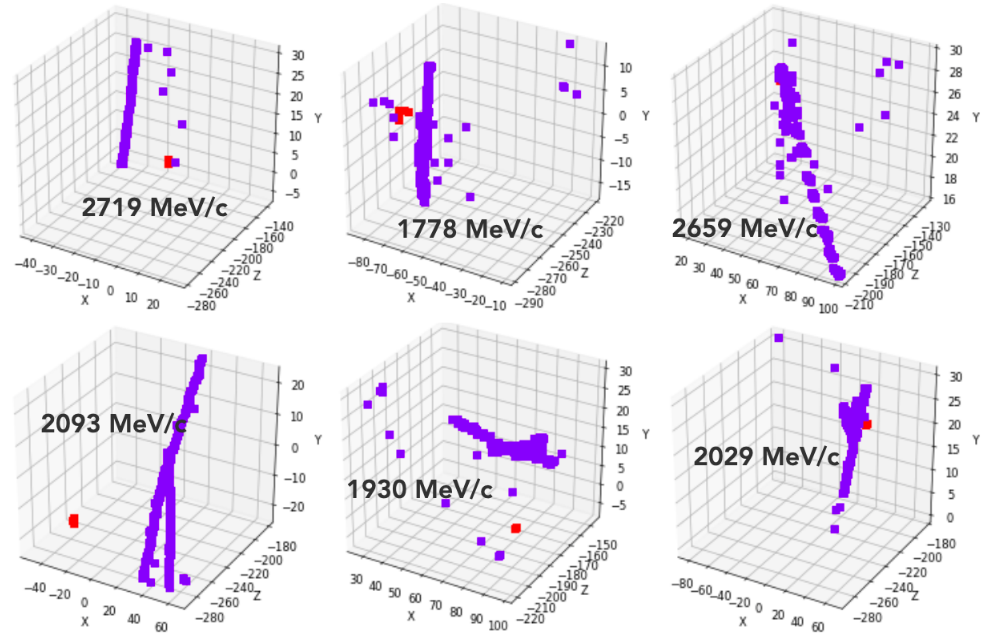

(b) Escaping particle

Figure E.13: Event displays for the randomly chosen p events that are misidentified as an electron. Captions show the true momentum of the particle. Colors correspond to the reconstructed track and cluster objects to which a hit belongs.

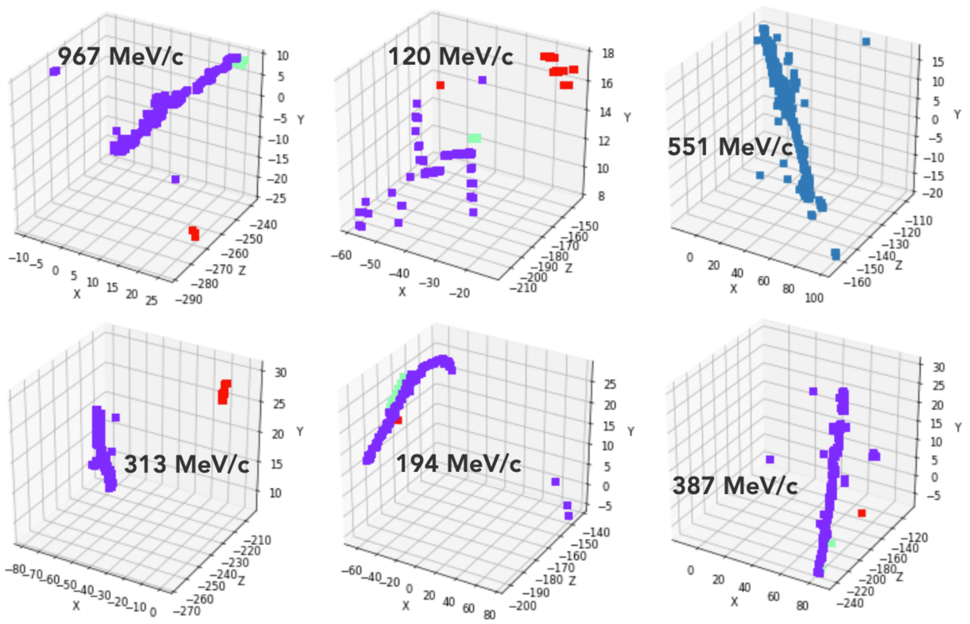

(a) Contained particle

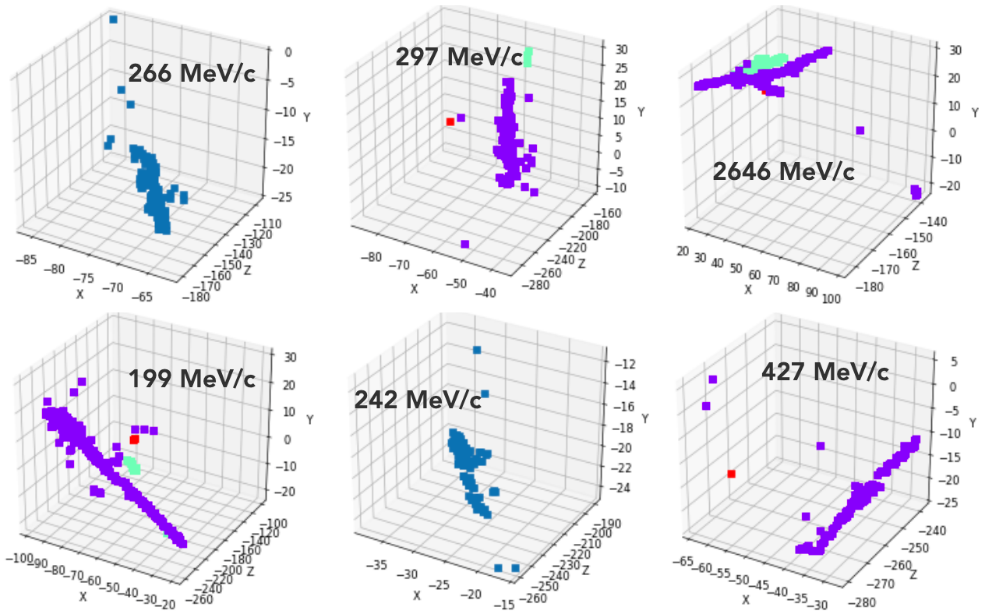

(b) Escaping particle

Figure E.14: Event displays for the randomly chosen γ events that are misidentified as an electron. Captions show the true momentum of the particle. Colors correspond to the reconstructed track and cluster objects to which a hit belongs.

List of Figures

List of Tables

Bibliography

[1] Y. Fukuda et al. “Evidence for Oscillation of Atmospheric Neutrinos”. In: *Phys. Rev. Lett.* 81 (8 Aug. 1998), pp. 1562–1567. DOI: 10.1103/PhysRevLett.81.1562. URL: https://link.aps.org/doi/10.1103/PhysRevLett.81.1562.

[2] Particle Data Group. “Review of Particle Physics”. In: *Progress of Theoretical and Experimental Physics* 2020.8 (Aug. 2020). 083C01. ISSN: 2050-3911. DOI: 10.1093/ptep/ptaa104. eprint: https://academic.oup.com/ptep/article-pdf/2020/8/083C01/34673722/ptaa104.pdf. URL: https://doi.org/10.1093/ptep/ptaa104.

[3] Manuela Boscolo, Jean-Pierre Delahaye, and Mark Palmer. “The Future Prospects of Muon Colliders and Neutrino Factories”. In: *Reviews of Accelerator Science and Technology.* 2019, pp. 189–214. DOI: 10.1142/9789811209604_0010. eprint: https://www.worldscientific.com/doi/pdf/10.1142/9789811209604_0010. URL: https://www.worldscientific.com/doi/abs/10.1142/9789811209604_0010.

[4] Cristina Volpe. “Beta-beams”. In: *Journal of Physics G: Nuclear and Particle Physics* 34.1 (Nov. 2006), R1–R44. DOI: 10.1088/0954-3899/34/1/r01. URL: https://doi.org/10.1088/0954-3899/34/1/r01.

[5] A. de Gouvea et al. “Working Group Report: Neutrinos”. In: *Community Summer Study 2013: Snowmass on the Mississippi.* Oct. 2013. arXiv: 1310.4340 [hep-ex].

[6] M. A. Acero et al. “New constraints on oscillation parameters from ν_e appearance and ν_μ disappearance in the NOvA experiment”. In: *Phys. Rev. D* 98 (3 Aug. 2018), p. 032012. DOI: 10.1103/PhysRevD.98.032012. URL: https://link.aps.org/doi/10.1103/PhysRevD.98.032012.

[7] Melanie Day and Kevin S. McFarland. “Differences in quasielastic cross sections of muon and electron neutrinos”. In: *Phys. Rev. D* 86 (5 Sept. 2012), p. 053003. DOI: 10.1103/PhysRevD.86.053003. URL: https://link.aps.org/doi/10.1103/PhysRevD.86.053003.

[8] J. Blietschau et al. “Total cross sections for ν_e and $\bar{\nu}_e$ interactions and search for neutrino oscillations and decay”. In: *Nuclear Physics B* 133.2 (1978), pp. 205–219. ISSN: 0550-3213. DOI: https://doi.org/10.1016/0550-3213(78)90299-7. URL: http://www.sciencedirect.com/science/article/pii/0550321378902997.

[9] K. Abe et al. “Measurement of the Inclusive Electron Neutrino Charged Current Cross Section on Carbon with the T2K Near Detector”. In: *Phys. Rev. Lett.* 113 (24 Dec. 2014), p. 241803. DOI: 10.1103/PhysRevLett.113.241803. URL: https://link.aps.org/doi/10.1103/PhysRevLett.113.241803.

[10] J. Wolcott et al. “Measurement of Electron Neutrino Quasielastic and Quasielasticlike Scattering on Hydrocarbon at $E_\nu = 3.6$ GeV”. In: *Phys. Rev. Lett.* 116 (8 Feb. 2016), p. 081802. DOI: 10.1103/PhysRevLett.116.081802. URL: https://link.aps.org/doi/10.1103/PhysRevLett.116.081802.

[11] K. Abe et al. “Measurement of the charged-current electron (anti-)neutrino inclusive cross-sections at the T2K off-axis near detector ND280”. In: *JHEP* 10 (2020), p. 114. DOI: 10.1007/JHEP10(2020)114. arXiv: 2002.11986 [hep-ex].

[12] K. Abe et al. “The T2K experiment”. In: *Nuclear Instruments and Methods in Physics Research Section A: Accelerators, Spectrometers, Detectors and Associated Equipment* 659.1 (2011), pp. 106–135. ISSN: 0168-9002. DOI: https://doi.org/10.1016/j.nima.2011.06.067. URL: http://www.sciencedirect.com/science/article/pii/S0168900211011910.

[13] K. Abe et al. “First combined measurement of the muon neutrino and antineutrino charged-current cross section without pions in the final state at T2K”. In: 26 (2020), pp. 1–44. arXiv: 2002.09323. URL: http://arxiv.org/abs/2002.09323.

[14] K. Matsuoka et al. “Design and performance of the muon monitor for the T2K neutrino oscillation experiment”. In: *Nuclear Instruments and Methods in Physics Research Section A: Accelerators, Spectrometers, Detectors and Associated Equipment* 624.3 (2010), pp. 591–600. ISSN: 0168-9002. DOI: https://doi.org/10.1016/j.nima.2010.09.074. URL: http://www.sciencedirect.com/science/article/pii/S016890021002098X.

[15] K. Abe et al. "First combined measurement of the muon neutrino and antineutrino charged-current cross section without pions in the final state at T2K". In: *Phys. Rev. D* 101 (11 June 2020), p. 112001. DOI: 10.1103/PhysRevD.101.112001. URL: https://link.aps.org/doi/10.1103/PhysRevD.101.112001.

[16] P.A. Amaudruz et al. "The T2K Fine-Grained Detectors". In: *Nucl. Instrum. Meth. A* 696 (2012), pp. 1–31. DOI: 10.1016/j.nima.2012.08.020. arXiv: 1204.3666 [physics.ins-det].

[17] N. Abgrall et al. "Time Projection Chambers for the T2K Near Detectors". In: *Nucl. Instrum. Meth. A* 637 (2011), pp. 25–46. DOI: 10.1016/j.nima.2011.02.036. arXiv: 1012.0865 [physics.ins-det].

[18] I. Giomataris et al. "Micromegas in a bulk". In: *Nuclear Instruments and Methods in Physics Research Section A: Accelerators, Spectrometers, Detectors and Associated Equipment* 560.2 (2006), pp. 405–408. ISSN: 0168-9002. DOI: https://doi.org/10.1016/j.nima.2005.12.222. URL: http://www.sciencedirect.com/science/article/pii/S0168900205026501.

[19] S. Assylbekov et al. "The T2K ND280 Off-Axis Pi-Zero Detector". In: *Nucl. Instrum. Meth. A* 686 (2012), pp. 48–63. DOI: 10.1016/j.nima.2012.05.028. arXiv: 1111.5030 [physics.ins-det].

[20] D. Allan et al. "The Electromagnetic Calorimeter for the T2K Near Detector ND280". In: *JINST* 8 (2013), P10019. DOI: 10.1088/1748-0221/8/10/P10019. arXiv: 1308.3445 [physics.ins-det].

[21] K. Abe et al. "Constraint on the matter–antimatter symmetry-violating phase in neutrino oscillations". In: *Nature* 580.7803 (2020), pp. 339–344. ISSN: 14764687. DOI: 10.1038/s41586-020-2177-0. arXiv: 1910.03887.

[22] K. Abe et al. "Proposal for an Extended Run of T2K to 20×10^{21} POT". In: (Sept. 2016). arXiv: 1609.04111 [hep-ex].

[23] K. Abe et al. "Hyper-Kamiokande Design Report". In: (May 2018). arXiv: 1805.04163 [physics.ins-det].

[24] K. Abe et al. "T2K ND280 Upgrade - Technical Design Report". In: (Jan. 2019). arXiv: 1901.03750 [physics.ins-det].

[25] Yoshinari Hayato. "A neutrino interaction simulation program library NEUT". In: *Acta Phys. Pol. B* 40.9 (2009), pp. 2477–2489. ISSN: 05874254.

[26] K. Abe et al. "Measurement of the muon neutrino charged-current single $\pi+$ production on hydrocarbon using the T2K off-axis near detector ND280". In: *Phys. Rev. D* 101.1 (2020). ISSN: 24700029. DOI: 10.1103/PhysRevD.101.012007. arXiv: 1909.03936.

[27] *Plastic Scintillating Fibers*. http://kuraraypsf.jp/.

[28] Hamamatsu Photonics K.K. *MPPC Technical note*. https://www.hamamatsu.com/resources/pdf/ssd/mppc_kapd9005e.pdf. 2017.

[29] *OMEGA - Centre de microélectronique — Organisation de Micro-Electronique Générale Avancée*. https://portail.polytechnique.edu/omega/en.

[30] J. Fleury et al. "Petiroc and Citiroc: Front-end ASICs for SiPM readout and ToF applications". In: *J. Instrum.* 9.1 (2014). ISSN: 17480221. DOI: 10.1088/1748-0221/9/01/C01049.

[31] A. Blondel et al. "The SuperFGD Prototype charged particle beam tests". In: *Journal of Instrumentation* 15.12 (Dec. 2020), P12003–P12003. DOI: 10.1088/1748-0221/15/12/p12003. URL: https://doi.org/10.1088/1748-0221/15/12/p12003.

[32] Mark Thomson. *Modern Particle Physics*. 4th ed. Cambridge CB2 8BS, United Kingdom: Cambridge University Press, 2013. ISBN: 9781107034266. URL: https://www.cambridge.org/ae/academic/subjects/physics/particle-physics-and-nuclear-physics/modern-particle-physics.

[33] C.H. Llewellyn Smith. "Neutrino reactions at accelerator energies". In: *Physics Reports* 3.5 (1972), pp. 261–379. ISSN: 0370-1573. DOI: https://doi.org/10.1016/0370-1573(72)90010-5. URL: http://www.sciencedirect.com/science/article/pii/0370157372900105.

[34] Dieter Rein and Lalit M Sehgal. "Neutrino-excitation of baryon resonances and single pion production". In: *Annals of Physics* 133.1 (1981), pp. 79–153. ISSN: 0003-4916. DOI: https://doi.org/10.1016/0003-4916(81)90242-6. URL: http://www.sciencedirect.com/science/article/pii/0003491681902426.

[35] V. Barone, C. Pascaud, and F. Zomer. "A new global analysis of deep inelastic scattering data". In: *Eur. Phys. J. C* 12.2 (2000), pp. 243–262. ISSN: 14346044. DOI: 10.1007/s100529900198.

[36] Dieter Rein and Lalit M. Sehgal. "Coherent 0 production in neutrino reactions". In: *Nuclear Physics B* 223.1 (1983), pp. 29–44. ISSN: 0550-3213. DOI: https://doi.org/10.1016/0550-3213(83)90090-1. URL: http://www.sciencedirect.com/science/article/pii/0550321383900901.

[37] N. J. Baker et al. "Quasielastic neutrino scattering: A measurement of the weak nucleon axial-vector form factor". In: *Phys. Rev. D* 23 (11 June 1981), pp. 2499–2505. DOI: 10.1103/PhysRevD.23.2499. URL: https://link.aps.org/doi/10.1103/PhysRevD.23.2499.

[38] R.A. Smith and E.J. Moniz. "Neutrino reactions on nuclear targets". In: *Nuclear Physics B* 43 (1972), pp. 605–622. ISSN: 0550-3213. DOI: https://doi.org/10.1016/0550-3213(72)90040-5. URL: http://www.sciencedirect.com/science/article/pii/0550321372900405.

[39] J. Nieves, E. Oset, and C. Garcia-Recio. "A theoretical approach to pionic atoms and the problem of anomalies". In: *Nuclear Physics A* 554.4 (1993), pp. 509–553. ISSN: 0375-9474. DOI: https://doi.org/10.1016/0375-9474(93)90245-S. URL: http://www.sciencedirect.com/science/article/pii/037594749390245S.

[40] Omar Benhar and Adelchi Fabrocini. "Two-nucleon spectral function in infinite nuclear matter". In: *Phys. Rev. C* 62 (3 Aug. 2000), p. 034304. DOI: 10.1103/PhysRevC.62.034304. URL: https://link.aps.org/doi/10.1103/PhysRevC.62.034304.

[41] J. Nieves, I. Ruiz Simo, and M. J. Vicente Vacas. "Inclusive charged-current neutrino-nucleus reactions". In: *Phys. Rev. C* 83 (4 Apr. 2011), p. 045501. DOI: 10.1103/PhysRevC.83.045501. URL: https://link.aps.org/doi/10.1103/PhysRevC.83.045501.

[42] R. Gran et al. "Neutrino-nucleus quasi-elastic and 2p2h interactions up to 10 GeV". In: *Phys. Rev. D* 88 (11 Dec. 2013), p. 113007. DOI: 10.1103/PhysRevD.88.113007. URL: https://link.aps.org/doi/10.1103/PhysRevD.88.113007.

[43] Y. Hayoto. "Neut". In: *Nucl. Phys. B - Proc. Suppl.* 111 (2002), pp. 171–176. ISSN: 09205632. DOI: 10.1016/s0920-5632(02)01759-0.

[44] *Overview — geant4.web.cern.ch.* https://geant4.web.cern.ch/node/1.

[45] Saúl Alonso-Monsalve et al. *Graph neural network for 3D classification of ambiguities and optical crosstalk in scintillator-based neutrino detectors.* 2020. arXiv: 2009.00688 [hep-ex].

[46] M. Daszykowski and B. Walczak. "Density-Based Clustering Methods". In: *Compr. Chemom.* 2 (2009), pp. 635–654. DOI: 10.1016/B978-044452701-1.00067-3.

[47] R. C. Prim. "Shortest connection networks and some generalizations". In: *The Bell System Technical Journal* 36.6 (1957), pp. 1389–1401. DOI: 10.1002/j.1538-7305.1957.tb01515.x.

[48] Hans R. Künsch. "Particle filters". In: *Bernoulli* 19.4 (Sept. 2013), pp. 1391–1403. ISSN: 1350-7265. DOI: 10.3150/12-bejsp07. URL: http://dx.doi.org/10.3150/12-BEJSP07.

[49] *TMVA - ROOT*. https://root.cern/manual/tmva/. (Accessed on 01/07/2021).

[50] *ROOT: analyzing petabytes of data, scientifically. - ROOT*. https://root.cern/. (Accessed on 01/07/2021).